Quantum Dot–Cavity Systems

By:
Luís Miguel Pais Pinto Martins

Department of Physics and Astronomy
The University of Sheffield

A thesis submitted for the degree of Doctor of Philosophy

Friday 1st September, 2017

Não sou nada.

Nunca serei nada.

Não posso querer ser nada.

À parte isso, tenho em mim todos os sonhos do mundo.

–Alváro de Campos in Tabacaria

To my lovely mother, *Fernanda*.

Acknowledgements

Firstly, I'd like to thank my supervisors Prof Mark Fox and Prof Maurice Skolnick for giving me the opportunity to study for my PhD in the LDSD group at Sheffield. Secondly, Feng Liu and Alistair Brash for teaching me so much throughout the process and for being so incredibly dedicated to the project, with whom I have worked with on the experiments for this project over the past three years. Big thanks to all members of the LDSD group for their helpful discussions and for making the LDSD such an excellent and enjoyable group to work in, particularly A. Waeber, E. Checkovich, A. Ul Haq with whom I learnt so much at every single dot meeting.

I'm very grateful for the assistance of the following people during my time at Sheffield: Chris Vickers and Philip Taylor in the helium liquefier, Paul Kemp-Russell and the other workshop staff, all the III-V centre staff, especially Ben Royal and Christopher Bentham for helping with sample fabrication. Even though I never had the pleasure of meeting Yanwen Wu and M. Hopkinson, these experiments would not have been possible without the single-dot wafer that they grew long ago. I also thankful to John O'hara who contribute to the chapter 4 performing the Rayleigh scattering measurement. For the funding to carry out this research, I'm grateful to University of Sheffield and the EPSRC.

I'd like to thank all friends I made in Sheffield, they made my life in this unique city pleasurable even with this awful weather, especially to Paco and Hyunju with who I learnt to enjoy the bitterness of the Peruvian filter coffee and their friendship and advices help me to carry on and focus on my PhD.

Thank all for your huge support.

Luís

Abstract

This thesis presents experiments carried out on a single InGaAs/GaAs quantum dot coupled with a photonic crystal cavity (H1). The single exciton qubit system is controlled by ultrafast optical pulses. Then, the resonance fluorescence (RF), which is proportional to the population of the quantum dot, is measured by a spectrometer. The two main results of the whole thesis are: *i*) measurement of the short exciton lifetime (22.7 ps); *ii*) achievement of full populated quantum dot through a few photons (on average ≈ 2.5 photons). To measure such a short lifetime the Two Pulse Resonance Fluorescence technique was developed. This technique enables measurements with high time resolution. This required the development of the Differential Resonance Fluorescence technique. This technique is highly efficient in suppressing the laser scattered light, permitting measurements of the RF of the dot. These two main results are the consequence of cavity enhancement. A Purcell factor of 42 was measured. This is the largest Purcell factor reported so far for the weak coupling regime. This enhancement allows the recovery of the coherence of the QD, permitting the investigation of the quantum dot–cavity system as a near–ideal single photon source on–chip and on–demand. The cavity enhancement also affects the exciton–phonon interaction. The full monotonic phonon side band is here presented for first time. This quantum dot–cavity system also allows the control of the cavity scattered light from the quantum dot. This can be used as an ultrafast switcher.

Publications

[1] F. Liu, **L. M. P. P. Martins** *et al*; "Ultrafast depopulation of a quantum dot by LA-phonon-assisted stimulated emission", Phys. Rev. B 93, 161407(R), (2016)

[2] A. J. Brash, **L. M. P. P. Martins** *et al*; "High-fidelity initialization of long-lived quantum dot hole spin qubits by reduced fine-structure splitting" Phys. Rev. B 92, 121301(Rapid Comms.), (2016)

[3] A. J. Brash, **L. M. P. P. Martins** *et al*; "Dynamic vibronic coupling in InGaAs quantum dots [Invited]", Vol. 33, No. 7 / July 2016 / Journal of the Optical Society of America B (2016)

[4] Feng Liu, Alistair J. Brash, John O'Hara, **L. M. P. P. Martins**, Catherine L. Phillips, Rikki J. Coles, Ben Royall, Chris Bentham, Nicola Prtljaga, Igor Itskevitch, Luke R. Wilson, Edmund Clarke, M. S. Skolnick, and A. M. Fox; "High Purcell factor generation of coherent on-chip single photons" Submitted to Nature Nanotechnology

[5] **L. M. P. P. Martins**, Feng Liu, Alistair J. Brash, M. S. Skolnick, and A. M. Fox; "Ultrafast Single Control of the Cavity Scattered Light Trough a Single QD" In preparation.

[6] **L. M. P. P. Martins**, Feng Liu, Alistair J. Brash, M. S. Skolnick, and A. M. Fox; "Cavity-enhanced exciton-phonon coupling" In preparation.

Contents

List of Figures

Chapter 1

Introduction

Moore's law [1] predicts that the number of transistors in a chip doubles every year. That means that the computation power also doubles every year. Such an increase results from miniaturisation of transistors from the semiconductor lithography techniques. However there is a physical limitation to miniaturisation. When a transistor switches a single electron, it is not possible to further miniaturise: quantum mechanics is applicable.

To overcome this limitation, Feynman [2] and Deutsch [3] suggested taking advantage of the quantum properties of superposition and entanglement states. Superposition can be the answer to power processor limitation. A conventional processor is based on irreversible logic–operations. Classically a bit has a value 0 or 1. A bit under a logic operation gives only one output (0 or 1). The number of operations (and bits) necessary to solve a task depends on the complexity of the task. For complex tasks the number of operations is greater and consequently computation time is longer. However, because of the superposition property, quantum bits (qubits) can be 0 and 1 simultaneously. Thus, for N qubits, 2^N operations can be performed. This means that for a quantum computer much more operations can be performed compared with a classical computer. This is

called *quantum parallelism*.

The typical example to show the difference between a classical and quantum computer is the factorization of prime numbers. This kind of problem is extremely complex and requires huge computational power. The difficulty of factorization of prime numbers is used in cryptography to keep communication secure. The computational time to solve this problem for a classical computer is exponential to n (n being the number of digits of a prime number). Using a quantum algorithm (Shor's algorithm [4]) the processing time is a polynomial of n. This processing time difference is more obvious for higher n.

Quantum information processing (QIP) opens the door to a new information world where a complex computational problem which nowadays takes years to solve could be solved with a quantum computer in a few seconds. However this also brings many challenges. The question which motivates this work, and hopefully this thesis contributes to answering, (even in a small portion) is: How to build a quantum circuit?

1.1 DiVincenzo criteria

To build a quantum computer several requirements must be fulfilled. These were summarized by David DiVincenzo's criteria [5]

1. **A scalable physical system with well characterized qubits**

   A qubit is a quantum two level system like two spin states of a spin 1/2 particle, or a ground and excited state of an atom, or the vertical and horizontal polarization states of a single photon. Scalability is obtained when a large number of individual qubits are addressed.

2. **The ability to initialize the state of the qubit to a simple fiducial state**

The qubit has to be set in a known state before the computation. The initialization time must be much faster than the timescale of the computation. Moreover, the quantum error correction requires a continuous supply of 0's (lowest entropy states $|0\rangle$).

3. **Long relevant decoherence times, much longer than the gate operation time**

   The interaction between the qubit and the environment degrades the qubit state which tends to an incoherent, mixed state. The time taken for a coherent state to degenerate to a mixed state is the decoherence time. This must be much longer than the gate operation time, otherwise the qubit will be in an unknown state causing errors. The decoherence time must be 10^4–10^5 larger than the gate operation time.

4. **A universal set of quantum gates**

   This is the core of quantum computation. Any algorithm is a sequence of unitary transformations (or gates) acting on qubits. A "universal" set of quantum gates is the set of the simplest gates in which all operations can be reduced.

5. **A qubit–specific measurement capability**

   The result of a computation must be read out and this requires the ability to measure specific qubits. To do this efficiently long decoherence times (*point 3*) and high fidelity is necessary.

For quantum computation the above five requirements are enough. However to include other kinds of information processing such as quantum communications two further requirements are necessary [5]:

6. **The ability to interconvert stationary and flying qubits**

7. **The ability to faithfully transmit flying qubits between specific**

locations

where the flying qubits are transmitted qubits. The latter is particularly important for quantum key distribution (QKD) protocols and quantum networks.

1.2 Qubit Candidates

1.2.1 Photonic Qubits

The simplest qubit scheme is polarization states of a single photon [6]. As the photons interact weakly with the environment, they present long coherence times which is one of the requirements of DiVincenzo's criteria. Moreover, the polarization photon is easily manipulable through wave retardation plates and can be easily transferred in-chip by waveguides. However, the photons are difficult to store, which bring big challenges.

1.2.2 Trapped Ions/Atoms

Using a magnetic field or an optical field, or both, individual ion atoms can be isolated [7–9]. The qubit states are the ground and excited state or two internal (hyperfine) states. To address the qubit states, a laser is used. These systems present long decoherence times, easy scalability and high fidelity [8].

1.2.3 Crystal Impurity Centres

Isolated electron spin can be obtained from crystal impurities as for example the active nitrogen vacancy centres in diamond crystals [10] or impurities in silicon crystals [11, 12]. The qubit states are the spin states of the electron. These systems have very high fidelity gate operation and very long coherence times.

1.2.4 Atomic Nuclei

The nuclear spin can be manipulated by radio frequency pulses. This is a very well–established technique called Nuclear Magnetic Resonance (NMR) and can be used to implement quantum algorithms [13]

1.2.5 Josephson Junctions

Josephson junctions are two superconductors weakly coupled. Josephson effect is a macroscopic manifestation of quantum effects. The quantized energy levels of this system allow one to use it as a qubit. The Cooper pair [14, 15] and the flux [16] can be used as qubit states.

1.2.6 Quantum Dots

Quantum Dots (QD) are artificial heterostructures of semiconductors smaller than the de Broglie wavelength of the charge carriers. Thus, energy confinement results, in all three dimensions. There are several techniques to form QDs: epitaxial growth at the interface of lattice mismatched solids [17]; fluctuations in higher-dimensional structures [18]; colloidal nano-particles [19], or an electrostatic localizing potential in a 2D electron gas [20].

The QDs can be manipulated by optical, electronic or spin-resonance techniques. Moreover, they can be easily integrated with photonic devices such as photonic crystal cavities and waveguides.

The work presented in this thesis was performed using a QD grown by self assembly technique (see section 2.1) coupled with a H1 photonic crystal cavity and waveguides.

For several reasons the self–assembled QDs (SAQDs) are good candidates

for a qubit. The atom-like emission and the stable solid-state environment are the main advantages of the SAQDs. Furthermore, as the SAQDs result from an engineering band–gap, the dot properties can be tailored. The fact that optical control of QD is possible is another advantage. Finally, the SAQDs can be easily integrated into electronic circuits and with photonic crystals. The flip side of the SAQDs is the random distribution of sizes, positions and aspect ratios across the wafer. However on–site controlled growth methods [21, 22] and QD registration [23] can overcome this disadvantage. Another limitation is the interaction with nuclear spins and with phonons, something which causes dephasing for a coherent state. However cavity enhancement overcomes the dephasing as is shown in chapter 4.

1.3 Chapter abstracts

In this section a brief summary of each chapter is presented:

- **Chapter 2: Background and Literature Review**

  In this chapter QDs will be explained in detail. What is a QD? How do QDs grow by the Stranski-Krastanov's technique? What makes a QD a good candidate for a qubit? Many other questions regarding QDs are answered in this chapter.

- **Chapter 3: Experimental Methodology**

  In this chapter the experimental techniques used to obtain the results given in following chapters are explained. The sample, and the QD–cavity system under study, are characterized in detail.

- **Chapter 4: On-Chip On-Demand Electrical Tuneable Single Pho-**

ton Source

In this chapter, a waveguide-coupled Photonic Crystal Cavity (PCC) is used to strongly reduce the radiative lifetime ($T_1 = 22.7$ ps) of the QD. Here a strong Purcell factor (42) is reported. To measure such short lifetimes, the Two Pulse Resonance Fluorescence (TPRF) technique was developed. The short exciton lifetime overcomes the dephasing, restoring the ideal coherence of the photon emitter ($T_2 \approx 2T_1$). Autocorrelation and Hong–Ou-Mandel (HOM) measurements were performed, by exciting the QD from the cavity and detecting the resonance fluorescence signal from the outcoupler. High purity (86%) and high indistinguishability (90%) were obtained on–demand and on–chip. These results confirm that this device is a near–ideal single photon source operating on–demand and on–chip.

- **Chapter 5: Influence of Cavity on QD Exciton–Phonon Coupling**
  This chapter gives a detailed study of how the cavity affects the exciton–phonon interaction. The electric field enhancement of ≈ 4.5 is reported. This means that only a few photons are needed to populate the QD. Furthermore, slow damping in Rabi oscillations were observed, indicating that the cavity suppresses the exciton-phonon interaction. This mechanism is not yet fully understood. Electric field enhancement also makes it possible to see the full picture of the exciton–phonon interaction. These results are discussed in detail in this chapter.

- **Chapter 6: Ultrafast Optical Control of Light Scattering in a QD Cavity System**
  In a weak coupling regime the cavity scattered light can be controlled by a single QD through variation of the refractive index. This variation occurs

when the QD is populated, consequently affecting the cavity scattered light. This phenomenon can be explained from a simple phenomenological model and can be used to form an ultrafast optical switching.

- **Chapter 7: Conclusions & Outlook**

  Here the main conclusion are listed. possible future developments are also considered.

- **Appendixes**

  The interaction between the exciton and the LA phonons is addressed theoretically through a master equation model. The deconvolution of time resolved data is also explained.

Chapter 2

Quantum Dots

2.1 Self Assembled Quantum Dots

The quantum dots studied in this thesis are grown by the Stranski-Krastanov (SK) technique [24]. This technique takes advantage of the difference between the lattice constants of the substrate material and the quantum dot material. The usual materials are GaAs as the substrate and In(Ga)As as the quantum dot material. The InAs lattice constant is 7% larger than the GaAs. The InAs is deposited layer by layer on the GaAs substrate by molecular beam epitaxy (MBE). As a first step, a thin film of an InAs monolayer is grown on a GaAs substrate, forming the so called wetting layer. At around 1.6 monolayers, strain, built as result of the lattice mismatch, exceeds the critical limit. The energy minimization leads to lateral relaxation, forming InGaAs islands. The quantum dots are subsequently capped with GaAs [25]. During the capping process some gallium diffuses into the dot, resulting in In(Ga)As QDs.

The samples grown from this self–assembly technique have $10^8 - 10^{11}$ dots per cm^2. The self-assembled method causes statistical variation in quantum dots, so they have different forms (lens, pyramidal, cylindrical) and sizes ($3 - 5$ nm of

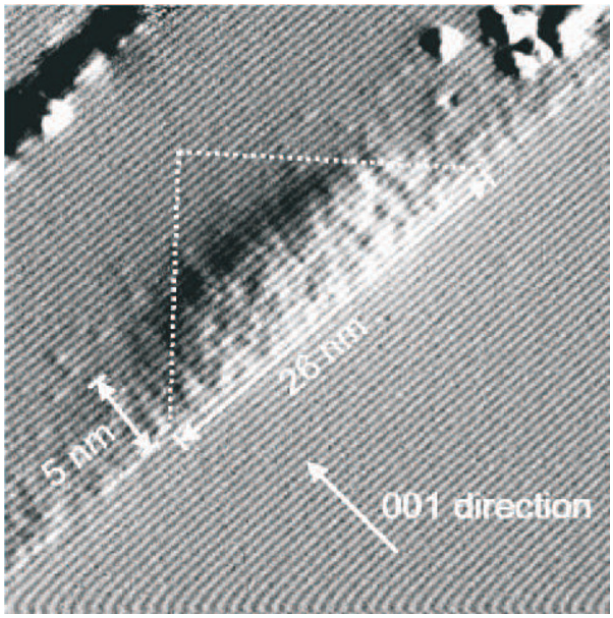

Figure 2.1: The cross-sectional scanning tunneling microscope image of an InAs/GaAs quantum dot (figure from [26]).

height and $15 - 25$ nm of diameter). Figure 2.1 shows a quantum dot with a truncated square pyramid shape. At such small dimensions the energy states become completely quantized, like atoms. QDs are therefore frequently called as "artificial atoms".

2.2 Electron and Hole Energy Levels

In III-V semiconductor materials the valence band derives from the p state of atoms, while the conduction band comes from the s state of atoms. As a consequence the angular momentum quantum number for the conduction band is $L = 0$, while for the valence band it is $L = 1$ [27]. The total angular momentum of electrons in the conduction band is only the spin quantum number $s_z^e = 1/2$. Two different projection in the z-direction (optical axis) are possible $m_{s,z}^e = \pm 1/2$. On the other hand, as the valence band has $L = 1$, the total angular momentum of holes is $j_z^h = 3/2$ and $j_z^h = 1/2$. The holes with total momentum $j_z^h = 1/2$ are not usually taken into account for QD transitions. Due to the difference in con-

finement energy the heavy holes ($m_{j,z}^{h,h} = \pm 3/2$) and the light holes ($m_{j,z}^{lh} = \pm 1/2$) become split. Typical energy splitting between heavy and light holes is > 10 meV. Thus, the light holes are usually neglected.

The electric confinement experienced by the carriers results in a discrete density of electronic states

As the band gap of InGaAs is lower than the GaAs, the carriers experience confinement in the quantum dot region. This potential confinement is further modified by strain in the crystal lattice of the QD. A piezoelectric field may also affect the potential, depending on the growth direction of dots on GaAs. For the dots under study this effect is negligible [28, 29].

In these dot structures the height is significantly smaller than the lateral size. The vertical and the in-plane motion are decoupled, and can thus be separated. The energies of the single particle state are given by:

$$E = E_z + E_{\text{in plane}} \,. \tag{2.1}$$

As the height is very small the confinement in the z direction is very strong. It is therefore assumed that the carries are in ground state, since there is a large energy gap between the first and second level energy (if this exists). The in-plane confinement potential is a parabola (rotational symmetry) $V(r) = \frac{1}{2} m\omega_0^2 r^2$. It has been shown that a single particle state in a lens-shaped QD can be approximated by a pair of harmonic oscillators [30, 31]. Thus, the energy eigenvalues at zero magnetic field are given by:

$$E_{n,m} = \hbar\omega_0(n + m + 1) \,, \tag{2.2}$$

where n and m are the quantum numbers of a two dimensional harmonic oscillator. The eigenvectors are the Fock-Darwin states, $|n, m\rangle$. The angular momentum

for electrons (holes) is $l = n - m$ ($l = m - n$) and the degeneracy of each shell is given by $g_S = 2(S + 1)$, where $S = m + n$ indicates the shell (*s, p, d, ...*, as in shell structure in atomic physics), and the factor 2 takes into account the spin degree of freedom. Due to the selection rules, electrons from a valence band can only be promoted to the same shell in the conduction band (*i.e s–s, p–p, ...*). Such rules are relaxed when the shells become mixed, as for example for highly asymmetric dots.

The electron-hole Coulomb interaction results in the formation of excitons. The exciton can be treated as a two–level system because of 3–D confinement. Due to the conservation of angular momentum only the transition between the heavy hole in the valence band and the electron in the conduction band with $S_z = m^e_{s,z} + j^h_z = \pm 1$ are allowed (bright excitons). This means that only electron-hole pairs in $|\Uparrow\downarrow\rangle$ (circular polarized light σ^+) and $|\Downarrow\uparrow\rangle$ (circular polarized light σ^-) states are allowed. The other states ($S_z = \pm 2$, $|\Uparrow\uparrow\rangle$ and $|\Downarrow\downarrow\rangle$) are forbidden and they are called dark excitons. Figure 2.2 shows the schematic electronic bandstructure of a self–assembled quantum dot. The neutral exciton state $|\uparrow\Downarrow\rangle$ and the bi–exciton are shown in Figure 2.2 a) and b) respectively. Note that due to the Pauli exclusion principle the bi–exciton can only be created by binding two excitons with different spins. This is discussed in Optical Selection Rules (see section 2.4)

2.3 Fine Structure

The asymmetry of the quantum dot results in an anisotropic electron-hole exchange interaction. This break of symmetry lifts the degeneracy of the exciton states. This interaction can be represented by the following Hamiltonian [32, 33]:

$$H_{\text{exchange}} = -\sum_{i=x,y,z} \left(a_i J_{h,i} \cdot S_{e,i} + b_i J_{h,i}^3 \cdot S_{e,i} \right) . \tag{2.3}$$

In Equation (2.3) $S_{e,i}$ ($J_{h,i}$) is the spin projection in i^{th} direction of the electron (hole), while a_i and b_i measure the strength of interaction. In the exciton state representation, H_{exchange} becomes:

$$H_{\text{exchange}} = \frac{1}{2} \begin{pmatrix} +\delta_0 & +\delta_1 & 0 & 0 \\ +\delta_1 & +\delta_0 & 0 & 0 \\ 0 & 0 & -\delta_0 & +\delta_2 \\ 0 & 0 & +\delta_2 & -\delta_0 \end{pmatrix} , \tag{2.4}$$

with basis $M = S_{e,z} + J_{h,z}$ ($\{|+1\rangle, |-1\rangle, |+2\rangle, |-2\rangle\}$). $\delta_0 = \frac{3}{4}a_z + \frac{27}{16}$, $\delta_1 = -\frac{3}{8}(b_x - by)$ and $\delta_2 = -\frac{3}{8}(b_x + b_y)$ are the exchange energy splittings. For an InGaAs quantum dot, the exchange energy splitting are typically $\delta_0 = 100$ to $500\,\mu$eV,

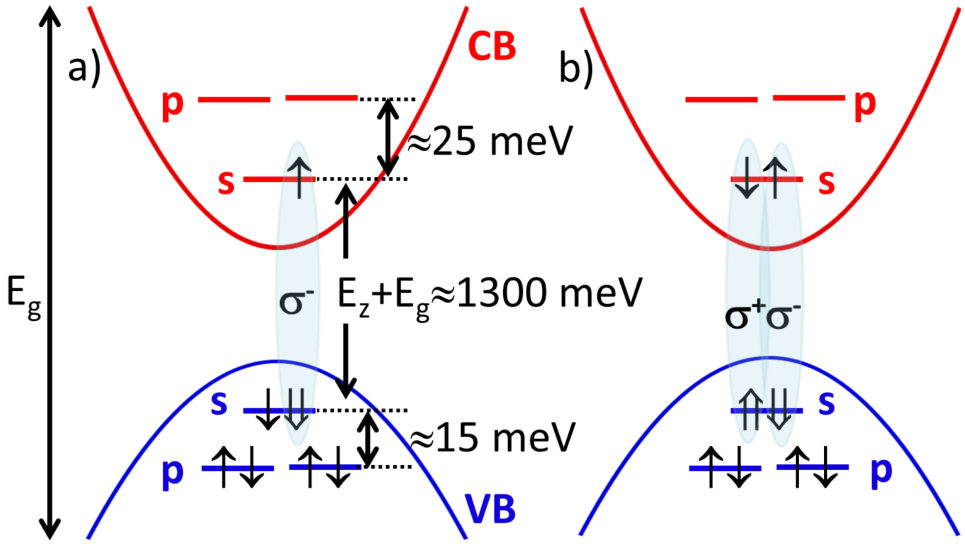

Figure 2.2: The s and p-shells in the conduction (CB) and valance bands (VB) for the QD. Each shell is twofold spin degenerate. a) By exciting with a circular polarised light (σ^-), the exciton with $|\uparrow\Downarrow\rangle$. b) The bi–exciton results from two excitons with different states due to the Pauli exclusion principle. Legend: $\uparrow$ $m^e_{s,z} = +1/2$, $\downarrow$ $m^e_{s,z} = -1/2$, $\Uparrow$ $m^{h,h}_{j,z} = +3/2$ and $\Downarrow$ $m^{h,h}_{j,z} = -3/2$. Light holes have been neglected for this diagram.

$\delta_1 = 10$ to $100\,\mu$eV [34] and $\delta_2 \approx 0$ [33, 35]. Thus, the spin–spin interaction lift the degeneracy of the exciton states and mixes the bright states. This means that the eigenstates are a superposition of the circular states, becoming linear states:

$$|\Psi_X\rangle = \frac{1}{\sqrt{2}}\left(|\Downarrow\uparrow\rangle + |\Uparrow\downarrow\rangle\right) \tag{2.5}$$

$$|\Psi_Y\rangle = \frac{1}{\sqrt{2}}\left(|\Downarrow\uparrow\rangle - |\Uparrow\downarrow\rangle\right), \tag{2.6}$$

where the eigenstates $|\Psi_X\rangle$ and $|\Psi_Y\rangle$ are aligned along the in-plane crystal axes [110] and [$\bar{1}$10] (x and y axes, respectively).

2.4 Optical Selection Rules

The creation of an exciton and a bi–exciton follows selection rules which result from conservation of the angular momentum and the Pauli exclusion principle. Therefore, an exciton is created if the quantum dot is excited with circular polarised light, as mentioned above. However, for an asymmetric quantum dot, the fine structure splitting (FSS) arises and the eigenstates become linear. In this case, if the transition is addressed with a circular polarised light and the pulse line–width is smaller than the FSS, the precession of the exciton states is observed.

Figure 2.3 shows the optical selection rules of the creation of an exciton and bi–exciton for circular and linear polarised light excitation. The schematic energy diagram shows the ground state ($|0\rangle$), the exciton ($|X\rangle$) and the bi–exciton ($|XX\rangle$)

The bi–exciton has an energy of $2E_X - E_b$, where E_X is the exciton energy and E_b the binding energy between two excitons. Due to the Pauli exclusion principle the bi–exciton state in circular basis can only be $|XX\rangle = |\uparrow\downarrow\Uparrow\Downarrow\rangle$

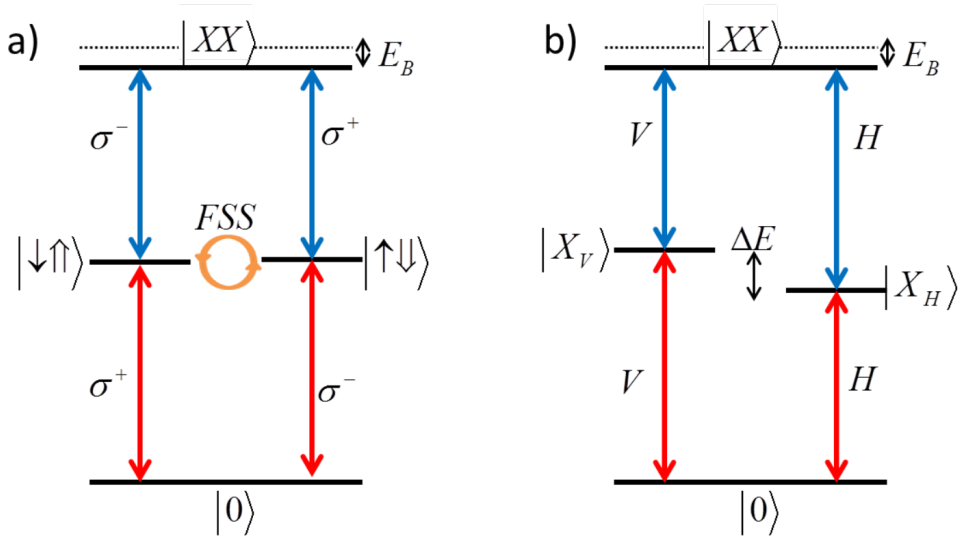

Figure 2.3: Optical selection Rules for an exciton and a bi–exciton for circular (a) and linear (b) polarised basis. Legend: $|H\rangle = 1/\sqrt{2}\,(|\uparrow\Downarrow\rangle + i|\downarrow\Uparrow\rangle)$, $|V\rangle = 1/\sqrt{2}\,(|\uparrow\Downarrow\rangle - i|\downarrow\Uparrow\rangle)$, $|XX\rangle = |\uparrow\downarrow\Uparrow\Downarrow\rangle$, E_B is the bi–exciton binding energy, FSS stands for Fine Structure Splitting and ΔE is the fine structure splitting energy.

2.5 Electric Field

2.5.1 Quantum-Confined Stark Effect

Applying a DC electric field, the potential confinement is modified by the Quantum-Confined Stark Effect (QCSE). The electric field causes the hole and electron wave–functions to change in such a way that the exciton energy is shifted [36]. This energy shift (ΔE_{QCSE}) can be computed by second order perturbation theory, assuming the DC electric field as a perturbation. ΔE_{QCSE} varies quadratically with the electric field (F),

$$\Delta E_{\mathrm{QCSE}} = pF + \beta F^2\,, \tag{2.7}$$

where β is the electric polarizability and p is the permanent dipole. This permanent dipole arises because of the non–uniform material composition in self–assembly quantum dots (SAQDs). For InGaAs QDs grown by the SK technique,

the electron wavefunction is localized at the bottom and the hole wavefunction is at the top of the QD (high indium content region) [37, 38]. This separation causes a strong permanent dipole aligned with the growth direction. Thus, a DC electric field applied in the growth direction results in a large energy shift due to the QCSE. The QCSE can also be used to determine p and hence measure the average distance between the electron and hole in the QD. The Stark effect can also occur due to internal electric fields, as for example the charge noise [39, 40]

2.5.2 Optical Stark Effect

Stark effects can also be induced by an Alternating Current (AC) electric field from an electromagnetic wave. The Stark shift depends on the angular frequency and strength of the laser. As the shift is induced by light it is called the Optical Stark Effect (OSE). The shift induced by OSE is

$$\Delta E_{\mathrm{OSE}} = \pm\frac{\hbar}{2}\left(\Delta - \sqrt{\Delta^2 + |\Omega_R|^2}\right) , \tag{2.8}$$

where Δ is the detuning between the laser and QD frequency and $\Omega_R = \mu E/\hbar$ is the Rabi frequency, μ the transition dipole moment and $E(t)$ the electric field of the laser.

The energy shift induced by the OSE is sensitive to polarization. This means that only the eigenstate co–polarized with the laser experiences the shift. Thus, OSE can be used to tune a specific exciton state and consequently cancel the Fine Structure Splitting. This allows improvement of the fidelity and the initialisation [41, 42].

In [42], we demonstrated an on-demand hole spin qubit initialization scheme meeting four key requirements of quantum information processing: fast initialization (100 ps); high fidelity ($F > 99\%$); long qubit lifetime ($2T_h > T_2^* \approx 10$ ns),

and compatibility with optical coherent control schemes. This is achieved by rapidly ionizing an exciton in an InGaAs quantum dot with very low fine-structure splitting at zero magnetic field. Furthermore, we showed that the hole spin fidelity of an arbitrary quantum dot can be increased by optical Stark effect tuning of the fine-structure splitting close to zero. In our scheme the OSE is induced by a linearly polarized CW laser which is positively detuned from the co-polarized $X \rightarrow XX$ (biexciton) transition by Δ_{CW}. The neutral exciton eigenstates ($X_{H/V}$) are linearly polarized along the in-plane crystal axes, and can be addressed individually by selecting the laser polarisation. X_H and X_V are split by δ_{FS}; we define X_V to be lower in energy. A positive-detuned V-polarized laser addresses the X_V state and acts to reduce δ_{FS} by Stark-shifting the X_V state to higher energy. By contrast, an H-polarized laser increases δ_{FS} by shifting the X_H state to higher energy. In the case of positive detuning ($\Delta_{CW} > 0$), the change in FSS due to the OSE (ΔE_{OSE}) is given by eq. (2.8). Full details of this work are presented in [42].

2.6 QD–Environment Interactions

A QD is generally called an artificial atom, because of its unique optical properties (bright single emitter, narrow line–widths). However a QD is typically formed by 10^5 atoms. This makes the system much more complex and rich in phenomena than isolated atoms, once the interaction between the exciton and the QD environment is taken into account. In this section, these environment interactions and their consequences are listed.

2.6.1 Bloch Sphere

These interaction between the exciton and the environment causes a degradation of the quantum state. The Bloch sphere is an appropriate way to represent the QD state (see fig. 2.4). The south and north pole represent the ground state ($|0\rangle$) and exciton state ($|X\rangle$), respectively. The state of the two–level system is represented by a pseudo–spin vector. Because of the dephasing processes this vector moves inwards from the sphere surface. There are two phenomenological dephasing processes: the longitudinal ($T_1 = 1/\Gamma_1$); and transverse ($T_2 = 1/\Gamma_2$). From the motion equation computed in appendix A.3, it is clear that:

$$\frac{1}{T_2} = \frac{1}{2T_1} + \frac{1}{T_2^*}\,. \tag{2.9}$$

T_1 affects the component z of the Bloch sphere as shown in fig. 2.4. This means that T_1 characterizes the relaxation from the excited state. Examples of T_1 are the radiative recombination of the exciton [43, 44] and the tunnelling of carriers from the QD [45].

T_2^* is called the pure dephasing time and affects the coherence of the state;

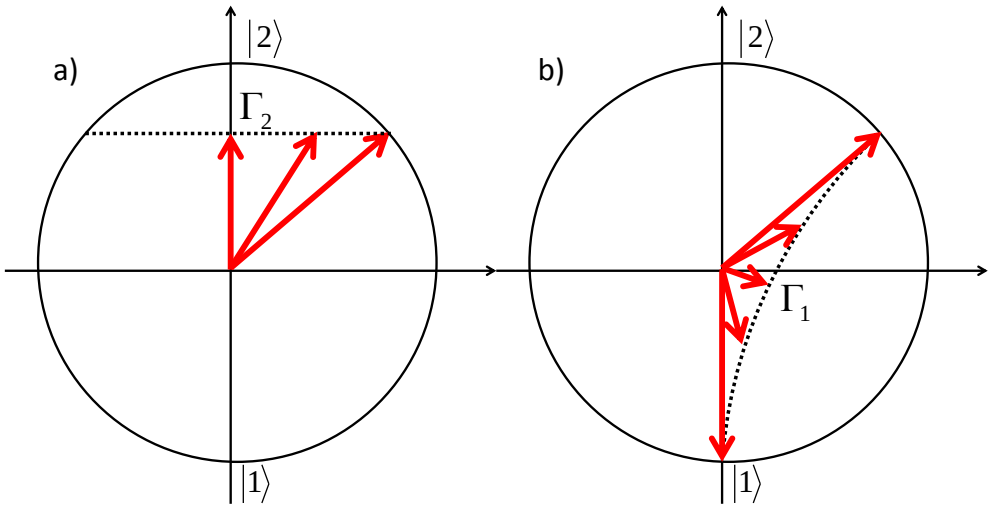

Figure 2.4: Dephasing process represented in the Bloch sphere.

this changes the x and y components of the quantum state in the Bloch sphere (the phase information) as shown in fig. 2.4. Phenomena such as hyperfine coupling to the inhomogenous Overhauser field [46], coupling between the exciton and phonon [47, 48] and charge noise [49], are examples of T_2^* processes. T_1 also affects the coherence of the state as is shown in eq. (2.9).

When the QD is coupled with a photonic cavity the dephasing times are affected, particularly T_1 due to the Purcell effect (see section 2.7.1).

2.6.2 Nuclear Field

Another contributor to dephasing is the nuclear interaction [50]. A quantum dot is a nano-structure consisting of many atoms and these atoms have nonzero nuclear magnetic moments. The nuclear-spin interaction (hyperfine) results in three individual processes: the Fermi contact hyperfine interaction; the dipole-dipole-like interaction, and the coupling of electron orbital angular momentum to the nuclear spin. The effective magnetic field created by the nuclear spin bath is called the Overhauser field. For electrons in the conduction band the last two contributions are zero, because of spherical symmetry ($s-$orbitals). On the other hand, for holes in the valence band only the first contribution is zero, because of $p-$orbital symmetry [51]. However, the Fermi contact hyperfine interaction is normally the largest term. Thus, the hole suffers less dephasing due to nuclear interaction than the electron, making the hole spin a better candidate for a solid state qubit [45]. In InGaAs/GaAs dots the Overhauser shifts can be up to $\approx 80\,\mu$eV. [52–54].

2.6.3 Electrical Environment

Carriers trapped in localized centres in the semiconductor material can affect the electric field experienced by the QD (see section 2.5). This causes the broadening of the QD [40] [55]. Moreover, the g–factor is very sensitive to the electrical environment. In an in-plane magnetic field, these electric fluctuations cause a random Lamor precession contributing to pure dephasing T_2^* [49], analogous to the nuclear spins.

2.6.4 Phonons

The semiconductor crystal lattice also interacts with the QD via emission/absorption of phonons. These phonons can be Longitudinal Optical (LO) and Longitudinal Acoustic (LA). In GaAs the energy of LO phonons is typically > 30 meV [56, 57] for $q = 0$. As the LO scattering affects the population, it contributes to T_1 dephasing. At low temperatures the LO scattering makes only a negligible contribution to pure dephasing T_2^* [58]. For these reasons they are neglected.

LA phonons have few meV of energy and present a continuous distribution. LA phonons contribute to pure dephasing, by providing an incoherent relaxation channel. To minimize the dephasing caused by phonon interaction, experiments are performed at low temperatures (4.2 K), where the phonon density distribution is very low. As the work presented in this thesis is done in the near resonant excitation regime (detuning < 7 meV), the exciton–LA phonon interaction is discussed below.

This interaction in a bare QD has been widely studied [59–61]. The coupling strength between the exciton and the LA phonon bath is given by the spectral density of the carrier-phonon interaction, $J(\omega)$ (see eq. (A.18)). This can be calculated assuming: a) the electron and the hole have a Gaussian spher-

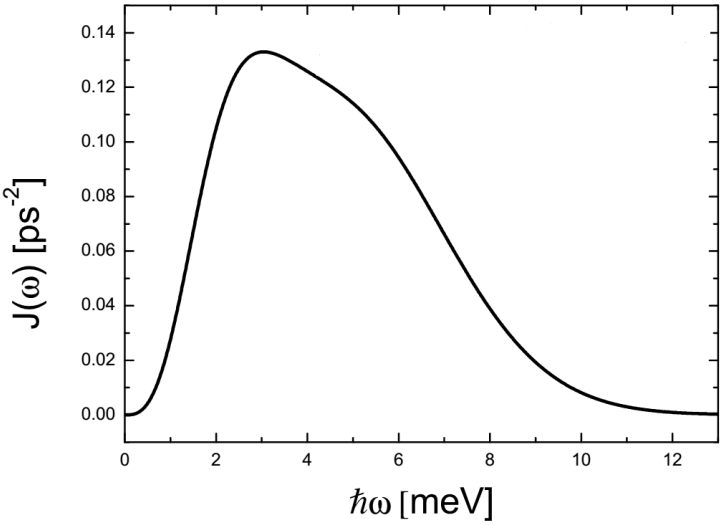

(a)

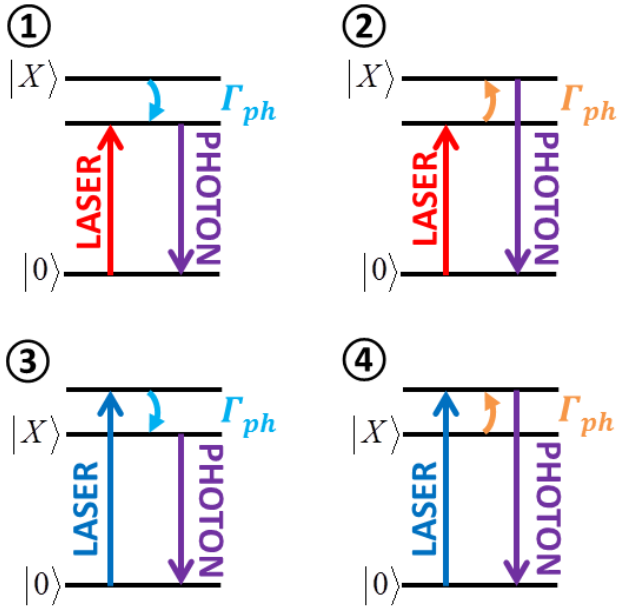

(b)

Figure 2.5: a) Density spectra function, $J(\omega)$. b) Phenomenological energy level diagrams of the phonon emission (1 and 3) and absorption (2 and 4) processes for both negative (1 and 2) and positive (3 and 4) detunings. 1 and 4 correspond to de–excitation of an exciton by, respectively emission and absorption of a phonon. On the other hand 2 and 3 correspond to excitation of an exciton by, respectively emission and absorption of a phonon. $|0\rangle$ and $|X\rangle$ are the ground and the exciton states, respectively, Γ_{ph} is the phonon relaxation rate.

ical wave–function; b) the carriers are mainly coupled with longitudinal acoustic phonons which have a linear dispersion relation [62]. Figure 2.5(a) shows the spectral density of a InGaAs QD coupled with a phonon bath. Figure 2.5(b) shows different exciton–phonon interactions. Phonon absorption processes at cryogenic temperatures are shown in fig. 2.5(b) (2) and (4). By exciting the QD with a red–shifted laser, an exciton can be created by absoption of a phonon as shown in fig. 2.5(b) (2). Figure 2.5(b) (4) shows the de–excitation of the exciton. Assuming there is already an exciton, exciting a blue–shifted laser will cause the exciton to be de–excited by absorption of a phonon. These processes are very unlikely because the probability of absorption depends on the thermal phonon density. This is determined by the Bose-Einstein statistics and for $T = 4$ K, $kT \gg \Delta E$. Therefore (2) and (4) will be not considered in this thesis.

Phonon emission processes are shown in (1) and (3) for de–excitation and excitation of an exciton, respectively. By exciting a QD with a blue–shifted laser, an exciton can be created by emission of a phonon (3). The probability of emitting a phonon is given by $J(\omega)$ as mentioned above. Similarly, an exciton is de–excited by exciting a QD with a red–shifted laser and emitting a phonon ((1)). These two processes play an important role through this work, namely in chapters 5 and 6. In appendix A the exciton–phonon bath interaction is addressed theoretically. The equations of motion were obtained through the master equation.

2.7 Optical Cavity

The interaction between a quantum emitter and a cavity has been widely studied. This field is called Cavity Quantum Electrodynamics (cQED). As the cavity confines the light, the light–matter interaction is enhanced. Through lithographic techniques it is possible to fabricate a photonic crystal cavity in a QD wafer

sample. Thus, a QD (quantum emitter) can be coupled with an optical cavity.

In this thesis a QD is coupled with a H1 photonic crystal cavity. A photonic crystal cavity is a periodic structure of two materials with different refractive indices. A band gap for light arises in the same way as the band gap for electrons in semiconductors. By introducing defects in this periodical structure it is possible to confine the light and consequently fabricate devices such as cavities, waveguides and others. This is explained in section 3.2.2

As mentioned above, coupling a single QD with a nanocavity permits the enhancement of the light–matter interactions. This offers great possibilities for quantum information processing, such as the creation of quantum logic gates [63] or a quantum electro-optic modulation [64,65], quantum optical switching [66–68] and brighter and indistinguishable quantum single photon sources [69, 70].

A cavity is characterized by the quality factor (Q–factor). This parameter defines how good the cavity is at confining the light. $Q = \omega_0/\Delta\omega$, where ω_0 and $\Delta\omega$ are respectively the resonance frequency and the linewidth of the cavity. The largest $Q-$factor is typically in the order of magnitude of tens of thousands. However [71] reports a $Q-$factor larger than $50,000$ in AlAs/GaAs photonic crystal cavities. The field leakage rate is κ. $\kappa = \Delta\omega/2$ defines how fast the light leaks out of the cavity (see fig. 2.6).

The strength of the atom–photon interaction is defined by

$$g = \sqrt{\frac{\omega}{2V_m\hbar}}\mu\,, \tag{2.10}$$

where μ is the dipole moment and V_m is the mode volume. The position of the QD inside the cavity strongly affects the g. Equation (2.10) assumes that the QD is placed at the cavity electric field maximum. The position of QDs was registered deterministically with accuracies of 50 nm, and less than 10 nm, respectively,

in [23] and [72]. In this thesis, the QDs are randomly positioned, and a selection is made from a large number of devices that are fabricated.

2.7.1 Weak Coupling Regime

When the cavity and/or QD dephasing rates (κ and γ, respectively) are larger than the coupling strength (g), the system is in a weak coupling regime ($g \ll \kappa, \gamma$). This means that the light is inside the cavity long enough to cause the QD to experience some enhancement, but not long enough to result in light–matter mixed states.

The enhancement or suppression of spontaneous emission can be observed in the weak regime. This phenomenon is called the Purcell effect [73] and is a consequence of the enhancement/suppression of density of states. This effect depends on the cavity properties and can be achieved by perturbation theory and using the Fermi Golden Rule to compute the emission rate.

The Purcell factor gives the magnitude of the spontaneous emission enhancement/suppression,

$$F_P = \frac{3}{4\pi^2}\left(\frac{\lambda_c}{n}\right)^3\left(\frac{Q}{V_m}\right)\frac{\kappa^2}{4\left(\omega_{\mathrm{QD}}-\omega_c\right)^2+\kappa^2}\frac{|\mu_{1,2}E|^2}{|\mu_{1,2}|^2|E|^2}\,, \tag{2.11}$$

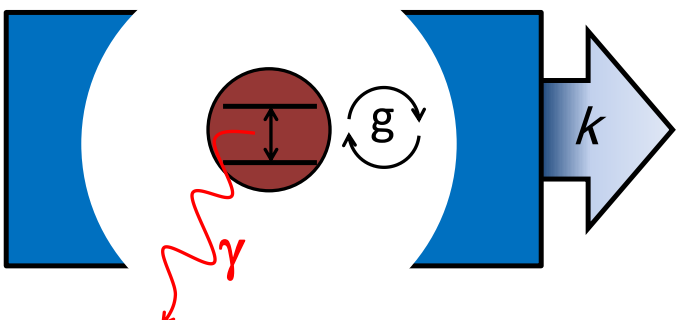

Figure 2.6: Schematic representation of a two–level system inside a cavity with a dephasing rate γ, loss rate κ and the coupling strength g.

where λ_C and ω_c are, respectively, the wavelength and frequency of cavity, ω_{QD} the frequency of the QD and n the refractive index. The term $|\mu_{1,2}E|^2/|\mu_{1,2}|^2|E|^2$ corresponds to the dipole overlapping between the quantum dot and the cavity and includes the spatial and polarisation overlapping. This term should be 1 when the QD is placed at the maximum of the cavity electric field and co–polarised with the cavity. Note that eq. (2.11) already includes the detuning between the QD and cavity frequency.

The Purcell factors reported so far are around 10 [74, 75]. However a Purcell factor of 28 was reported by [76]. This was not directly measured but estimated indirectly. In my thesis a Purcell factor of 42 was measured. This is the strongest Purcell factor reported so far. The discussion is presented in detailed in chapter 4.

2.7.2 Strong Coupling Regime

In the strong coupling regime the QD–photon interaction (g) is larger than κ or γ ($g \gg \kappa, \gamma$). In this case the light is inside the cavity long enough to interact with the QD and consequently population coherently oscillates between the QD and the cavity field [77–79]. This phenomenon is named Vacuum Rabi oscillations. The exciton states mix with light states and this is described by the well–known Jaynes-Cummings model [80]. The extension of this model for the multi-level atomic system is described by the Tavis-Cummings model [81]. To achieve strong coupling regimes the cavity must have large $Q/\sqrt{V_m}$.

Figure 2.7 shows the Jaynes-Cummings ladder. The Jaynes-Cummings ladder describes the states in the strong coupling regime with a coupling constant g, and for $\Delta = 0$.

All results presented in this thesis were obtained from QD coupled with

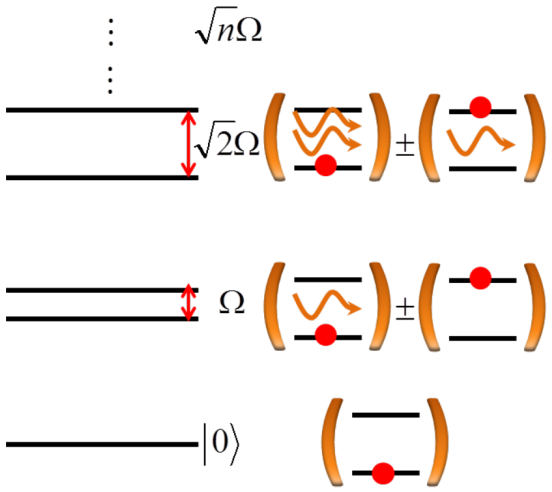

Figure 2.7: The Jaynes-Cummings ladder.

a cavity in weak coupling regime. The strong coupling regime is only presented here for the completeness of the Optical Cavity section.

Chapter 3

Experimental methodology

3.1 Introduction

To study a QD coupled with a photonic crystal cavity, sophisticated techniques were used in order to overcome the many challenges that this system presents. In this chapter all techniques used throughout this thesis will be described.

To measure the coherent quantum states of the QD, the sample is held at cryostat temperatures (4.2 K). Therefore, potential sources of decoherence are minimised. The QD states are controlled optically, using a pulse laser shorter that the T_2^* coherent time (see section 2.6.1). To perform time–resolved measurement a new two pulse resonance fluorescence technique was developed (see section 4.2).

In previous studies conducted by the author's group the signal was read out electrically, through the photocurrent technique. However, as the QD is now coupled with a cavity, the signal in this work is read out optically, by resonance fluorescence. This requires a cross–polarised setup (see section 3.5.2). To further suppress the laser scattered light the new technique, differential resonance fluorescence (DRF), was developed. This technique is described in section 3.5.3.

Resonance Fluorescence technique has two main advantage relative to the photocurrent technique: *i*) it is a spectral resolved technique and, *ii*) it works at lower fields, because the dephasing is not limited by the tunnelling rates.

3.2 Sample

The results presented in this thesis were obtained from measurements performed on the QD–cavity system in Sample BR014. This sample was cleaved from the VN2668 single-quantum dot wafer, grown in the EPSRC National Centre for III–V Technologies in Sheffield by Dr. Edmund Clarke. A layer of self–assembled InGaAs QDs were epitaxially grown in a GaAs membrane. The full structure is shown in fig. 3.1. This is a *p*–*i*–*n* diode. Thus, the QD can be tuned by the QCSE. The *p*–*i*–*n* diode is discussed in detail in the next subsection. To suppress the tunnelling of the carriers, doped tunnelling barriers of AlGaAs with $45\,,\mu$m of thickness were grown below and above the QD layer. These barriers maximised the QCSE tuning range. A p^- doped GaAs layer (nominal Be, density 2×10^{19} cm^{-3}) of $45\,,\mu$m thickness was deposited above the top barrier and a n^+ doped GaAs layer (nominal Si, density 2×10^{18} cm^{-3}) of $45\,\mu$m thickness

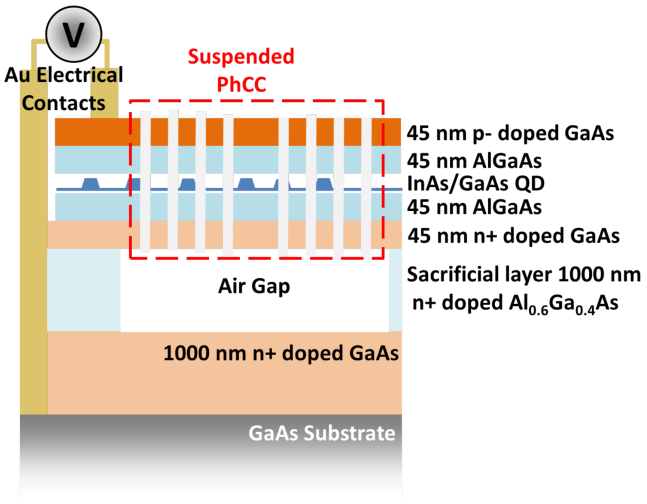

Figure 3.1: Schematic structure of BR014 Sample.

was deposited below the lower barrier. At the bottom a sacrificial layer of n^+ doped AlGaAs and a n^+ doped GaAs layer, both 1 μm thick were deposited. A suspended photonic crystal cavity was fabricated on the sample. This will be explained in section 3.2.2.

3.2.1 *p–i–n* diodes

To tune the QD energies by the QCSE, *p–i–n* diodes were fabricated on the sample, as mentioned above. Arrays of Au p-type and n-type contacts were fabricated, by ultraviolet (UV) photolithography and metal deposition. These *p–i–n* diodes were fabricated by Dr. Ben Royal and Dr. Christopher Bentham at the EPSRC National Center for III–V Technologies in Sheffield. Figure 3.2(a) shows a photograph of the diodes in the mounting details. Each diode has 8 cavities without waveguides plus 12 cavities with the waveguides. The diode used throughout this was labelled as $S4$. The diode $S4$ was chosen because it has the best current–voltage curve. Figure 3.2(b) shows the IV curve of diode $S4$ at

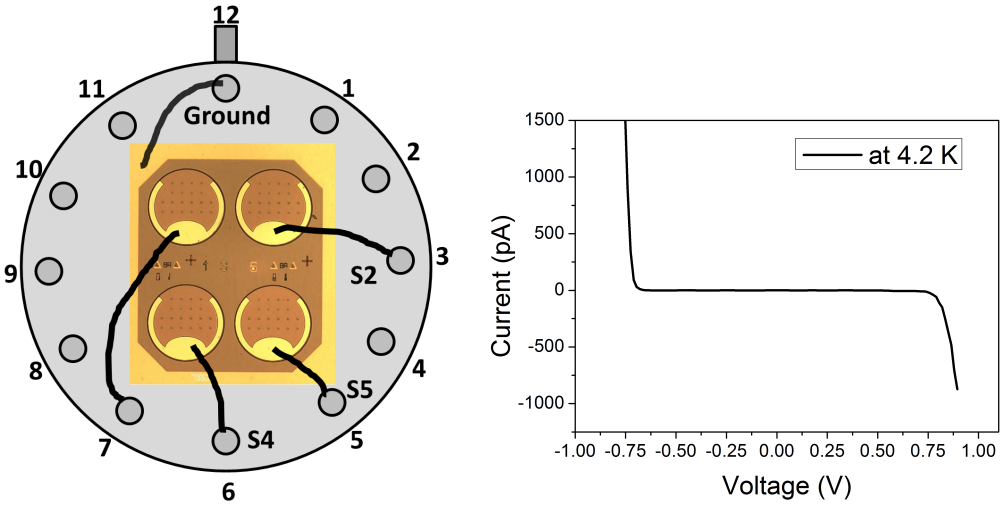

(a) (b)

Figure 3.2: a) Diode sample mounted on the holder. Each diode is connected to a pin which is, in its turn, connected to a wire. The wires were labelled as $S2$, $S4$ and $S5$. $S3$ corresponds to the ground. b) The current as a function of the bias voltage for diode $S4$.

4.2 K.

3.2.2 Photonic Crystal H1 Cavities

Photonic crystals are periodic structures of dielectric media. These structures present photonic bands, separated by band gaps. Thus, a photonic crystal is the electromagnetic counterpart of the crystalline atomic lattice. By introducing a defect in the periodic structure, it is possible to create several types of devices, such as cavities, waveguides, etc [82]. The H1 cavity is a defect photonic crystal cavity (PhCC) where one hole is missing. This defect confines the light as an optical cavity [83]. The H1 cavities have a small mode volume; therefore large Purcell factors are expected (see eq. (2.11)) The frequency and the quality factor can be controlled by the diameter of the holes and distance between them. A H1 PhCC supports two degenerate modes. However, breaking the symmetry of the structure, by adding a small shift of the pair of holes above and below the cavity, the degeneracy of the orthogonal linear polarized cavity modes is lifted (see fig. 3.4(a)).

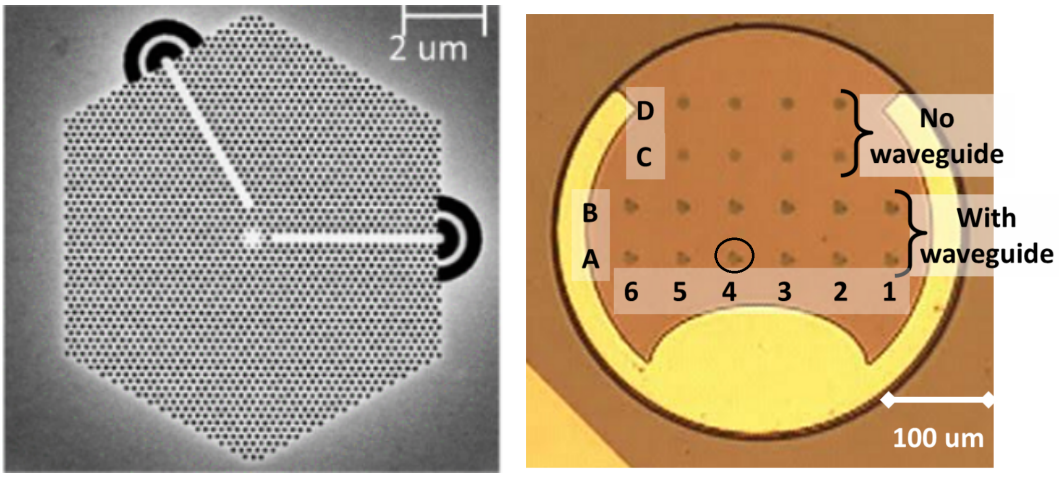

(a) (b)

Figure 3.3: a) SEM image of a H1 cavity with waveguides. b) Detail of the $S4$ diode where the cavities are visible and labelled.

The PhCCs were fabricated by Dr. Ben Royal at the EPSRC National Centre for III-V technologies in Sheffield. The PhCCs were patterned by Electron Beam Lithography and then etched by the Inductively Coupled Plasma techniquee. The sacrificial AlGaAs layer was etched away by immersion in 40% Hyrofluoric Acid (HF) solution to leave a suspended PhC membrane 200 nm thick (see fig. 3.1). The full details of fabrication of this PhCC is presented in [84, 85].

Figure 3.3(b) shows the array of H1 PhCCs that were fabricated in each diode. The two rows on the top (D and C) are single H1 cavities; the two rows on the bottom (A and B) are H1 cavities coupled into two W1 defect waveguides (see fig. 3.3(a)). Each waveguide couples a different orthogonal cavity mode and they are at 120^0 to one another. This sample had been studied to demonstrate exciton spin readout [84] and single photon routing [85].

The cavity under study is labelled as $A4$ (see fig. 3.3(b)). This cavity is coupled into two waveguides (see fig. 3.3(a)). For this cavity the relationship between the PhCC slab height, $h = 200$ nm, and the period, a, was selected as $h = 0.85a$ ($a = 232$ nm); the hole radius, r, varied between $0.31a$ and $0.34a$ (*i.e.* between 73 nm and 80 nm). This cavity is similar to the designs presented in [86]. The cavity was aligned with the crystal axes, [110] and $[1\bar{1}0]$ (x and y axes, respectively), so that the QD eigenstates match with the orthogonal linear polarized cavity modes.

Photoluminescence (PL) measurements on the cavity were performed using an off-resonant continuous-wave (CW) excitation ($E_{\text{Laser}} = 1.55$ eV). The results are shown in fig. 3.4. The cavity has two orthogonal linear polarized modes, at 1.3545 and 1.3568 eV, labelled by $M1$ and $M2$, respectively. The Q-factor of the two modes are 539 and 764, respectively (see fig. 3.4(a)). The Q-factor is obtained by $Q = E/\Delta E$, where E is the central energy and ΔE is the linewidth of the mode. By tuning the exciton energy by the QCSE, a sharp increase in the low

power, PL intensity is observed when the QD is resonant with the lower energy cavity mode ($M1$) (see fig. 3.4(b)). This is evidence that the QD is coupled to the cavity. This enhancement of the QD emission is called Purcell enhancement [73]. The Purcell effect was introduced in section 2.7.1.

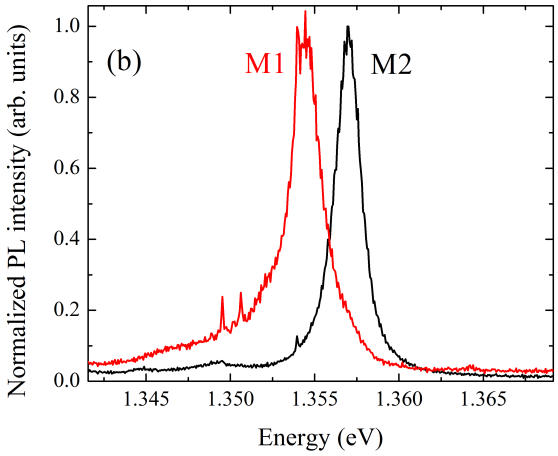

(a)

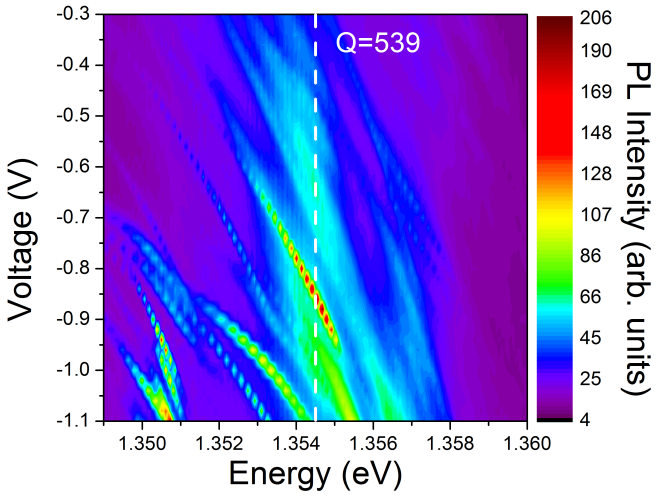

(b)

Figure 3.4: a) PL spectrum measured at a high laser power 10 mW and excitation energy $E_{\text{Laser}} = 1.55$ eV. Two orthogonally polarised modes labelled M1 and M2 are observed. b) PL intensity as a function of energy and bias voltage measured at a low laser power 10 μW and excitation energy $E_{\text{Laser}} = 1.55$ eV. The PL intensity of a QD increases significantly when it is tuned through the cavity mode. The dashed white vertical line indicates the position of the mode $M1$.

3.2.3 Cryostat

To maintain the low temperatures required for coherent control measurements of a QD, the sample is held in a bath cryostat. The cryostat is in a 50 l reservoir of liquid helium, which is encased by a vacuum chamber. To avoid environmental vibrations the cryostat is placed at an anti damping system. The sample, the piezo stages and the objective lens are mounted in a cage system built from cage rods and cage plates (Thorlabs). The cage system is inserted in a tube with a glass window at the top, permitting optical access to the sample. The tube is sealed and pumped to a high vacuum. Afterwards, a small amount of helium gas is added (< 10 cm^3) to allow thermal exchange between the sample and the helium bath. Thus, the sample temperature can be maintained at 4.2 ± 0.05 K for 15 days. Figure 3.5 shows schematically the sample inside the cryostat.

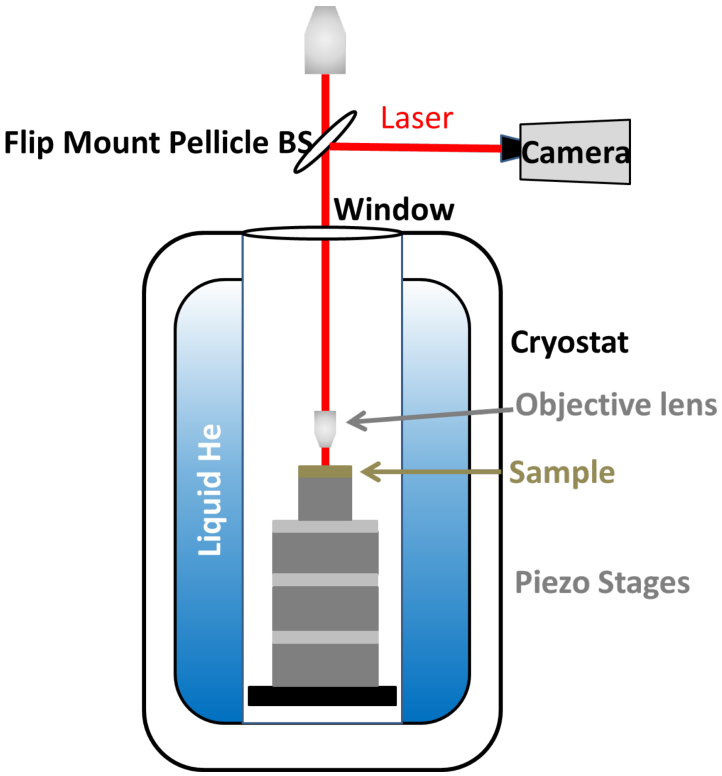

Figure 3.5: Schematic representation of the sample inside the cryostat

3.2.4 Sample mounting

The sample is mounted on to a T0-5 header allowing for electrical connections. The p-type and n-type contacts are connected to the external circuit by Au wires bonded to the contacts (see fig. 3.3(b)). The header with the sample is mounted on to the stack of piezo stages. The piezo stages allow fine control of the sample position relative to the laser spot. For the purposes of temperature dependent measurements, a resistive heater and temperature (Lake Shore Cernox) were attached to the sample mount. By implementing a Proportional-Integral-Derivative (PID) feedback algorithm, the temperature can be stabilised between 4.2 and 70 K with an accuracy of 1 mK.

3.3 Two Pulse Setup

The optical setup used to perform the measurements presented in this thesis is schematically illustrated in fig. 3.6. The laser generates ultrafast pulses ($<$ 100 fs). These pulses are split in two arms, where the bandwidth, wavelength, polarization, power and arrival time of each pulse is controlled independently. These ultrafast tunable pulses are ideal for coherent control measurements.

3.3.1 Ultrafast Laser

The laser source used was a tunable ultrafast Ti:sapphire (Coherent Mira 900, pumped by Coherent Verdi G10 laser). In mode–locked operation, the laser emits ultrafast pulses with a duration of 80 fs and a bandwidth of $\approx$ 16.2 nm at 76.2 MHz repetition rate (13.2 ns temporal pulse separation). The average output power at 915 nm ($\approx$ wavelength of the QD-cavity system under study) is $\approx$ 1 W.

To maintain the output stability the Ti:Sapphire laser operates at 17^{o}C.

To keep this constant temperature the laser is cooled by deionized water chiller. The laser was also purged with dry N_2 to prevent absorption by water vapour in the atmosphere (humidity level < 3 %).

3.3.2 Pulse Shaper

To prevent addressing other QDs in our medium density sample, spectrally narrow pulses are required (FWHM$\ll$ 1 meV). Narrow pulses can be achieved by using a $4-f$ pulse shaper. The pulse shaper design is shown in fig. 3.7. The first diffraction grating (1200 lines mm^{-1}) spreads the spectral components of the input beam spatially. The first lens (focal length $f = 500$ mm) spaced at f

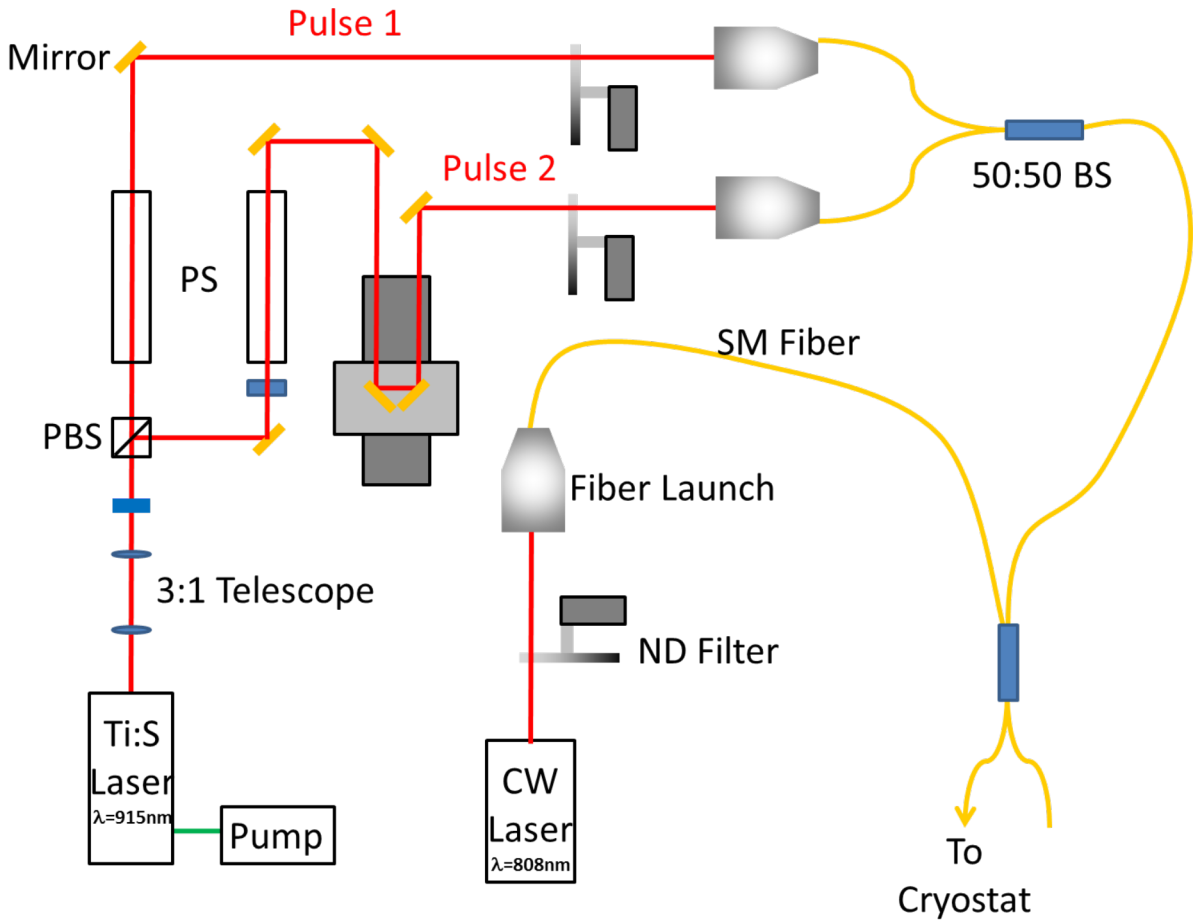

Figure 3.6: Experimental two pulse setup (optical bench).

from the diffraction grating, collimates the spread of the beam in the horizontal plane and focuses on the vertical plane. To prevent pulses with a high top–hat character in frequency domain and a $sinc^2$ temporal dependence, the motorized split (Newport linear translation stages MFAPP, MFA-CC or M-MFN25CC, 25 mm travel) is not positioned exactly at distance f, but is shifted by a small distance (dx) from the focal plane. This gives Gaussian shape pulses in both frequency and time. The slit only transmits a small fraction of the frequency components. The width and position of the slit defines the bandwidth and the central frequency of the narrow pulse beam. The second half of the pulse shaper is a mirror image of the first half. Thus, the second half of the pulse shape spatially recombines the spectral components of the beam. In case of no slit, the output beam should be the same as the input beam ($4-f$ zero dispersion pulse shaper).

3.3.3 Delay stage & power control

To measure the time dynamics of the QD in the cavity, pump–probe measurements are performed [87, 88]. The control of the delay time between these two beams allows measurement of the dynamics. This delay is obtained by chang-

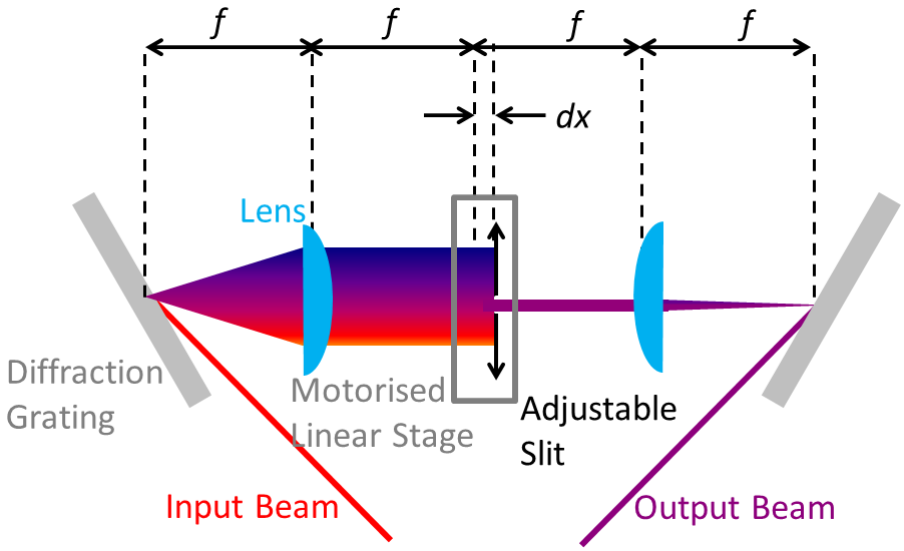

Figure 3.7: Schematic design of the $4-f$ pulse-shaper.

ing the path length of one of the arms. To control the path length a hollow retro-reflector mounted in a linear stage with 300 mm range of travel (Newport M-IMS 300) is used. Thus, an additional displacement up to 600mm is added to the optical path. This corresponds to a delay time up to 2 ns. The position of *zero time delay* is found measuring the interference that occurs when both pulses arrive simultaneously. Scanning the delay time between the two beams, each one resonant with the neutral exciton transition and with the pulse area of π, *zero time delay* occurs when the interference is maximized. The position of *zero time delay* was found at 125.9mm, for the setup used throughout this thesis.

Power dependence measurements, among others, require fine control of the input power. The power control is obtained by using circular a graded ND filter, with an OD between 0 and 4 depending on the angle, mounted on a motorized rotational stage (Newport PR50-PP).

3.3.4 Fibre optics

The beams travel from the optical bench to the top of the cryostat through single mode fibres (Thorlabs SM800). A microscope objective (Olympus Plan achromatic 10×), mounted in a high precision x , y and z translation stage (Elliot Scientific Gold series xyz flexure stage) is used to couple the beam into the fiber. The coupling of the beam into the fiber is the biggest source of power loss for the short lengths used in this experiment ($<$ 3 dB/km, plus 1.5 dB loss per connector). The microscope objective was chosen to match the numerical aperture (NA) of the fiber. Angled fibers are used whenever possible to avoid back reflections. The back reflection can reduce the stability of the laser.

3.4 Continuous-Wave Non-Resonant Excitation

Non resonant excitation was used to perform the CW characterization measurements. A diode laser (Thorlabs LD808-SA60) is used. This diode produces a beam at 808 nm with a power up to 60 mW. Figure 3.6 also shows the scheme of the CW setup.

3.5 Detection

The electron–hole pair is photogenerated by exciting the QD with a pulse laser. Then one of the following two things can occur: *i*) each carrier tunnels out of the QD, resulting in a photocurrent (Photocurrent regime), or *ii*) the hole and the electron emit a photon by radiative recombination (Photoluminescence regime). The Photocurrent technique was used previously in the author's group [42, 60]. In this thesis, the detection is based on Photoluminescence (PL). The detection regime is defined by the competition between the tunnelling and radiative time. If the carriers tunnel faster than the radiative recombination, the QD is in Photocurrent regime, otherwise it is in PL regime. The tunneling time can be made longer by incorporating tunnelling barriers below and above the QD layer (see section 3.2). Furthermore, in a high forward bias the carrier tunnelling time increases, because forward bias tilts the valence and conduction bands in such a way as to the electric field experienced by the carriers. The electric field (F) applied to the sample is given by [37, 89]:

$$F = \frac{V - V_{bi}}{W}\,, \tag{3.1}$$

where V is the applied bias (positive for forward bias and negative for reverse bias), V_{bi} is the built-in voltage of the diode which corresponds to 1.52 V (band

gap of GaAs) and W is the width of the intrinsic region (200 nm). The PL of neutral exciton of the QD under study is visible for the voltage range of 0.25–0.93 V, which corresponds to an electric field range of 3.33–3.15 kV/cm. At lower voltage than 0.25 V the photocurrent dominates and at higher voltage than 0.93 V, a carrier is injected into the dot, resulting in a charged state of the QD.

3.5.1 Resonance Fluorescence vs Photoluminescence

Photoluminescence (PL) is generated following non–resonant excitation, in this case above band gap excitation. This excitation creates carriers. By non radiative processes the carriers decay to lowest available state and eventually create a exciton. Then, by radiative recombination of the electron and the hole, light is emitted. Resonance fluorescence (RF) is a similar process, except that the laser is resonant with the exciton. The QD is excited with a resonant laser. This creates an exciton directly. A radiative recombination of a hole and an electron results in the emission of a photon with the same frequency as the laser. An important difference between the PL and RF is the relation between the polarizations of the excitation laser and the photon emitted. The RF is a polarization preserving technique, whilst, the PL preserves the polarisation, depending on which excited states are excited [90].

The biggest challenge in RF measurements is to separate the photon of radiative recombination of the exciton from the excitation laser. In order to do this, the cross polarization method and Differential Resonance Fluorescence techniques were used. These are discussed below.

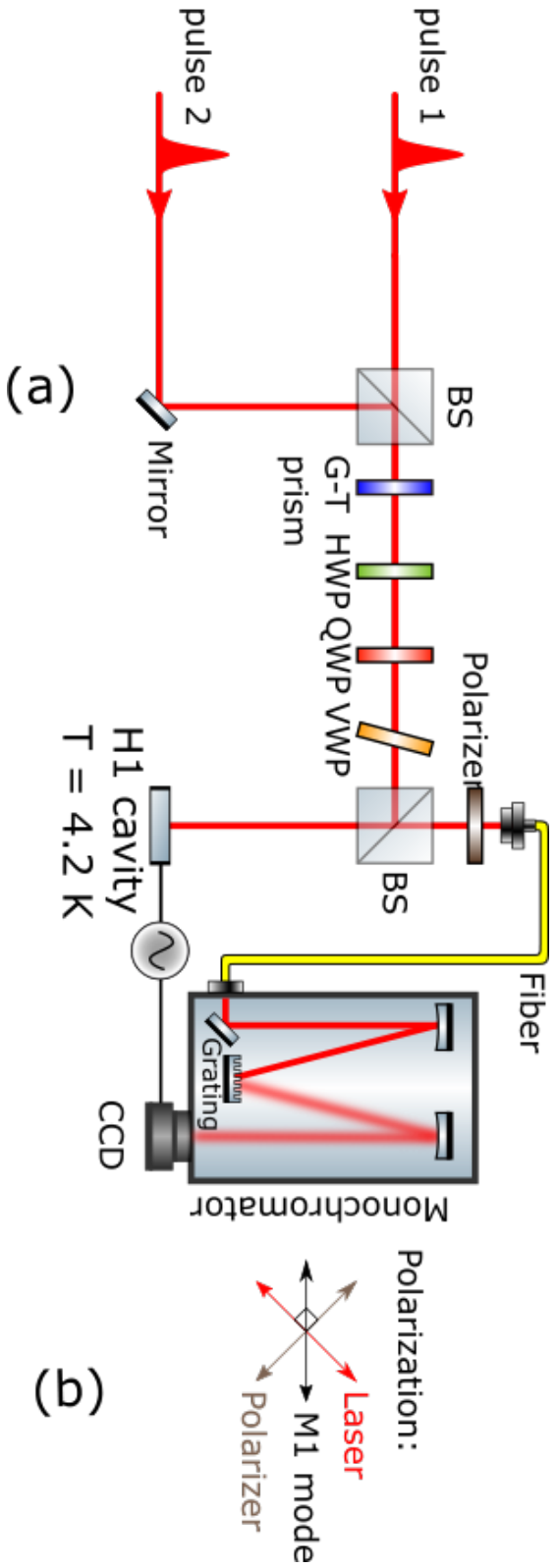

Figure 3.8: a) Experimental RF Setup using two pulses. b) The polarization scheme of laser excitation and the cavity mode.

3.5.2 Cross Polarization Method

In section 3.3, the experimental setup in the optical bench was described. This explained how the excitation pulses were generated and how the band width, energy and delay time were controlled. Through a single mode fibre the pulse traveled from the optical bench to the breadboard on top of the cryostat. Figure 3.8 shows a schematic drawing of the breadboard. The exciation polarisation is set using a Glan–Thompson polariser prism (extinction ratio–100000 : 1). A quarter wave plate, a half wave plate and a variable wave plate help to optimise the laser suppression (i.e. increasing the extinction ratio). A cube beam splitter combines the beam into two different paths. One of the paths ends in a power meter (Coherent FieldMaster GS), to monitor the excitation power. The other one guides the beam to the sample through the cryostat. The polarisation of the excitation laser is 45^0 degrees relative to the crystal axes as shown in fig. 3.8 (b). In the same way as the eigenstates of the QD, the two orthogonal linear polarised cavity modes are aligned along the in-plane crystal axes [110] and $[1\bar{1}0]$ (x and y axes, respectively). Thus, the eigenstates of the QD are co–polarised with the cavity modes. This was deliberately done during the device fabrication. As the excitation is 45^0 degrees relative to the cavity mode M1, the laser excites $1/\sqrt{2}$ component along M1. Then the emission from the QD–cavity system travels from the same path and QD-cavity RF signal passes through the linear polariser. The linear polariser is cross–polarised relative to the polarisation of the excitation. In this way, the light from the scattered laser was filtered, so that only the light emitted from the QD was detected.

The emitted light travels through a single mode fiber and is sent to a grating spectrometer and is detected by a back illuminated deep-depletion (high QE–up to 90%) Charge-Coupled Device (CCD) detector (Princeton PyLoN 400BR). The spectrometer and CCD setup was calibrated using a Neon Argon spectral

lamp. The spectral resolution of the spectrometer is $< 20\,\mu$eV.

At low powers, the signal to noise ratio using only the cross polarisation method can be $40:1$ (see fig. 3.9(a)). This value is lower than for the CW case, because the laser suppression is highly dependent on the laser frequency and the ultrafast laser pulse contains a bandwidth of frequencies. Moreover, some optics add an elliptic characteristic to the polarisation, as for example the beam splitter. Because of the poor laser suppression and the fact that signal noise ratio decreases quickly by increasing the excitation laser power, the Differential Resonance Fluorescence (DRF) technique, described in the next section, was also developed to isolated the RF signal.

3.5.3 Differential Resonance Fluorescence

To further increase the signal to noise ratio, the DRF technique was used. The DRF modulates the voltage to enable measurements of the spectrum where the laser is resonant with QD (see red line of fig. 3.9(a)) and another spectrum where

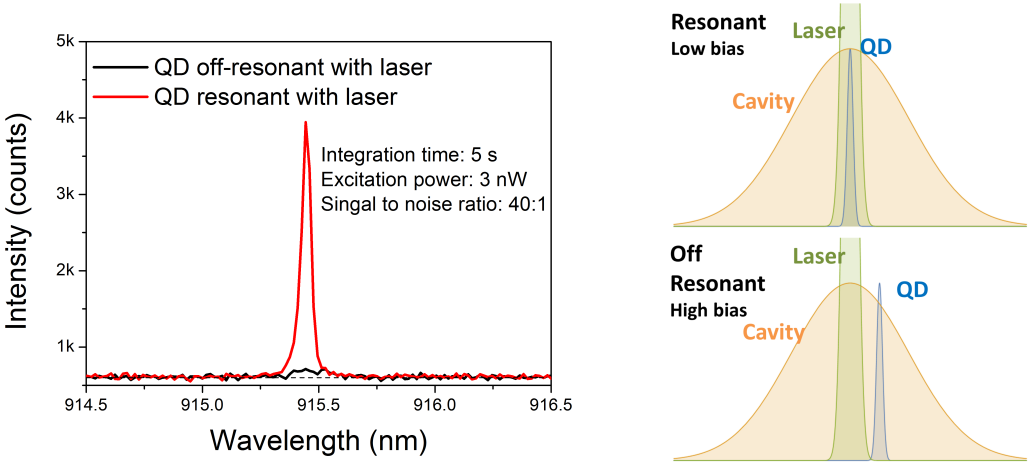

(a) (b)

Figure 3.9: a) Cross Polarization Method: Spectrum measured with QD resonant (red line) and non resonant (black line) with the pulsed laser. b) Scheme of the relative spectral position of Laser, QD and Cavity for QD resonant (top) and off resonant with laser (bottom).

the QD is tuned away from the laser by the QCSE (see black line of fig. 3.9(a)). Figure 3.9(b) shows the DFR measurement scheme, when the QD is resonant (top) and off–resonant (bottom) with the laser. The subtraction of these two spectra gives the signal due to QD alone. This is because the cavity scattered laser light is not sensitive to a small changes of bias. Figure 3.10 shows the QD and cavity energy as a function of the bias voltage. The QD energy can be tuned 1.7 meV for a voltage range of 0.7–1.00 V. For the same voltage range the cavity only tunes 0.02 meV. The small variation of cavity energy as a function of the voltage bias can be visible in the inset of fig. 3.10. This is mainly caused by a small change of refractive index with field.

To perform this differential technique, a function generator (Tektronix AFG3000) was used to generate a square wave–bias function. This switches the

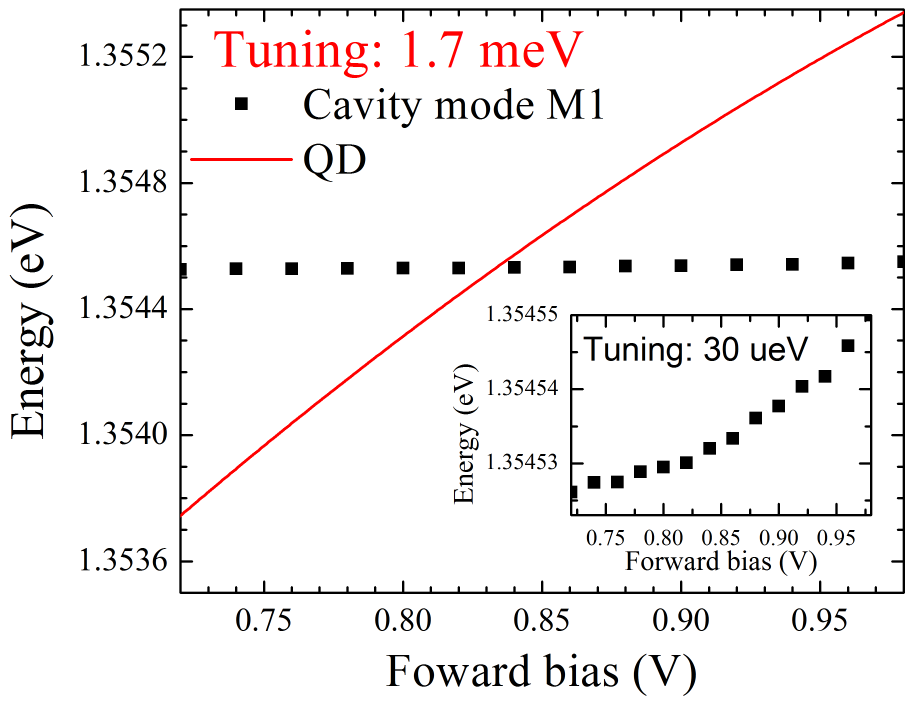

Figure 3.10: QD and Cavity energy as function of voltage bias. Inset: Zoom in of the cavity energy as a function of voltage bias.

QCSE of the dot, and the voltages were chosen so that low bias corresponds to the dot on resonance with the laser, and the high bias to the case with the dot blue detuned. In this way, phonon-assisted excitation was avoided for the off–resonant case. This is because phonon-assisted excitation only occurs if the QD is tuned to lower energies than the laser [59]. In this situation, the laser is blue–shifted detuned relative to the QD, and can create an exciton by phonon–assisted excitation, as explained in section 2.6.4. Such phonon–assisted excitation is not possible if the dot is blue–shifted relative to the laser in the off resonant case. Using a Trigger–Type Logic (TTL) signal with frequency $2f$, the CCD detector is triggered at each new exposure (blue rectangles of fig. 3.11) on each rising edge. The TTL signal also synchronises the square–wave from the function generator, which applies bias to the device, with the CCD exposure time detection. To minimize the noise fluctuations and maximize the signal to noise ratio, the differential RF was modulated at a low frequency (22 Hz) and many frames were measured. This frequency was fast enough to cancel the noise fluctuation due to the drifts in laser suppression and power, and at same time slow enough for the integrated RF signal acquired to be large enough to be distinguished from the CCD background. Figure 3.11 shows the temporal scheme of the Differential

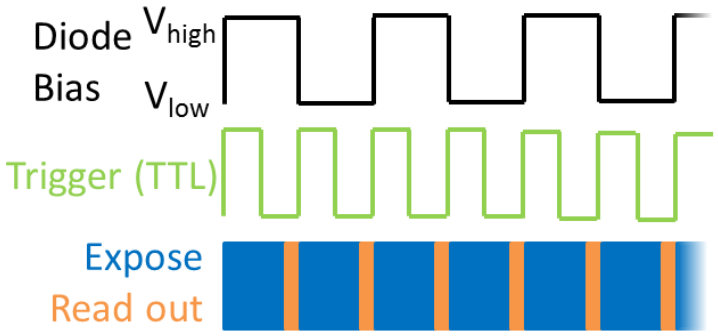

Figure 3.11: Bias Modulation Scheme–the diode bias shifts the QD from resonant (V_{high}) to off-resonant (V_{low}) with the laser. A phase locked ($\phi = 0$) TTL signal with frequency $2f$ triggers the CCD detector at each new exposure (blue rectangles) on each rising edge. The TTL signal also locks the square–wave coming from the function generator with the CCD exposure time detection.

Resonance Fluorescence technique.

3.6 Hanbury Brown Twiss Setup

To confirm that the QD is a good single photon emitter, the second order of correlation was measured ($g^2(\tau)$). To perform this measurement the Hunbury Brown Twiss setup was used (see fig. 3.12). The second order of correlation ($g^2(\tau)$) measures the coincidence probability of a pair of photons as a function of time, τ. To measure the second order of correlation ($g^{(2)}(\tau)$), the signal coming out from the spectrograph was passed through a motorised split which allowed selecting of QD wavelength, filtering the background. This helps to improve the signal to noise ratio, which has to be very low to perform this measurement successfully. Then, the QD signal is split using a beam splitter. Each arm guides the QD signal to an Single Photon Avalanche Photodiode Detector (SPAD). The SPADs were triggered by the laser pulse signal. The coincidence counter receives the signal from both SPADs and measures the coincidences. This coincidence counter scanned the time delay between the APDs' signal. The second order correlation gives information about the quality of the QD as a single–photon source.

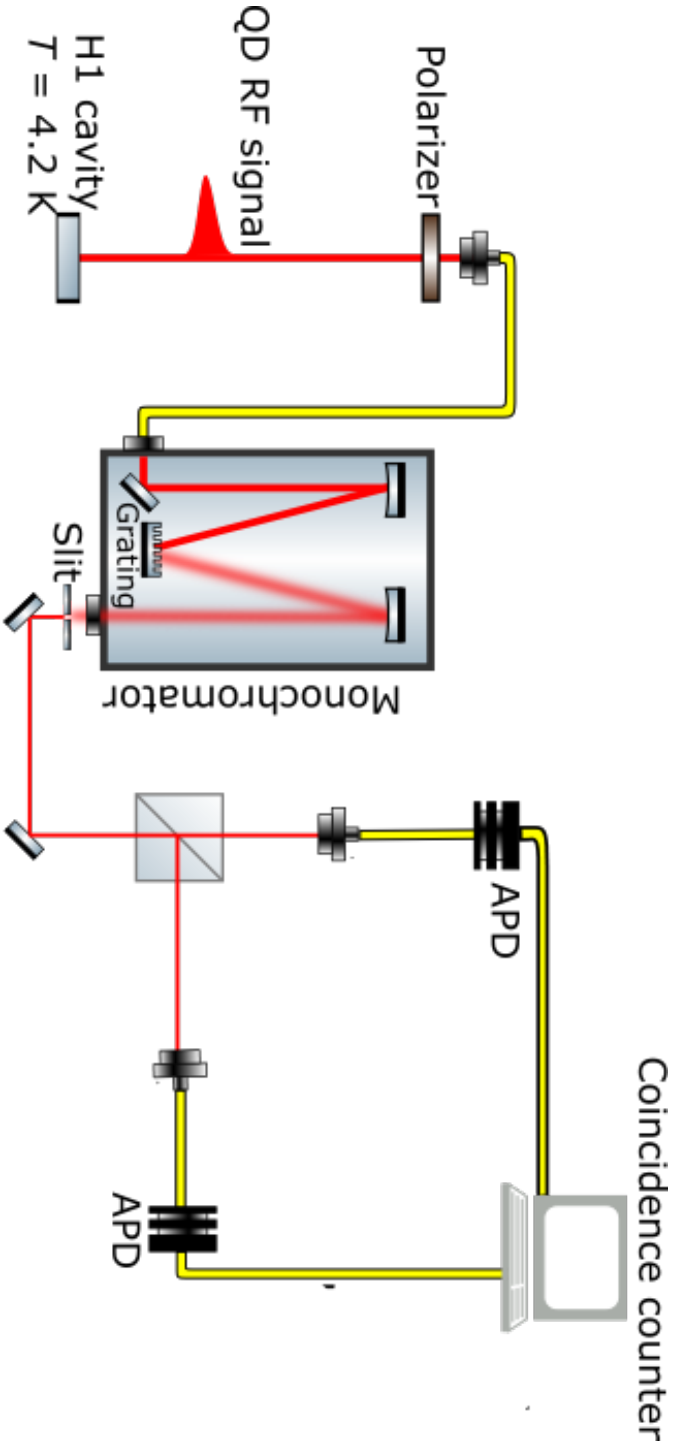

Figure 3.12: A simplified scheme of the $g^{(2)}$ setup

Chapter 4

On-Chip On-Demand Tunable Single Photon Source

4.1 Introduction

Integrated quantum photonics has made great progress in recent years. However the scaling issue remains unsolved. Scalability is a requirement for Quantum Information Processing. Quantum interference between silicon photon-pair sources on–chip has been demonstrated [91–101]. As the pair of photons are obtained from probabilistic down-conversion processes, this requires such a large space and optical power, as to preclude allowing the scalability to large N. On the other hand, single photon sources based on QD do not require large space and low optical powers, as they offer nearly ideal performance in free space [69,70,102–105]. On–demand QD single photon sources with low multiphoton probability ($g^{(2)} \approx 0$) and high indistinguisability ($T_2 \approx 2T_1$) have recently been observed [70,106].

However the issue of integrating this photon emitter in a quantum circuit remains. The charge noise from the etched surfaces close to the QD induces de-

phasing which degrades the coherence of the photons emitted [39]. As mentioned in eq. (2.9), the total dephasing time is given by:

$$\frac{1}{T_2} = \frac{1}{2T_1} + \frac{1}{T_2^*}\,, \tag{4.1}$$

where T_2^* is the pure dephasing time and T_1 the exciton lifetime. One way to achieve a high coherent single phonon source is by reducing the exciton lifetime in such a way that the short exciton lifetime overcomes the dephasing ($1/2T_1 \gg 1/T_2^*$), restoring the coherence of the photon emitter ($T_2 \approx 2T_1$) [107]. The indistinguishability, which is determined by the ratio $T_2/2T_1$ is then ideal. Similar approaches have been implemented, but not very successfully, owing to the modest Purcell factor (around 10) [74, 75]. These modest Purcell factors are owing to the exciton lifetimes being measured using a band–gap or a p–shell excitation [108]. Such excitations cause a carrier relaxation time jitter. Therefore, the photon coherence time had to be much larger than the incoherent carrier relaxation time jitter (about tens or hundreds of ps) [109].

In this chapter, a waveguide-coupled Photonic Crystal Cavity (PhCC) is used to strongly reduce the radiative lifetime ($T_1 = 22.7$ ps) of the QD. To avoid the time jitter associated with the relaxation, a resonant excitation method was used. To measured such short lifetimes the Two Pulse Resonance Fluorescence (TPRF) technique was developed. Therefore, a strong Purcell factor (42) is reported. To confirm the high coherence of the QD emission, the autocorrelation and Hong–Ou-Mandel (HOM) [110, 111] measurements were performed by exciting the QD from cavity and detecting the RF signal from the outcoupler. These measurements were carried out by J. O'Hara and A. Brash, and are briefly presented here to support the results of this research. Thus, high purity (86%) and high indistinguishability (90%) were obtained on–demand and on–chip. These results confirm that this device is a near–ideal single photon source on–demand

and on–chip.

A manuscript about this work was recently submitted in Nature Nanotechnology.

4.2 Two Pulse R.F. Technique

To measure the very short exciton lifetime, a novel technique was used. This technique is similar to the inversion recovery measurements reported in [87, 88]. The Two Pulse Resonance Fluorescence (TPRF) technique consists of two beams with pulse area of π and resonant with the QD (see fig. 4.1(a)). The delay time between these beams is scanned. The first beam creates the exciton ($t = 0$). By radiative recombination the exciton population decays as a function of time ($t \leq \Delta t$). After a time delay Δt the second beam arrives. If $\Delta t = 0$, both beams arrive simultaneously. The first beam creates an exciton but the second beam de–excites it (equivalent to 2π pulse). No RF is detected. If the time delay between the beams is shorter than the exciton lifetime, the second beam still finds the QD partially populated and de–excites it ($t = \Delta t$). Only a fraction of the exciton created by the first pulse is detected. Otherwise, if the time delay between the beams is longer than the exciton lifetime, the second beam finds the QD empty and excites it again. Two exciton are detected in this case ($t \gg \tau_X$). Thus, the RF signal detected is proportional to the exciton population created by the first beam. This can be mathematically expressed by:

$$I(t) \propto 2\,(1 - C_X) \propto 2\left(1 - e^{-\frac{\Delta t}{\tau_X}}\right), \tag{4.2}$$

where C_X is the exciton population created by the first beam and τ_X is the exciton lifetime. The scheme of the TPRF technique is illustrated in fig. 4.1(b). The graph is symmetrical because the pulse area of both beams is the same

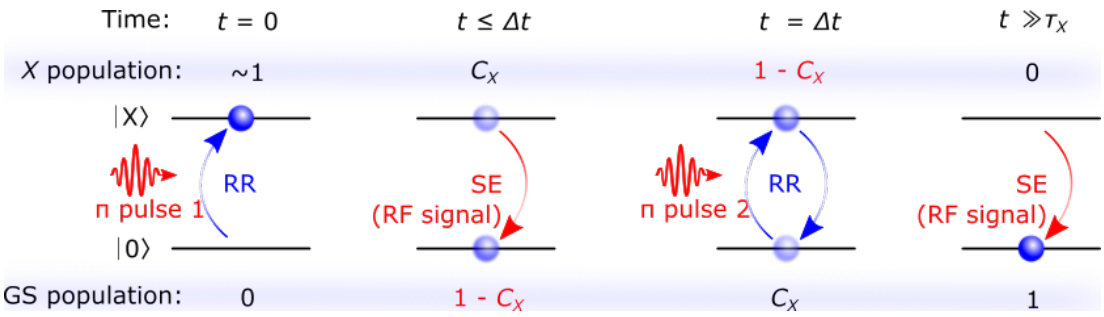

(a)

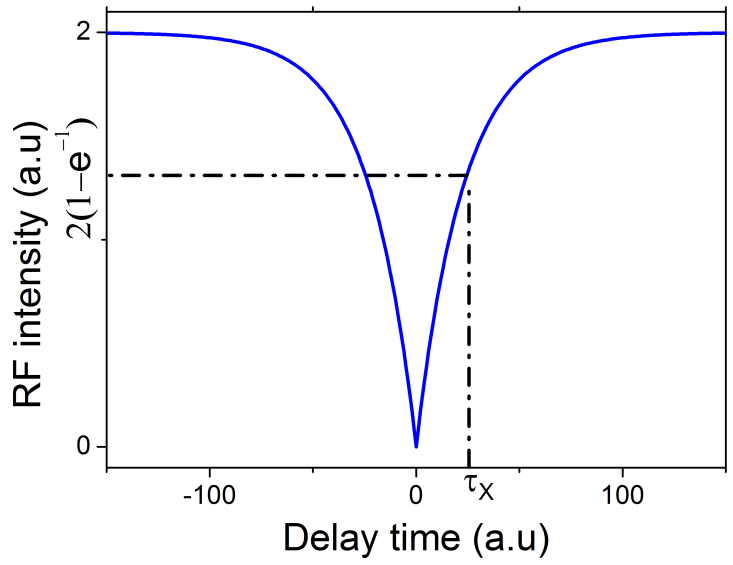

(b)

Figure 4.1: a) The principles of the TPRF technique. b) Schematic measurement using TPRF technique. The line is obtained by eq. (4.2).

($\Delta t \longrightarrow |\Delta t|$). This technique allows measurement of the time dynamics of the exciton, and consequently the exciton lifetime can be obtained.

Note that this technique is combined with the Differential Resonance Fluorescence technique (see section 3.5.3), which enables to obtain a background free spectrum.

4.3 Huge Purcell Factor

The strength of cavity on QD can be quantified by the well known Purcell factor (see section 2.7.1). In the next chapter (chapter 5) the effect of the cavity on the QD is considered in detail. To quantify the Purcell factor the exciton lifetime of the QD coupled (Γ_{cav}^{QD}) and uncoupled ($\Gamma_{\text{free}}^{QD}$) with the cavity have to be measured. The Purcell factor is then given by $F_P = \Gamma_{\text{cav}}^{QD}/\Gamma_{\text{free}}^{QD}$. However the $\Gamma_{\text{free}}^{QD}$ value of the specific QD coupled to the cavity could not be measured, as it is not possible to remove the QD from the cavity. When the QD is tuned far away (≥ 3 meV) from the cavity, either the RF signal or the oscillator strength of the QD changes. So the $\Gamma_{\text{free}}^{QD}$ had to be estimated. The exciton lifetime of a random QD uncoupled with the cavity was measured to estimate the $\Gamma_{\text{free}}^{QD}$.

4.3.1 Exciton Life Time of an Uncoupled QD

To estimate $\Gamma_{\text{free}}^{QD}$, a random uncoupled QD was found in the bulk region of the sample. The wavelength of this QD was 910 nm (at bias of 0.83 V). This QD seemed brighter than the average (spectra of this QD is plotted in fig. 4.3). This made the measurement easier, since for dim QDs the RF signal is of the same order of magnitude as the background noise. However the brightness can also indicate that the exciton lifetime of this QD is shorter than the average. Nevertheless, the TPRF technique was performed on this QD in order to measure its exciton lifetime. The time dynamics measurement is shown in fig. 4.2

In order to extract the exciton lifetime from the TPRF measurement, the data is fitted using the following function:

$$f(t) = y_0 + A\left(1 - e^{-\frac{t}{\tau_X}}\right) + B\left(1 - e^{-\frac{t}{\tau_X}}\cos\left(\omega_{\text{FSS}}t\right)\right), \tag{4.3}$$

where y_0 is the offset, A and B are the amplitudes, τ_X ($\Gamma = 1/\tau_X$) the exciton

lifetime and ω_{FSS} the FSS frequency. The first term of eq. (4.3) corresponds to the time dynamics of the exciton (same as eq. (4.2)), whilst the second term, which includes the *cosine*, corresponds to the FSS dynamics of the exciton (see section 2.3). For QDs with $\tau_X \ll \omega_{\mathrm{FSS}}^{-1}$ the second term can be neglected. FSS is observed because the eigenstates of the QD are aligned with the crystal axis, and the polarisation of the excitation beam is tilted at 45^o relative to the crystal axis. Therefore, the excitation beam excites both eigenstates, causing a Larmor precession of the QD states (see section 2.3). From this fit an exciton lifetime of $\tau_X = 575$ ps and an $FSS = \hbar\omega_{\mathrm{FSS}} = 9\,\mu$eV (see the inset of fig. 4.2) were obtained. The exciton lifetime is rather shorter than expected. This can be characteristic of this specific dot, or be because resonant excitation was used, which avoids the jitter time relaxation, as explained above.

The FSS was also measured from the time average of RF signal measured

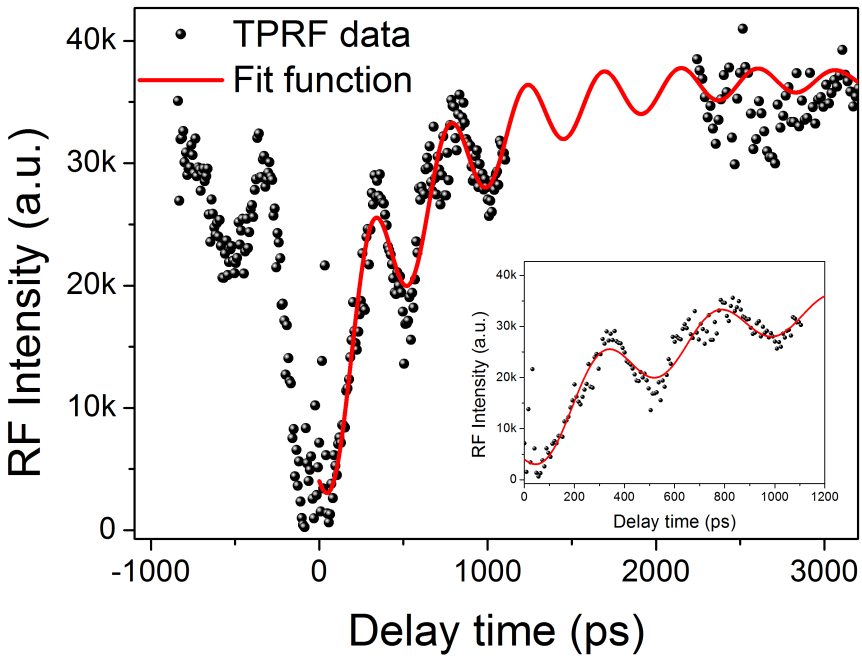

Figure 4.2: TPRF measurement for a QD uncoupled with the cavity. The red line is obtained by fitting an exponential sinusoidal damped function (see eq. (4.3)). Inset: Zoom where the oscillations due to the FS are more visible.

on the spectrometer. Rotating the polariser in the detection path, the QD PL signal can be measured as a function of the polarisation to reveal the FSS. Figure 4.3 shows the exciton peaks for two orthogonal polarisations. The peaks are centered at different energies because they are different exciton states (see level diagram of fig. 2.3). This energy difference corresponds to the FSS. In the inset of fig. 4.3, the peak energy as a function of the polarisation is shown. The FSS measured from the spectrometer was of $FSS = 8.9\,\mu$eV. This value matches closely to the value measured from the TPRF technique. The observation of the FSS proves that it is a neutral exciton, at this bias range.

At zero time delay, a peak is observed in fig. 4.2. This peak occurs because at zero time delay the two beams overlap. Thus, the overlapping results in a single

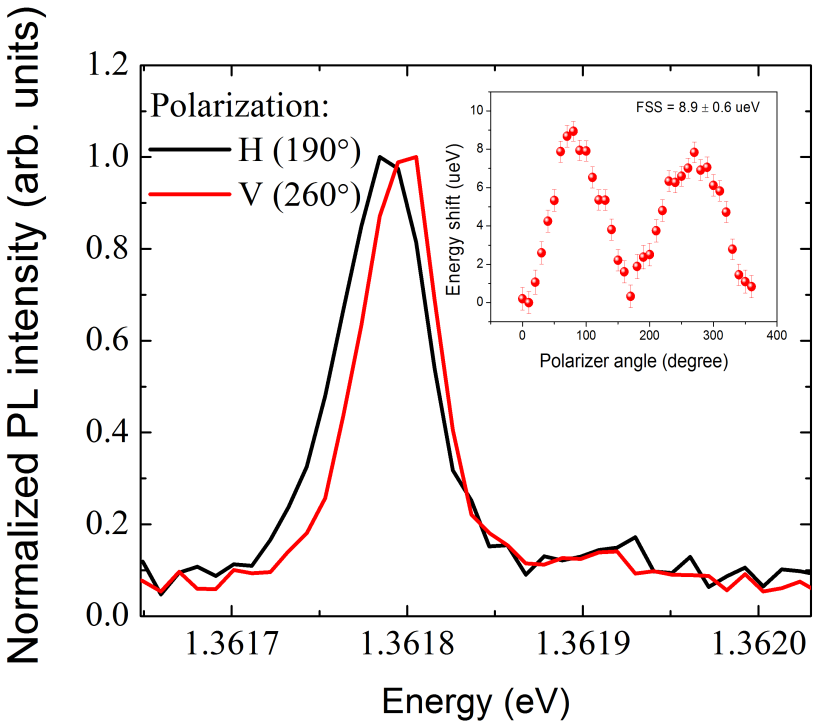

Figure 4.3: PL spectra of an uncoupled QD for two different polarisations of the polariser in the detection path. The spectra were measured under above band excitation. The excitation power was $10\,\mu$W. Inset: Relative energy position of the exciton PL peak as a function of the angle of the detection. The amplitude of the oscillation is $8.9\,\mu$eV. This corresponds to the FSS.

beam with $\sqrt{2}\pi$ of pulse area [88].

To obtain a second estimation of the exciton lifetime of an uncoupled QD, the exciton lifetime for dots in the bulk of the crystal was measured using a APD. A random area of the sample was excited with an above band gap pulsed laser excitation. Such excitation was obtained using the unshaped Ti:S laser centered at 808 nm. Many uncoupled QDs were excited and the APD detected the average PL signal as a function of the time. Thus, the average time dynamics of many QDs were measured. Figure 4.4 shows the average exciton lifetime as a function of the bias voltage for two different areas of the sample. The exciton lifetime is almost constant with the bias voltage. The average exciton lifetime varies between 0.92–1.02 ns for both areas. This value is in accordance with the values found in literature for this material QDs [29]. As an above band excitation was used, this lifetime can be overestimated due to the incoherent carrier relaxation time jitter [109, 112]. However, as the jitter time is of the order of tens/hundreds of picoseconds, it can be neglected.

The inset of fig. 4.4 shows an example of a lifetime measurement using the APD. The blue line is the instrument response function, which corresponds to the time resolution of the APD ($\approx$ 400 ps). The black circles are the PL lifetime measured at 0.83 V bias with a laser power of 5 μW. The red line is the fit using the convoluted exponential and Gaussian functions. More detail about the fit can be found in appendix B.

The average exciton lifetime measured with APD ($\approx$ 1 ns) is quite different from the exciton lifetime of a single random QD measured using the TPRF technique ($\approx$ 600 ps). The dot selected was particularly bright, shorter lifetime than the average was expected. However, as only a single random QD was measured using the TPRF technique, it is not possible to compare. What it is possible to conclude is that the exciton lifetime of a uncoupled QD is between 600 ps and

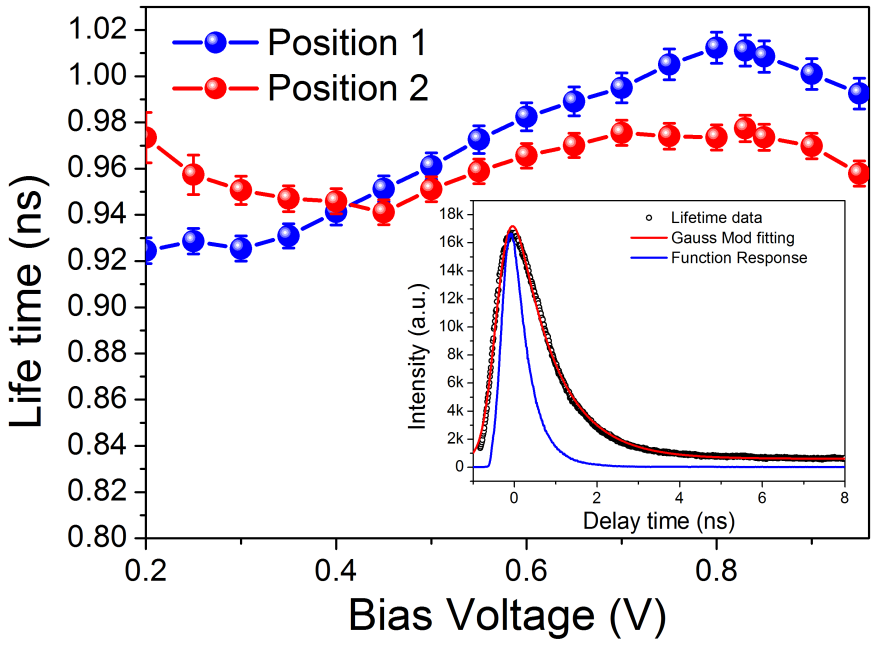

Figure 4.4: Average of the exciton lifetime of uncoupled QDs as a function of the voltage bias for above band excitation and measured using an APD. Inset: Normalized PL decay QDs measured at bias = 0.83 V (black circles). The red line is the fitting using the convolution of a Gaussian and exponential function (see appendix B). the black line is the Instrument response function.

1 ns.

4.3.2 Exciton Lifetime of the QD Coupled with a Cavity

To measure Γ_{cav}^{QD}, the TPRF technique was used (see section 4.2). The exciton lifetime of the QD was measured for different QD detunings relative to the cavity. Figure 4.5 shows the lifetime measurement for two different QD–cavity detunings. The black line was the data measured when the QD was resonant with the cavity, and the red line was the data measured when the QD was -2.5 meV detuned relative to the cavity. As is clear from fig. 4.5, when the QD is far away from the cavity resonance, the exciton lifetime is longer.

Fitting the data shown in fig. 4.5 with the convolution of an exponential

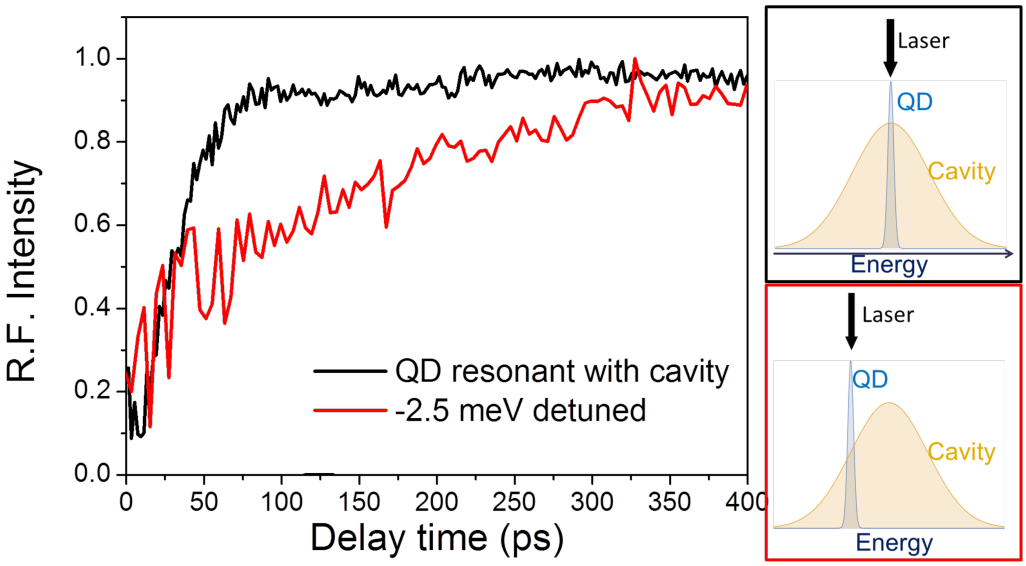

Figure 4.5: TPRF measurements for the QD resonant (black line) and −2.5 meV (red line) detuned relative to the cavity. On the right hand side are the scheme of the relative energy position of laser, QD and cavity for QD on (top) and off (bottom) resonant with the cavity.

with a Gaussian function, the exciton lifetime can be extracted (see appendix B). When the QD is resonant with the cavity (black line), the exciton lifetime is $\tau_X = 22.7$ ps. When the QD is -2.5 meV detuned relative to the cavity, the exciton lifetime is $\tau_X = 126.2$ ps. The exciton lifetime for QD resonant with the cavity is ≈ 4.8 times larger then when it is significantly detuned from the cavity. This result is consistent with the enhancement of the electric field. This effect will be discussed in chapter 5.

Figure 4.6 shows the exciton lifetime ($\tau_X = 1/\Gamma$) and the Purcell factor as a function of the QD detuning relative to the cavity mode M1. The theoretical red and blue curves were obtained from eq. (2.11) and $F_P = \Gamma^{QD}_{\text{cav}}/\Gamma^{QD}_{\text{free}}$, respectively:

$$\Gamma^{QD}_{\text{cav}} = \frac{3}{4\pi^2}\left(\frac{\lambda_c}{n}\right)^3\left(\frac{Q}{V_m}\right)\frac{\kappa^2}{4\left(\omega_{\text{QD}}-\omega_c\right)^2+\kappa^2}\Gamma_{\text{free}}\,\zeta\,, \tag{4.4}$$

where $\lambda_c = 915.315$ nm is the wavelength of the cavity, ω_{QD} the frequency of the QD, n the refractive index, $\kappa = 1.1$ meV and $Q = 539$ respectively the width

and the Q–factor of the cavity mode and $V_m = 0.65\ n^3/\lambda_c^3$ the mode volume [84, 86]. The mode volume (V_{m}) was obtained by FDTD simulation performed by Dr. R. Coles. The remaining parameters were measured (see chapter 3). $\zeta = |\mu_{1,2}E|^2/|\mu_{1,2}|^2|E|^2$ was the only fitting parameter and represents the overlap of the dipole ($\mu_{1,2}$) with the electric field (E). This includes the spectral, spatial and polarisation overlapping between the light and the QD dipole. As the QD is resonant with the cavity, the cavity mode M1 overlaps with the QD dipole. In the same way the polarisation overlapping is assumed as 1. This is because the laser excitation is tilted by 45^o relative to the crystal axes. However, as the light experienced by the QD is filtered by the cavity, and the QD eigenstates are aligned with the crystal axis, the light which reaches the QD is co–polarised with the QD. Basically the cavity works as a polariser. Therefore the polarisation overlapping is also assumed as 1. Only the spatial overlapping can vary between 0 and 1. It is 1 when the QD is positioned at the maximum electric field of the cavity. The value of ζ obtained from the fitting depends on the Γ_{free} used. If $\Gamma_{\mathrm{free}}^{-1} = 0.94$ ns (from PL lifetime measurements on QD in the bulk), $\zeta = 0.65$. On the other hand if $\Gamma_{\mathrm{free}}^{-1} = 0.575$ ns (from TPRF measurement on a specific uncoupled QD), $\zeta = 0.51$. Equation (4.4) shows that the exciton lifetime and the Purcell factor can be controlled by the cavity [113].

For micropillar cavities the Purcell factor reported was around 6 [69, 70]) and for photonic crystal cavities was around 9 [74] . This difference is due to the mode volume, which is larger for micropillar cavities. Although a Purcell factor of 28 was reported [76], the Purcell factor in these works was indirectly obtained by fitting the HOM measurement rather than direct lifetime measurement. Here a strong Purcell factor of 42, directly measured, is reported. The fact that $\Gamma_{\mathrm{cav}}^{QD}$ was so short explains why the Purcell factor reported here is so high. Such a short lifetime ($\Gamma_{\mathrm{cav}}^{QD}$) can only be measured using a resonance fluorescence technique, avoiding the time jitter added to the lifetime when an above band or p–shell

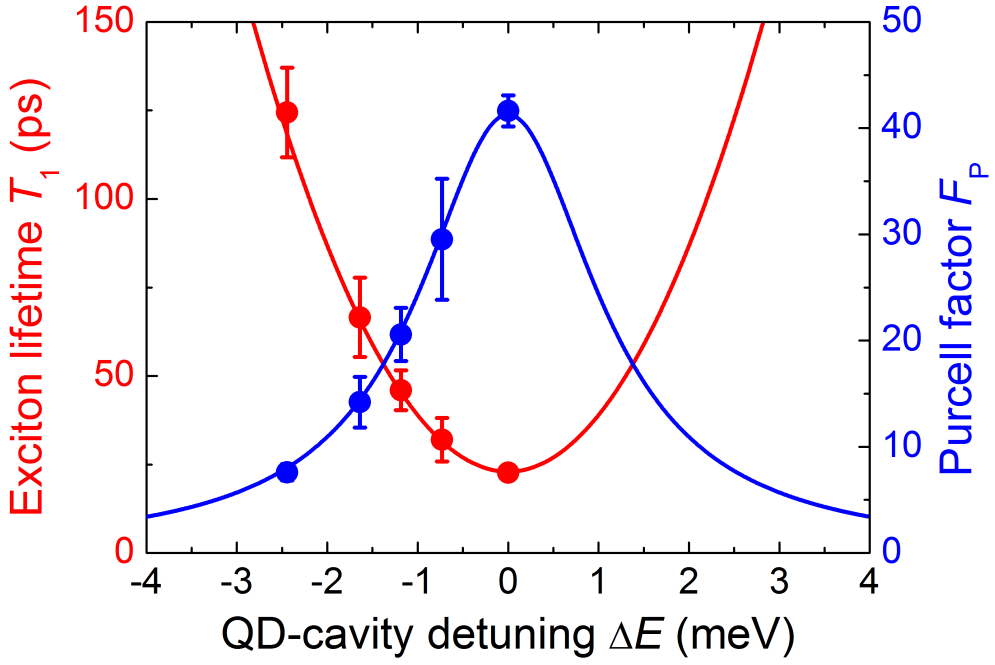

Figure 4.6: Exciton lifetime (red dots) and the Purcell factor (blue dots) as a function of QD detuning. The red and the blue line were obtained from eq. (4.4). The only fitting parameter is ζ. All of the other parameters were measured except V_{m} which was obtained by simulation.

excitation is used. The TPRF technique meets these requirements. Moreover, this technique has high time resolution; it is only limited by the laser width (see appendix B). The theoretical Purcell factor is 63, when the dipole overlaps with the electric field ($\zeta = 1$).

From the Purcell factor, the coupling strength between the QD and the cavity can be estimated. $F_P = 2g^2/\kappa\Gamma$, where g is the coupling strength, κ the leakage rate of the cavity and Γ the decay rate of the QD. Therefore, $g = 132\,\mu$eV was estimated. This is one of the largest coupling strengths reported for a weak coupling regime. A $g = 129\,\mu$eV was reported in [76]. However the Purcell factor was indirectly estimated by the HOM data fitting.

4.4 On–Demand and On–Chip Single Photon Source

The high Purcell factor leads to a near transform-limited QD. Therefore, the high Purcell-factor significantly relaxes the quality requirement of both the QD itself and the PhCC. So, for all of the following measurements presented, the QD was in resonance with the cavity. This makes this QD–cavity system a good candidate for a single photon source. To confirm this, the photon coincidence correlation, or second-order correlation ($g^{(2)}(\tau)$), was performed (see section 3.6). To measure $g^{(2)}(\tau)$, the light from the spectrometer was guided to the APDs, passing through a 50 : 50 beam splitter. However, only the QD signal must arrive on the APD. So, a motorised slit with 2 μm width was mounted on the output gate of the spectrometer. Thus, the output signal is filtered, allowing selection of only the wavelength for which the QD signal is a maximum (see fig. 3.12). Figure 4.7(a) shows spectra, obtained from the APD by scanning the central wavelength of the spectrometer, for the QD resonant (black squares) and off–resonant (red circles) with the laser. The QD is tuned electrically by the QCSE (see section 2.5.1). The inset of fig. 4.7(a) indicates that the excitation laser and the detection were both from the cavity.

The result of the $g^{(2)}(\tau)$ measurement is shown in fig. 4.7(b). The value of $g^{(2)}(0) \approx 0.12$, much lower than 0.5, indicating the that the QD–cavity is indeed a good single photon source. Only 12% of the time the APDs detected two photons simultaneously. As the lifetime is short comparable with the laser width, the QD can be occasionally re–excited to emit additional photons during the system-pulse interaction [107]. This is under resonant excitation (see the right hand side of fig. 4.7(b)), however it is not an on–demand single photon source, because the pulse area of the laser excitation was not π but 0.7π. This

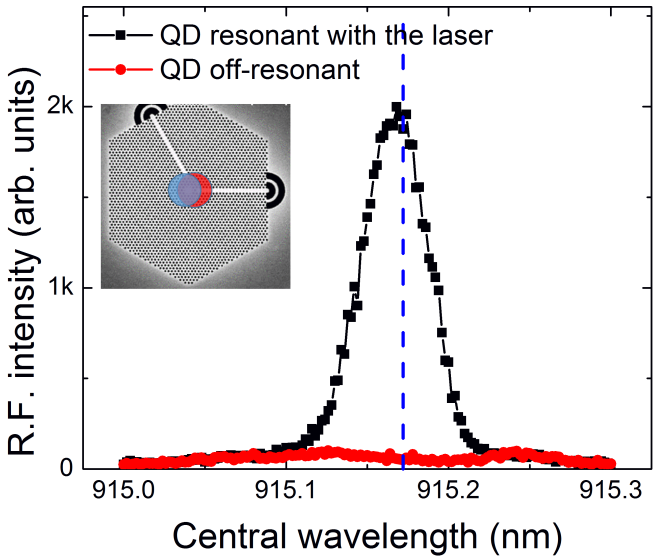

(a)

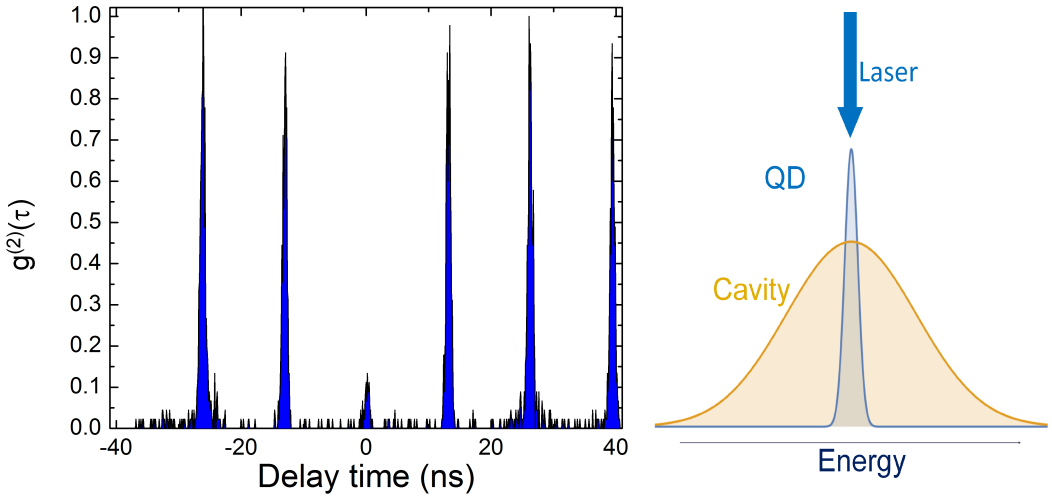

(b)

Figure 4.7: a) RF emission as a function of the central wavelength of the spectrometer for QD resonant (black squares) and off–resonant (red circles) with the laser. The vertical dashed blue line indicates the CCD pixel where the signal to background ratio is maximum (73 : 1). Inset: the configuration of the experiment. The excitation (red circle) and the detection (blue circle) of signal occurs from the top of the cavity. b) $g^{(2)}(\tau)$ measurement for a laser excitation power correspondent to $0.7\,\pi$ of pulse area. $g^{(2)}(0) \approx 0.12$. On the right hand side is the scheme of the QD, cavity and laser energy position. In this case, the laser excites resonantly the QD, which is resonant with the cavity.

means that not every time the QD is excited does it emit a photon. So low laser excitation power was chosen to optimise the signal to background ratio. In this experimental configuration, both excitation and detected RF come through the top of the cavity (see inset of fig. 4.7(a)). The signal to background ratio is too low to perform the $g^{(2)}(\tau)$ measurements for higher pulse areas than 0.7π.

As one way of avoiding laser scattering, the QD can be excited from the phonon side band (chapter 5). The experimental configuration is shown in the right hand side of fig. 4.8). Thus, the laser and the signal are spectrally separated, improving the signal to background ratio. Figure 4.8 shows the second-order correlation for an excitation laser detuned +0.73 meV relative to the QD and a laser power of 100 nW. The $g^{(2)}(0) \approx 0.1$ is slightly better than the previous result shown in fig. 4.7(b). Once again, this is not a perfect on–demand single photon source, because, as will be seen in section 5.3.2, it is not possible to reach the population 1 from the phonon excitation process.

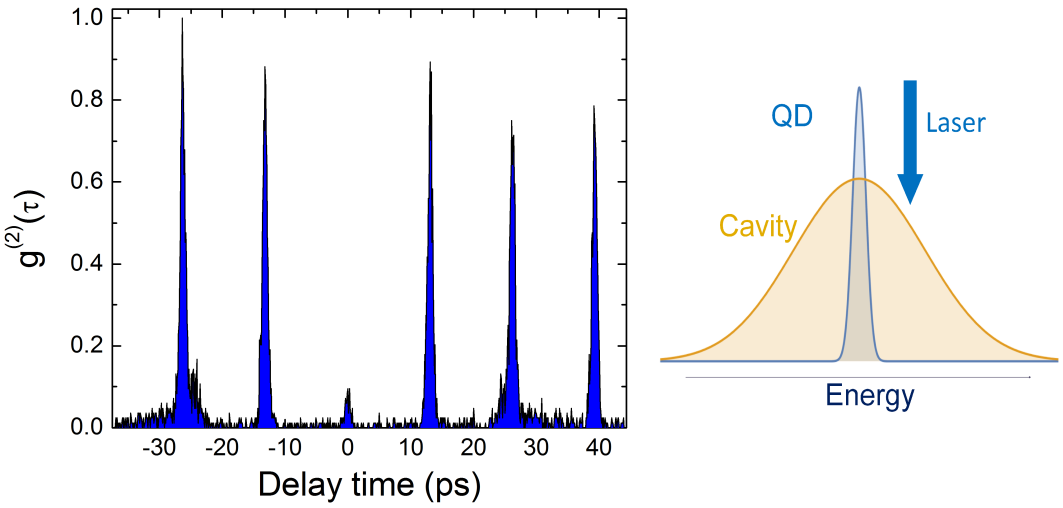

Figure 4.8: $g^{(2)}(\tau)$ measurements for a laser excitation power of 100 nW. The laser is +0.73 meV detuned relative to the QD. $g^{(2)}(0) \approx 0.1$. On the right hand side is the scheme of the QD, cavity and laser energy position. In this case, the laser excites the QD through the phonon side band (laser positive detuned relative the QD).

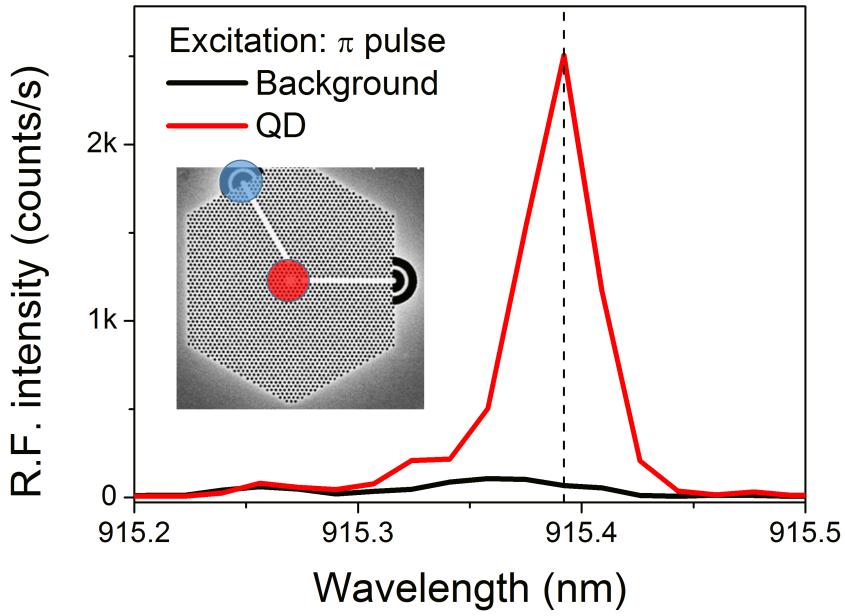

(a)

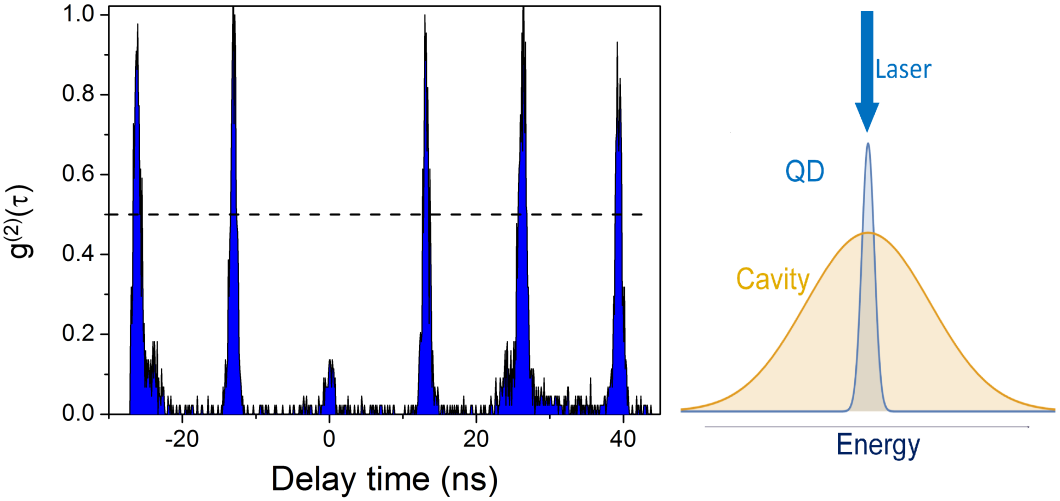

(b)

Figure 4.9: a) Spectra for the QD resonant (red line) and off–resonant (black line) with the laser. The signal to background ratio is (35 : 1). Inset: the configuration of the experiment. The excitation (red circle) hits the cavity whilst the signal is detected from the out–coupler (blue circle). b) $g^{(2)}(\tau)$ measurements for a laser excitation power correspondent to π of pulse area. $g^{(2)}(0) \approx 0.14$. On the right hand side is the scheme of the QD, cavity and laser energy position. In this case, the laser excites resonantly the QD, which is resonant with the cavity.

To further filter the laser scattering, an on–chip configuration was used. Thus, the excitation laser was positioned at the cavity (red circle) whilst the QD signal was collected from the out-coupler (blue circle) as shown in the insert of fig. 4.9(a). The spatial separation between the excitation laser and the detection signal allows obtaining of a high signal to background ratio at high excitation powers. Such an experimental configuration is permitted because the Purcell factor significantly improves the emission quality of the QD. Thus, it is possible to couple a waveguide-coupled low Q–factor cavity (600) with the H1 cavity, keeping a good QD quality. Figure 4.9(a) shows the spectra for the QD resonant (red line) and off-resonant (black line) within the laser duration ($FWHM = 16.8$ ps). The signal to background ratio is $(35 : 1)$. This is the outcoupler coupled with the M1 mode, which is resonant with the QD. An excitation power of 8.3 nW, corresponding a pulse area of π, was used. Owing to the poor spacial match between laser and QD, and the poor coupling between the laser and the cavity, a laser power of 8.3 nW means that only 2.5 photons on average arrive to the QD exciting it. This value was obtained by DFTD simulation performed by Dr. R. Coles and is explained in next subsection (section 4.4.1).

The $g^{(2)}(\tau)$ results are shown in fig. 4.9(b). The $g^{(2)}(0) \approx 0.14$ is slightly worse than the results above, but is still a good single photon source. This value can be limited by the 2 photon emission, which is more likely at high excitation powers (excitation power at π is bigger than at 0.7π). To further investigate the contribution of the 2 photon emission, the probability of creating two excitons within the laser duration was computed. Figure 4.10 shows the probability of create a single exciton (red) and two excitons (purple) as a function of time. The probability of the two excitons was computed by:

$$C_{2\text{ Excitons}} = C_X(\Theta = \pi, t) \times C_X(\Theta = \zeta, t)\,, \tag{4.5}$$

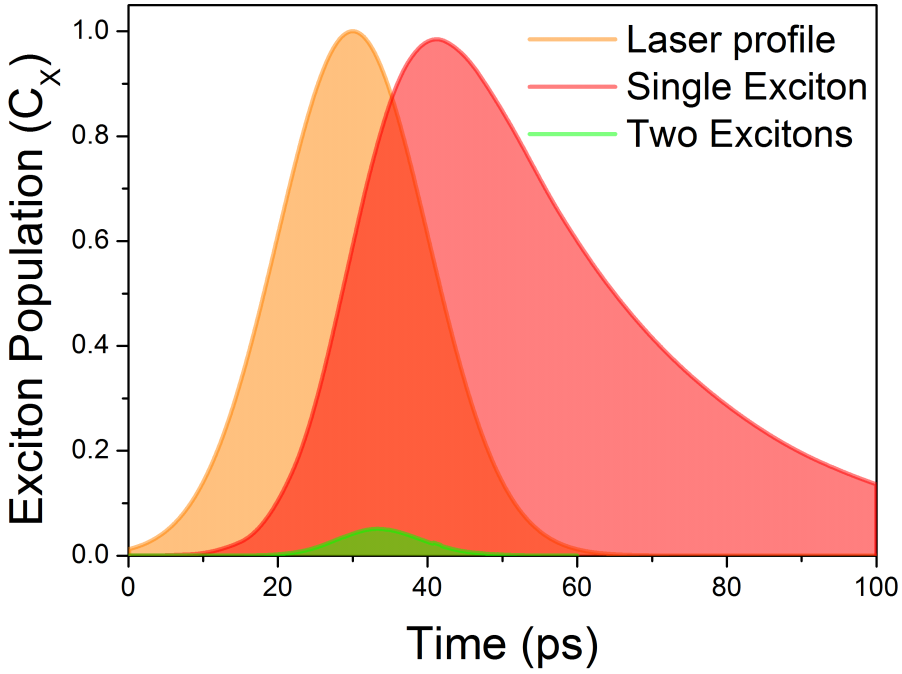

Figure 4.10: The laser profile with a FWHM of 16.8 ps (orange), probability of creating a single exciton (red) and two excitons (purple) within the laser duration. Simulations obtained by solving eq. (A.23) (see appendix A)

where $C_X(\Theta = \pi, t)$ is the probability of creating a single exciton for a π pulse area laser and $C_X(\Theta' = \zeta, t)$ is the probability of creating the other exciton. However the pulse area is now $\Omega_R = \zeta$, which corresponds to remaining laser power and can be calculated by $\zeta = \int_t^{+\infty} \Omega(t')dt'/\pi$, where $\Omega(t) = \pi \exp\left(-t^2/(2\tau_p^2)\right)/(\tau_p\sqrt{2})$ and τ being the pulse half width. From the simulation (shown in fig. 4.10), the probability of creating two excitons is ≈ 0.051. This simulation was obtained solving the master equation presented in appendix A. Therefore, the value of $g^{(2)}(0)$, measured previously, is mainly due to the low signal to background ratio.

Nevertheless, this is a remarkable result, because it shows an on–demand (π pulse area excitation) on–chip (detection from outcoupler) single photon source ($g^{(2)}(0) \approx 0.14 < 0.5$) without any spectral filtering. Moreover this is achieved exciting the QD for 2.5 photons on average. Previous research has demonstrated on demand single photon sources for a QD coupled with a micropillar [70] and

with a planar cavity [104]. This is the first time an on–demand and on–chip single photon source emitting into free space is being reported.

4.4.1 QD Driven by a Few Photons

Owing to the poor spacial match between laser and QD, and the poor coupling between the laser and the cavity, only a small fraction of photons from the laser arrives to the QD and excites it. The average number of photons that reaches the QD was obtained from Lumerical Solutions FDTD simulations. The M1 mode is centered at 915.34 nm with a theoretical Q-factor of $31,000$. However the experimental Q–factor, for the waveguide-coupled cavity, was ≈ 600. The difference between the experimental and the theoretical Q–factor is not known. To match with the experimental Q–factor, all external loss mechanisms from the experimental device were added into the simulation:

$$\frac{1}{Q_{\text{experimental}}} = \frac{1}{Q_{\text{intrinsic}}} + \frac{1}{Q_{\text{loss}}}\,, \tag{4.6}$$

where $\frac{1}{Q_{\text{loss}}}$ is the loss rate introduced into the simulation. The refractive index of the photonic crystal membrane was $\tilde{n} = 3.4 + 0.003i$, where 3.4 is the real refractive index of GaAs at 4 K. The imaginary component corresponds to the value for which the Q–factor simulated match with the experimental. Thus, the coupling efficiency is estimated, by calculating the power absorbed by the cavity as:

$$\eta = \frac{P_{\text{cavity}} - P_{\text{no cavity}}}{P_{\text{source}}\xi_{\text{abs}}}\,, \tag{4.7}$$

where P_{source} is the total power injected by the source, P_{cavity} is the total power leaving the simulation domain with the cavity present and $P_{\text{no cavity}}$ is the power absorbed by the photonic crystal membrane. $P_{\text{cavity}} - P_{\text{no cavity}}$ is the power absorbed by the cavity. ξ_{abs} is a correction factor applied to account for the fields

scattered to free space:

$$\xi_{\text{abs}} = \left(1 - \frac{Q_{\text{loss}}}{Q_{\text{intrinsic}}}\right) = 0.982\,. \tag{4.8}$$

This means that $\approx 98\%$ of the power is dissipated by the cavity and absorbed by the membrane, the other 2% is scattered to free space. To take into account these scattered fields the coupling efficiency is divided by ξ_{abs}. Therefore, the total power dissipated by the cavity is obtained. The laser beam was a Gaussian field source, focussed by the objective lens. A thin lens with 0.55 NA (numeric aperture) and diameter 50.7 mm was used in the model. The lens is illuminated by a beam of width 1.74 mm (calculated from experimental apparatus). The source was positioned $2\,\mu$m above the cavity and is focussed onto the cavity. A transmission box around the whole simulation recorded the total power leaving the simulation domain. A schematic of the simulation is shown in fig. 4.11. The coupling efficiency from these simulations was calculated to be 0.483%. This low value is due to a large laser spot and a small cavity and the laser incidence being

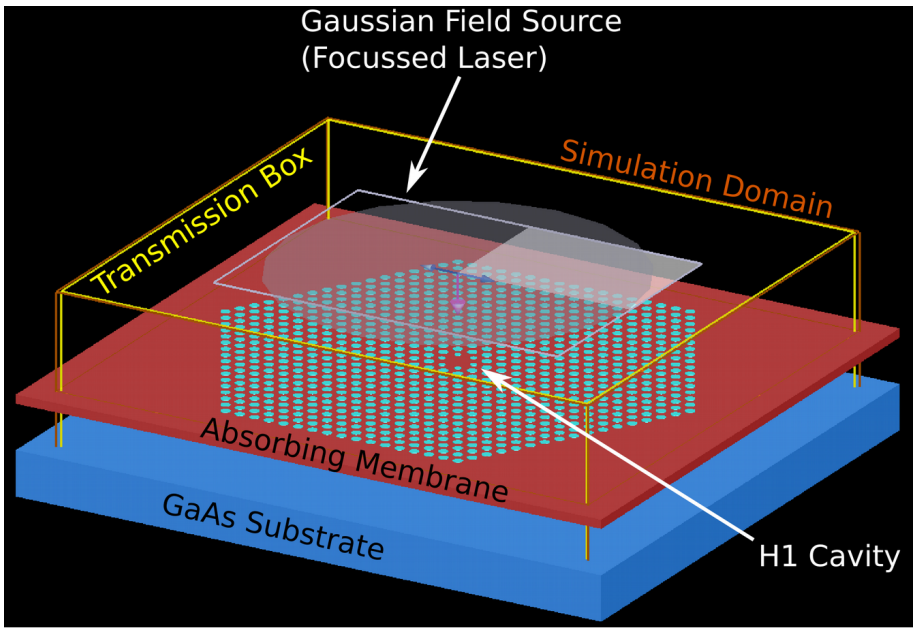

Figure 4.11: Schematic of the FDTD simulation used to estimate the laser coupling efficiency–by Dr Rikki Coles.

orthogonal to the cavity plane. The number of photons in the cavity required for a π pulse area can then be calculated by:

$$N^{\pi}_{\text{cavity}} = \eta \frac{hc\Gamma_{\text{rep}}}{\lambda P^{\pi}_{\text{avg}}}, \tag{4.9}$$

where η is the laser-cavity coupling efficiency defined above, Γ_{rep} is the laser repetition rate, λ is the wavelength, and P^{π}_{avg} is the average π pulsed laser power. For a 76 MHz pulsed laser at the cavity wavelength with 8 nW average power the average number of photons in the cavity is 2.44.

4.4.2 Brightness

Another important parameter to measure the efficiency of the QD as a single photon source is the brightness. The highest number of counts measured from the CCD was $\approx$ 15 kHz when the expected value should be 76 MHz (laser rate). This huge difference between the value measured and the value expected can be understood as result of the losses caused by the optics placed in the path detection (from the outcoupler to the CCD). For a QIP context, more important than the fraction of light which reaches the CCD is the fraction of light which comes out of the QD. This is the light which will flow in the circuit. Thus, brightness is defined as the probability (P) of collecting a single photon in the first external optic at every laser pulse [114]. $P = \eta P_s$, where P_s is the probability that the quantum dot is in a target state at every laser pulse and η is the extraction $\beta(1-\alpha)$, where β is the fraction of the light emitted by the QD that is coupled into the cavity mode; $(1-\alpha)$ is the fraction of the microstructure optical field that can be collected by the first lens in the collection setup.

If a π pulse is used to excite the QD and the QD is a good single photon emitter ($g^{(2)}(0) = 0$), then P_s is almost 1 ($P_s = 1 - g^{(2)}(0)$). In this on-chip single

photon source, $g^{(2)}(0)$ was measured with a π pulse is 0.14. The coupling efficiency for each waveguide is 0.36 and 0.09 respectively (efficiencies obtained from FDTD simulation performed by Dr. R. Coles). Thus, $P = P_s\eta = 1 \times 0.86 \times 0.36 = 31\%$, meaning the probability of collection of a single photon by the waveguide every laser pulse is 31%.

Previous results for micropillars [114, 115] show much higher brightnesses, 70% and 60%, respectively. The reason for such high brightness is that they measured very high single photon purity ($g^2(0) < 0.01$). These values were obtained filtering the QD emission using a Fabry–Pérot interferometer and performed in a micropillar cavity, which has much higher efficiencies. As is shown in supplementary information in [70], $g^2(0)$ before the filtering was ≈ 0.12, similar to the value reported here.

4.5 Resonant Rayleigh Scattering

The very short lifetime measured in section 4.3.2 indicates that, under resonant excitation, high coherence should be possible for the QD. For similar QDs the dephasing time T_2^* is ≈ 600 ps [96]. As T_1 is one order of magnitude lower than T_2^* (22.7 ps), it is expected that T_2 must be limited by T_1. This ($T_2 \approx 2T_1$) is a key condition for obtaining indistinguishable photons. In this section further measurements, carried out by J.O'Hara, A. Brash and C. Phillips, are reported to confirm the high photon coherence.

Photon coherence can be measured by the visibility. The visibility of two-photon interference is given by the $T_2/2T_1$ ratio (see section 2.6.1). High $T_2/2T_1$ ratio means that the photons emitted do not suffer any dephasing (small T_2^*); on the other hand, a low $T_2/2T_1$ ratio means that the photons experience strong dephasing (large T_2^*). As a consequence of strong dephasing the QD has a

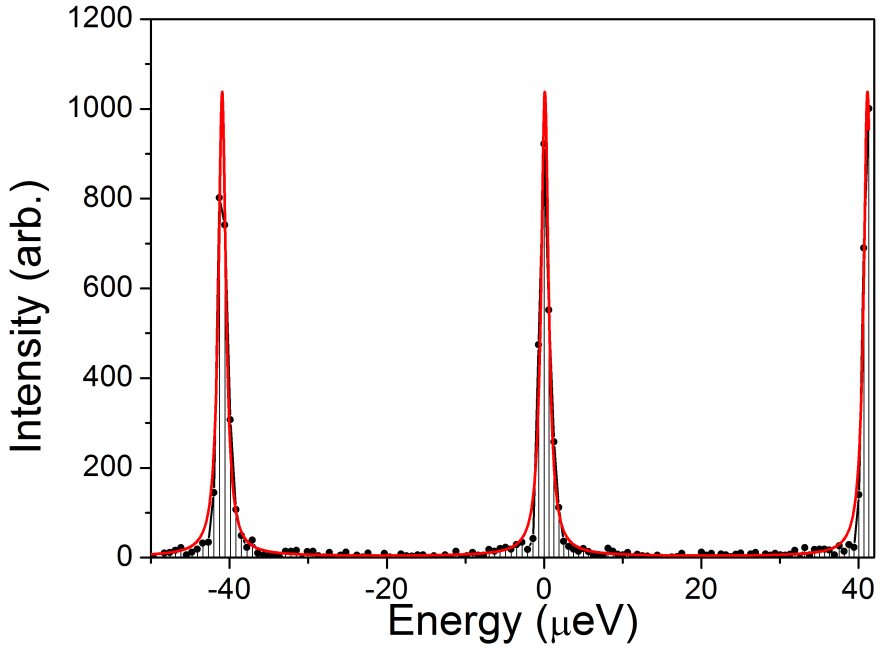

Figure 4.12: Spectrum measured for a laser power of 25 nW using a CW excitation

higher probability of emitting distinguishable photons. So for an indistinguishable photon source $T_2/2T_1$ ratio must be close to 1. To measure T_2, a Fabry-Pérot Interferometer (FPI) was used. From the FPI spectra, the $T_2/2T_1$ ratio was calculated.

Figure 4.12 shows a spectrum measured by FPI. The spectrum was measured at low power excitation (25 nW). The red line is the multi Lorentzian fit. From the fit the intensity of the coherent Rayleigh scattering (I_{RSS}) and the incoherent (I_{RF}) light is obtained. The I_{RSS} and I_{RF} correspond respectively to the peak area and background area (in this case the background is ≈ 0). Figure 4.13 shows the ratio of $I_{RSS}/(I_{RSS}+I_{RF})$ plotted as a function of the excitation power. The red line is the fitting obtained from the following expression [116–118]:

$$\frac{I_{RRS}}{I_{Total}} = \frac{T_2}{2T_1}\frac{1}{1+\Omega^2 T_1 T_2}\,. \tag{4.10}$$

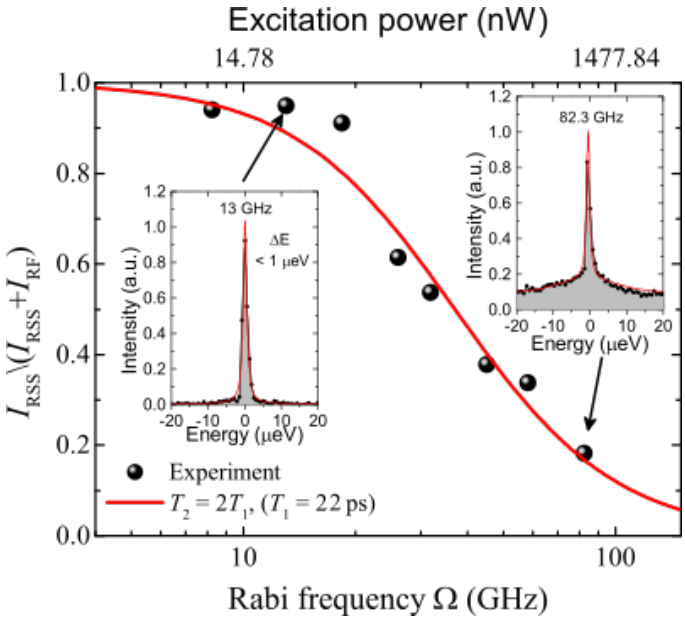

(a)

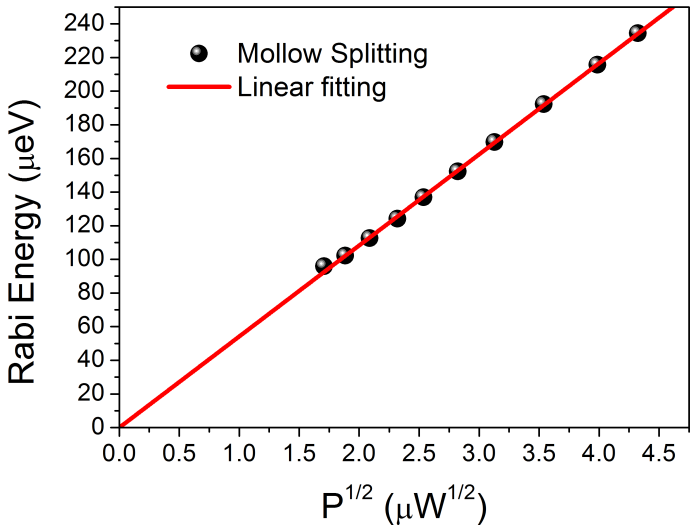

(b)

Figure 4.13: a) Plot of the ratio of the coherently resonantly scattered laser photons (I_{RSS}) over the total QD emission ($I_{\mathrm{RSS}} + I_{\mathrm{RF}}$) as a function of Rabi frequency and CW excitation power. Red line: Simulation using the T_1 measured in fig. 4.5 and taking $T_2 = 2T_1, (T_1 = 22.7$ ps). Insert: High resolution spectra of the QD emission under weak (left) and strong (right) continuous resonant driving measured with a Fabry-Pérot interferometer. The spectrum under weak driving is dominated by coherently resonantly scattered laser photons. Under strong driving, an increased contribution from QD resonance fluorescence is shown by the prominent broad feature. Red line: A double Lorentzian fit. These measurements were performed by J. O'Hara and A. Brash.

To fit the data presented in fig. 4.13(a), it was assumed that $T_2 \approx 2T_1$. The reason for this assumption is that I_{RSS}/I_{Total} at low power is ≈ 1. Ω was obtained from the Mollow triplet measurement (see fig. 4.13(b)). The fit agrees well with the experimental data. And T_1 matches with the value obtained previously in section 4.3.2 At low power $T_2/2T_1 \approx 1$ (94.9%), meaning that the QD emits near transform-limited photons [119]. As expected, increasing the laser power the $I_{RSS}/(I_{RSS}+I_{RF})$ tends to 0. This happens owing to the spectral broadening ($\propto \Omega^2$) [120, 121]. The coherence time is then limited by the exciton lifetime. This is one of the requirements for an ideal single photon source.

4.5.1 Indistinguishability

As seen in the previous section, the QD under study emits near transform-limited photons ($\approx 95\%$). Thus, the two photons emitted in a short interval of time must be indistinguishable; this means they must have the same quantum state and energy. Due to the charge noise, which causes small energy shifts in the QD, the photons emitted in a long interval of time are less indistinguishable [119,122]. To demonstrate that two photons emitted in a short time are highly indistinguishable, Hong–Ou–Mandel [110] measurements were made by exciting the QD with two resonant π pulses and detecting the waveguide-coupled on-chip QD emission scattered from the outcoupler.

For the HOM measurement a fibre interferometer is used in the Mach Zehnder configuration as illustrated in Fig. 4.14(a). Fibre paddles are used to correct for birefringence induced by the fibres, ensuring polarization matching at the second fibre splitter where photon coalescence occurs. A short delay fibre is added to one arm to introduce a delay of 2 ns with respect to the other. The delay time is chosen to be significantly larger than both the emitter lifetime and detector response time, ensuring well-resolved peaks. A motorized half-wave plate

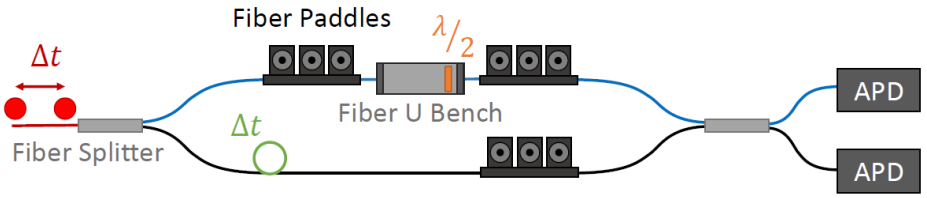

(a)

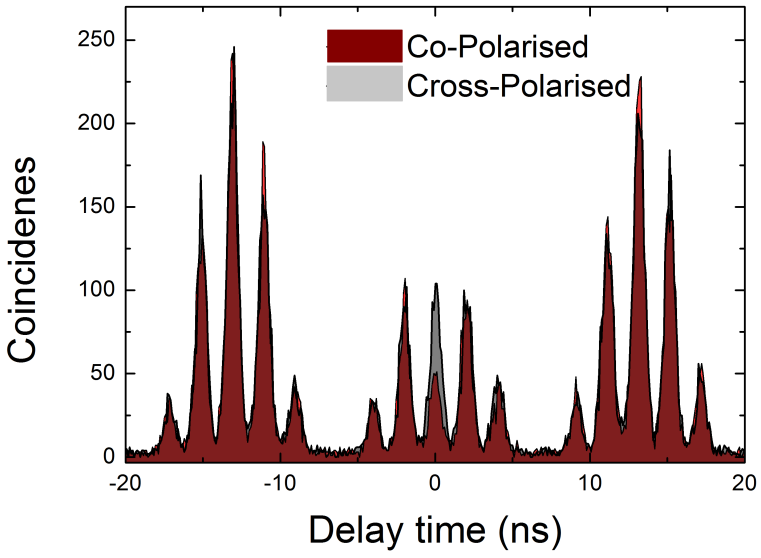

(b)

Figure 4.14: a) Scheme of the Michelson-type interferometer to perform the HOM measurement. The two photon counters are connected to a coincidence counter. b) The coincidence histogram as a function of the delay time between the two photon created by two pulse with pulse area of π and separated temporally by 2 ns. This measurement was performed by A. Brash and C. Phillips.

(HWP) allows the polarization of the other arm to be rotated between co- and cross-polarized with respect to the other, making the photons either maximally or minimally distinguishable. The photon has a 50% chance of going through either the short or long arm. When the time delay between the two photons emitted is smaller than T_1, the photons can interfere with each other before being detected.

The indistinguishable photons interfere in such a way that should negate any coincidence (HOM effect). Figure 4.14(b) shows the number of times a photon is detected at both APD (coincidences) with polarisation control in each arm.

The grey and red histograms are the coincidences for cross– and co–polarisation, respectively. The peaks at ±4 ns result when the first photon goes through the short arm and the second photon goes through the long arm. The peaks at ±2 ns result when both photons go through the same arm (the pulses are separated by 2 ns). The central peak at 0 results when the photons go through different arms, with the first through the long arm and the second through the short arm. Thus both photons meet at the beam splitter, interfering with each other. When the two photons are indistinguishable (i.e. co-polarisation case), the peak at $\Delta = 0$ ideally vanishes [102, 123]. The relative difference between the peak amplitude in each of the co– and cross–polarised cases, tells how indistinguishable the photons are. In this case an indistinguishability of $74.7 \pm 2.7\%$ was measured (value after correction for the non-unity purity of the emission and the interferometer properties–see supplementary information in [70]). The loss of indistinguishability is only related to the electron-phonon coupling without being affected by spectral diffusion [124].

4.6 Conclusions

In this chapter a QD coupled with a cavity, in the weak coupling regime, was explored as a photon emitter. Because of the cavity, the optical emission of the QD is enhanced, making it a good candidate for a single–photon source. The strong Purcell effect (34–see fig. 4.6) is the key point of this near-ideal single–photon source. The Purcell effect reduces the exciton lifetime in such way that $T_2 \approx 2T_1$ (see section 4.5). This high coherence is a requirement of an ideal single photon source. Such a short lifetime could only be measured because of the TPRF technique. This technique allows measurement of very fast radiative lifetimes which could not be measured by conventional detectors. The exciton lifetime reported here (22.7 ps–see fig. 4.5) is shorter than any previous measurement in

the weak coupling regime [69, 70, 76, 125].

Combining resonant excitation, strong Purcell effect and electrical tuning, an efficient on-chip electrical tunable single photon source has been demonstrated. To confirm this, autocorrelation and HOM measurement were carried out, by exciting the QD with a resonant π pulses and detecting the waveguide-coupled on-chip QD emission from the outcoupler. A single photon purity of 84% (see fig. 4.9) and indistinguishability of 95% (see section 4.5.1) were obtained, by exciting the QD with a few photons (2.5 photons on average).

The device reported here emits coherent single photons many orders of magnitude faster and consumes much less excitation power and space on the chip than previous devices [91]. Moreover, the short exciton lifetime (22.7 ps) and high coherence implies potential single-photon emission rates > 10 GHz. These features make this device a good candidate to form the building block for quantum computing chips based on multiple on-demand single-photon sources.

Chapter 5

Influence of Cavity on QD Exciton–Phonon Coupling

5.1 Introduction

The exciton population of a QD by longitudinal acoustic (LA) phonon assisted processes has been proposed in [126, 127] and shown in [128–130]. The inversion population by incoherent excitation is possible due to the interaction of the dressed states with the Boson bath [131]. The population inversion via phonon assisted excitation is much more robust to the variations in the pump strength and laser detuning. This advantage can be explored in different applications.

In these previous works, the exciton population achieved was limited by the power available. Here the effects of cavity on QD–exciton coupling are explored on the process of enhancement of the spontaneous [69,70] and LA phonon assisted emission [132]. This is called Purcell effect [73] and has widely studied in QD coupled with microcavities. The cavity enhancement can also significantly reduce the power needed to achieve population inversion by phonon assisted excitation, as shown theoretically in [133].

The study presented in this chapter follows the previous research developed in the author's group. Either the excitation [128] and de-excitation [61, 134] of an exciton by the phonon assisted process were demonstrated in a bare QD. In this previous research the exciton population was detected by the photocurrent technique. The novelty of the work reported here is that the QD is coupled with a cavity and the RF signal is detected, instead of the photocurrent. As the QD is coupled with a cavity, an electric field enhancement of ≈ 4.5 was observed. This means that considerably fewer photons are needed to populate the QD (2.5) than in a bare QD. Thus, two main results were obtained: *i*) observation of slow damping in Rabi oscillations, indicating that cavity reduces the exciton-phonon interaction. This mechanism is not fully understood yet, and *ii*) the eletric field enhancement also allows to see the full picture of the exciton–phonon interaction. These results are discussed in detail in this chapter.

5.1.1 Theory

The model that describes the interaction of a two–level system coupled with a phonon bath and to an optical cavity is [135, 136]:

$$H = \Delta\sigma_+\sigma_- + \frac{\Omega_c(t)}{2}\left(a^\dagger + a\right) + \sum_{\mathbf{q}} \omega_{\mathbf{q}} b^\dagger_{\mathbf{q}} b_{\mathbf{q}} + \hbar f\left(\sigma_- a^\dagger + \sigma_+ a\right) + \sigma_+\sigma_- \sum_q \left(g_{\mathbf{q}} b^\dagger_{\mathbf{q}} + g^*_{\mathbf{q}} b_{\mathbf{q}}\right) , \quad (5.1)$$

where Δ is the laser detuning relative to the QD, $g_{\mathbf{q}}$ defines the exciton–phonon and f is the QD–cavity coupling, $a^\dagger$ (a) is the photon creation (annihilation) operator and $\sigma_+ = |0\rangle\langle X|$ ($\sigma_- = |X\rangle\langle 0|$) is the exciton creation (annihilation) operator. The exciton is driven by an optical pulse $\Omega(t) = \Theta \exp\left(-t^2/(2\tau_p^2)\right)/(\tau_p\sqrt{2})$, where τ_p is pulse half width and Θ is the pulse area. $\Omega(t)$ is also equal to $2\mu\epsilon(t)/\hbar$, where μ is the exciton dipole and the $\epsilon(t)$ is the electric field. The phonon bath

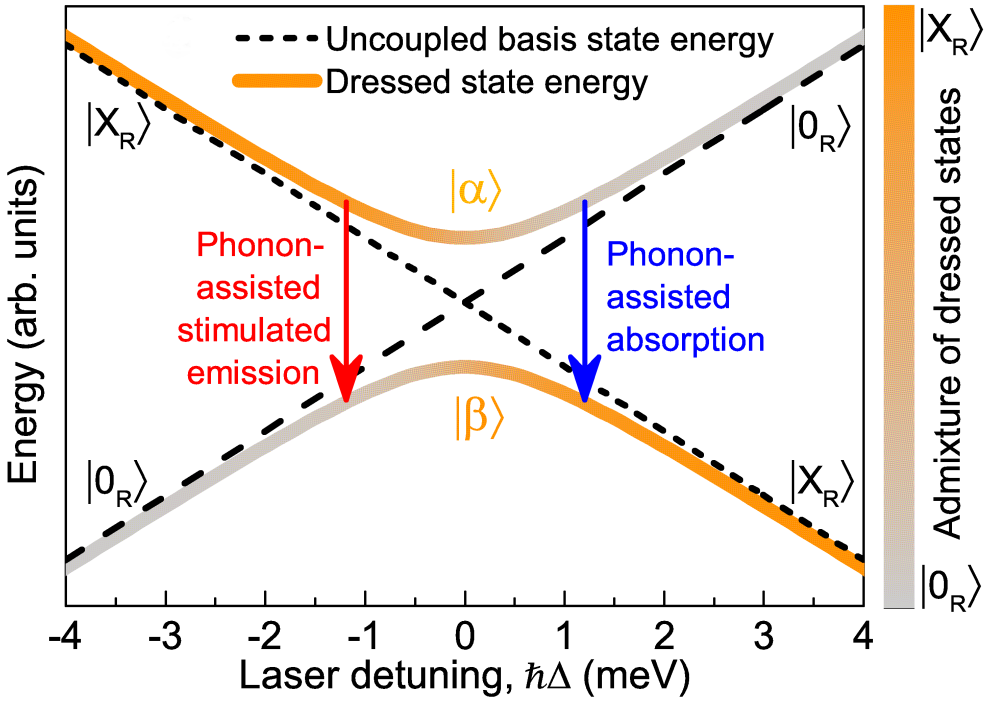

Figure 5.1: The dressed-state picture. $|0_R\rangle$, $|X_R\rangle$: uncoupled ground state and exciton state viewed in the rotating frame. $|\alpha\rangle$, $|\beta\rangle$: optically dressed states split by the effective Rabi energy Λ.

consists of harmonic oscillators with wave vector $\mathbf{q}$; $b_{\mathbf{q}}^{\dagger}$ ($b_{\mathbf{q}}$) is the creation (annihilation) operator and $\omega_{\mathbf{q}} = v_s|\mathbf{q}|$ is the frequency of the acoustic phonon, where v_s is the speed of sound. Only the acoustic phonons are considered, since the measurements were performed in a near resonant excitation, and the optical phonon energies are typically > 30 meV [56, 57]. $g_{\mathbf{q}}$ is the coupling strength of the exciton–phonon bath interaction. Equation (5.1) was obtained assuming the rotating wave approximation. More detail can be found in appendix A

Figure 5.1 shows how the laser couples the exciton state with the phonon bath. As a result of the coupling between the phonon and the QD, the dressed states are formed ($|\alpha\rangle$ and $|\beta\rangle$) and separated by the effective Rabi splitting ($\Lambda = \sqrt{\Omega^2 + \Delta^2}$). The relaxation between the dressed states implies the emission or absorption of a phonon with an energy equal to the effective Rabi splitting. This relaxation process is an extra channel of dephasing and is a function of the

Rabi frequency [48].

Beside the exciton–phonon interaction there is still the QD–cavity coupling. A few papers show the solution of eq. (5.1) for CW excitation [137, 138]. The difficulty of this problem increases for pulsed excitation. However, the Hamiltonian eq. (5.1) is simplified, assuming the system is in the "bad cavity" limit. This means the QD is weakly coupled with the cavity. This is a reasonable good assumption once the cavity, under study here, has a very low Q–factor.

In the weak coupling regime an optical cavity traps the light in a very small region. Thus, the electric field at the centre of the optical cavity is concentrated. A QD placed at the centre of the cavity experiences the enhancement of the electric field. The coupling strength between a QD and an optical cavity is given by:

$$g = \frac{1}{\hbar}\sqrt{\frac{\hbar\omega}{2V_m}}\mu\,, \tag{5.2}$$

where μ is the QD dipole moment and V_m the cavity volume (see section 2.7.1).

The resonant drive strength of a QD weakly coupled with an optical cavity is [127, 133]:

$$\Omega_{\text{eff}}(t) = \frac{g\Omega_c(t)}{\sqrt{\kappa^2 + \Delta_{LC}^2}} \tag{5.3}$$

$$\Theta_{eff} = \frac{g\Theta_c}{\sqrt{\kappa^2 + \Delta_{LC}^2}}\,, \tag{5.4}$$

where $\Theta = \int_{-\infty}^{+\infty} dt\Omega(t)$, Θ_c is the pulse area (drive strength) and the Rabi frequency of the pulse is described by $\Omega_c(t) = \Theta_c/(2\tau\sqrt{\pi})\exp[-(t/2\tau)^2]$. The cavity decay rate is $\kappa = \omega_c/Q$ and Δ_{LC} is the detuning between the laser and the cavity resonance. The drive strength will be much higher for a QD coupled with cavity than a bare QD, for the same power. When the laser is resonant with the cavity ($\Delta = 0$) the pulse area must increase by a factor of Q ($\Theta_c = Q\Theta$). This means less power will be needed to obtain the same pulse areas. As the pulse area is

$\Theta \propto \sqrt{P}$ (P is the laser power), the power experienced by the QD is

$$P_{QD} \propto \frac{g^2 Q^2}{\kappa^2 + \Delta_{Lc}^2} P_c \,, \tag{5.5}$$

where P_c is the power injected in to the cavity. Knowing this, the Hamiltonian eq. (5.1) can be reduced to:

$$H = \Delta\sigma_+\sigma_- + \frac{\Omega_{\text{eff}}(t)}{2}\sigma_x + \sum_{\mathbf{q}} \omega_{\mathbf{q}} b_{\mathbf{q}}^\dagger b_{\mathbf{q}} + \sigma_+\sigma_- \sum_q \left(g_{\mathbf{q}} b_{\mathbf{q}}^\dagger + g_{\mathbf{q}}^* b_{\mathbf{q}}\right) \,, \tag{5.6}$$

where $\Omega_{\text{eff}}(t)$ is given by eq. (5.4) and $\sigma_x = (\sigma_+ + \sigma_-)/2$.

In appendix A the eq. (5.6) is solved using the master equation approach. Throughout this chapter, wherever possible the experimental data will be supported by simulations obtained from the master equation.

5.1.2 Experimental Details

To measure the influence of the cavity and phonon bath on the QD, the differential resonance florescence (DRF) technique was used. The full details of this technique is explained in section 3.5.3. This is a spectrally resolved technique, and so allows not only the measurement of the neutral exciton, but also other species at the same time. To show a spectrum measured by DRF, the excitation laser is -1 meV detuned relative to the neutral exciton (X^0), which is resonant with the cavity at 0.83 V. Figure 5.2 a) shows the relative energy position of the laser, cavity, QD and a different QD, namely QDb. Figure 5.2 b) shows the raw spectra measured at 0.83 V (black line) and 0.81 V (red line). By subtracting the spectrum measured at low bias from the spectrum measured at high bias, the differential spectrum is obtained (blue line). The laser is not completely suppressed, but nevertheless the suppression is enough to see clearly the neutral exciton (X), bi–exciton (XX), with binding energy of -3.4 meV, and the other quantum dot, which is named

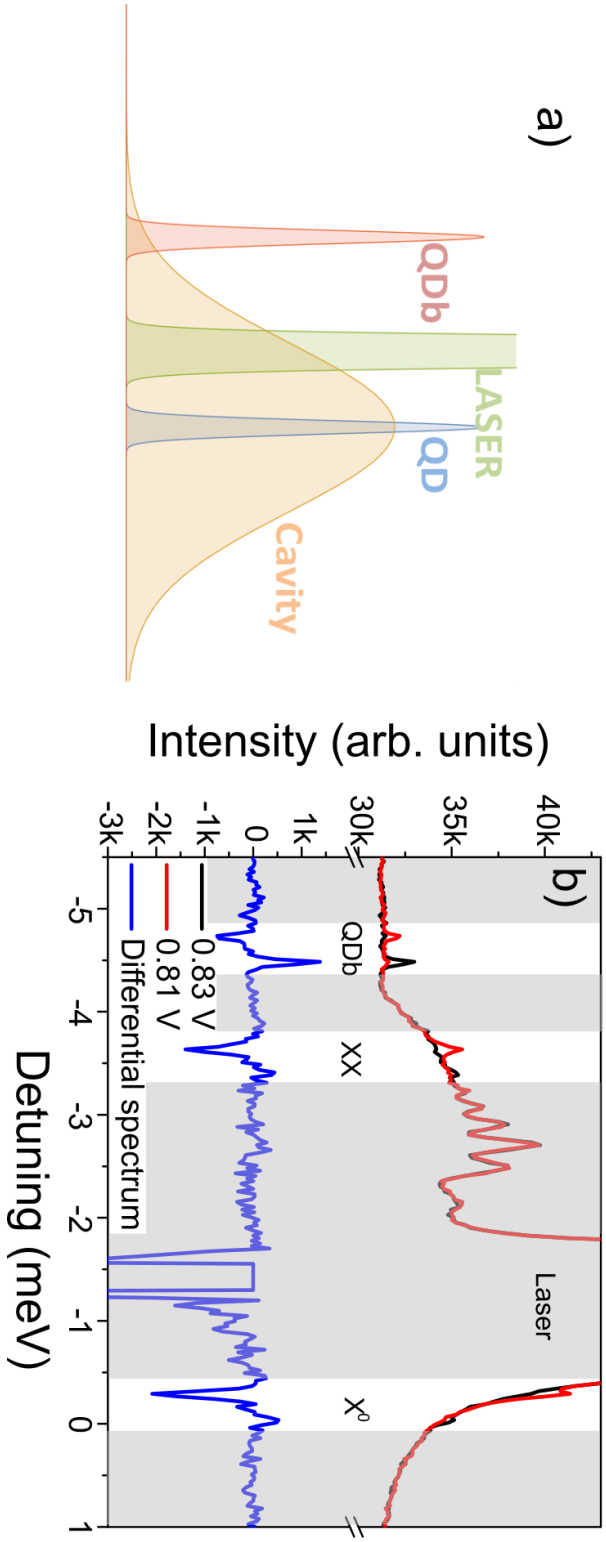

Figure 5.2: a) Experimental configuration of a DRF measurement. b) Raw spectrum at 0.83 V (black) and 0.81 V (red). Subtracting each other the differential spectrum (blue) is obtained. The neutral exciton (X^0), the bi–exciton (XX) and QDb are observable. The experimental configuration used is shown in a).

QDb. The dispersive shape is then a consequence of the DRF technique.

This technique allows measurements of the QD resonant with the laser, which are presented in next section section 5.2 and measurements of the exciton–phonon coupling enhancement section 5.3.

5.2 Cavity–Enhanced Rabi Oscillation

5.2.1 Rabi Oscillation of the QD in the Cavity vs QD in the Bulk

As seen in section 5.1.1, the cavity modulates the electric field experienced by the QD, enhancing the electric field when the QD is resonant with the cavity and reducing the field when the QD is far away from the cavity. This means that the cavity renormalizes the pulse area axis. The cavity enhancement is easily seen by comparing the P^{π} for a QD resonant with a cavity and an uncoupled QD (see fig. 5.3). A P^{π} enhancement of 22 is observed. The cavity enhancement is further discussed in the following sections. This drive strength enhancement allows exploration of phenomena at high pulse area, previously inaccessible due to the high power requirements. However, the laser suppression is a limitation at resonance. As at high laser powers the laser suppression is not efficient (see section 3.5.2), the QD RF signal can not be separated from the laser scattering.

5.2.2 QD–Cavity Detuning Dependence of the Rabi Oscillation

To understand how the cavity affects the electric field, the RF power dependence of the QD was measured for different laser–cavity detunings. The QD is de-

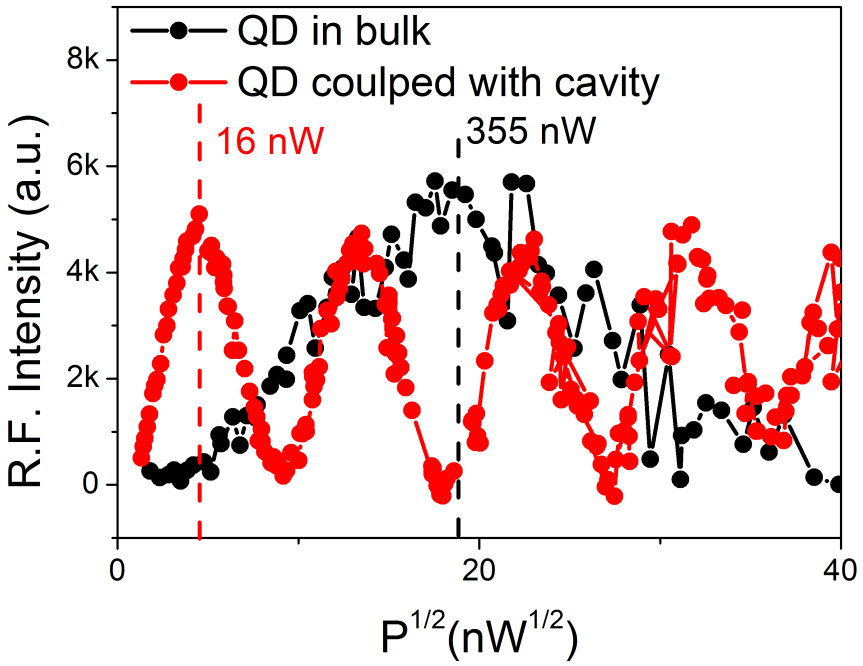

Figure 5.3: Rabi oscillations of a QD coupled and resonant with a cavity (red dots) and of a QD in bulk (black dots)

tuned relative to the cavity by changing the bias (AC-Stark effect), and the laser frequency was changed so that it was always resonant with the QD. Figure 5.4 shows the power dependence for two different detunings. The well known Rabi oscillations are observed. At $\Delta = 0$ meV detuning the electric field is more enhanced than at $\Delta = -2.47$ meV as expected (see eq. (5.4)). On the right hand side of Equation (5.4) the experimental configuration for two different laser/QD detuning relative to the cavity: $\Delta = 0$ (top), and $\Delta \neq 0$ (bottom). Less power is needed at $\Delta = 0$ meV to achieve the full inversion population (π pulse area) than at $\Delta = -2.47$ meV.

From these Rabi oscillations measurements, P_c^π, which corresponds to the π power enhanced by the cavity, was obtained. Figure 5.5 shows the normalized $1/P_c^\pi$ as function of laser–cavity detuning (blue dots). The cavity modes are shown in the background and the QD is coupled to the grey shaded mode. The dashed blue line is the fit function obtained from eq. (5.5), assuming P_{QD}^π is

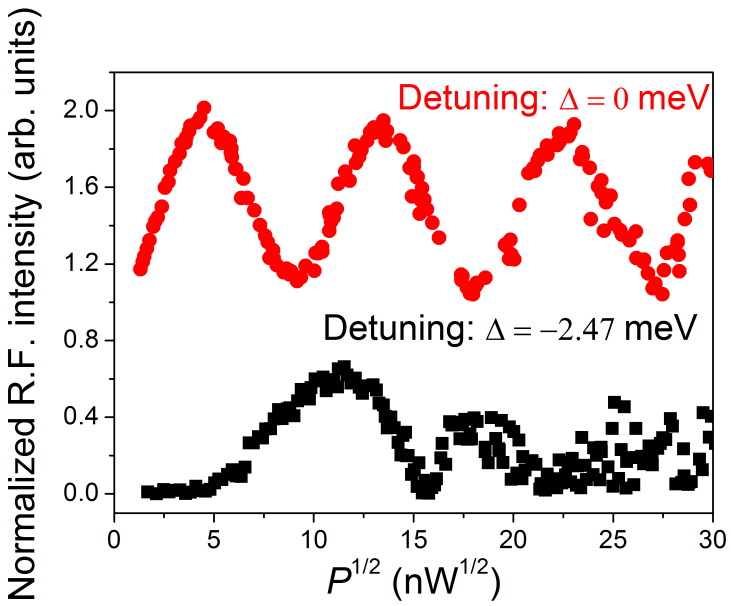

Figure 5.4: Power dependence measurements for two different QD/laser detuning relative to the cavity: $\Delta = 0$ meV (resonant with cavity, same data as fig. 5.3) and -2.47 meV. Note that the laser is always resonant with the QD.

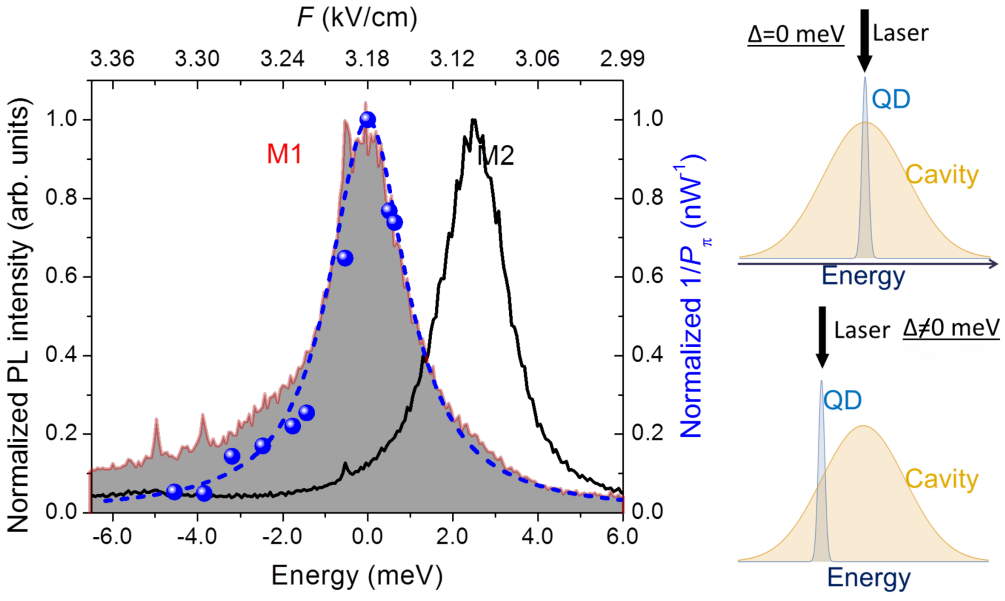

Figure 5.5: Inverse of π pulse power as function of QD detuning relative to the M1 mode (blue dots and right hand Y axis). The dashed blue line is obtained fitting eq. (5.5) and using the measured cavity line–width. In the background are the normalized cavity modes (left hand Y axis). The QD is coupled with the grey shaded mode M1. On the right hand side are the experimental configurations of two different detunings: $\Delta = 0$ (top), and $\Delta \neq 0$ meV (bottom).

constant. This assumption is true because change of the oscillator strength in this voltage range (see top axis) can be neglected. Note that the only fitting parameter used was the amplitude. Q, k were experimentally obtained. The data and the fit function (eq. (5.5)) follow the cavity mode M1. For negative detuning ($\Delta < -2$ meV), it seems that they start to diverge. This happens because at that energy there is some background, which is not visible at positive detunings. The P_c^π for $\Delta = 0$ meV is ≈ 20 larger than for $\Delta = -4.5$ meV, which corresponds to an electric field enhancement of ≈ 4.5. This enhancement is analogous to the Purcell effect observed in the spontaneous emission rate in chapter 4.

5.2.3 π Rotation Driven by a Few Photons

The previous subsections showed that the cavity indeed enhances the electric field experienced by the QD when it is resonant with the cavity, resulting in a reduced power necessary to populate the QD. The lowest π power measured was 8.9 nW as shown in fig. 5.6(a). This enhancement allows the measurement of Rabi oscillations up to $22\,\pi$ of pulse area (see fig. 5.6(b)). At higher pulse area the laser noise does not permit measurement of the RF of the QD. The laser power of 8.9 corresponds to 2.5 photons (see section 4.4.1).

The coherent manipulation of a QD with few photons has been shown in a QD–micropillar cavity system [125]. The micropillar had high in–coupling efficiency (95 %) and high Q–factor $(11,000)$. Thus, only 3.8 photons were needed to populate the QD. In the case reported in this chapter, even with much lower Q–factor (539), the average number of photons needed to fully populate the QD is lower (2.5). The reason for that is the mode volume. Whilst in a micropillar cavity the mode volume is quite large, H1 photonic cavities are very small. The mode volume affects the Purcell factor. The Purcell factor is 13 in [125] whilst in this case is ≈ 42 (see chapter 4).

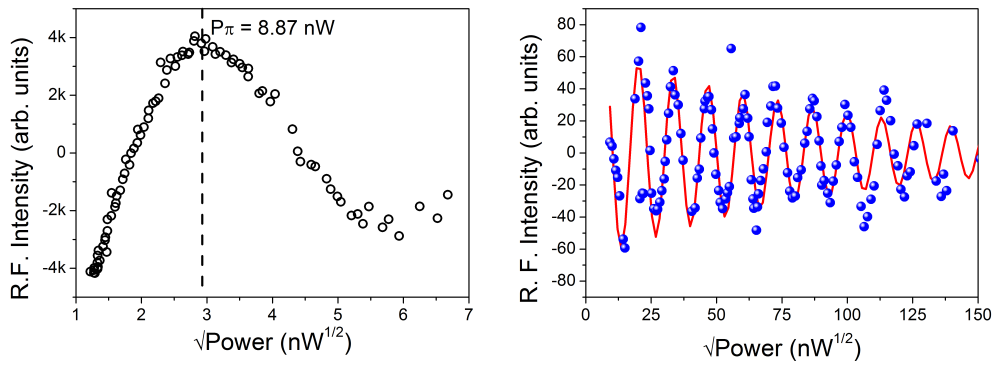

(a) (b)

Figure 5.6: a) The lowest π power measured. b) Rabi oscillation up to 22 π pulse area. The red line is only to guide the reader.

5.2.4 Reduced Damping of the Rabi Oscillation

Longitudinal acoustic phonons are the main source of Rabi rotation intensity dumping in InAs/GaAs self-assembled quantum dots. This has been extensively studied both experimentally [47, 139, 140] and theoretically [141, 142]. The dephasing depends on the coupling strength of the exciton to the phonon bath. This process occurs when a phonon is resonant with the effective Rabi frequency, allowing a pathway for the exchange of energy between the QD and the crystal lattice. Consequently the exciton loses its phase [143] causing a mixing of exciton states (see section 2.6.1 and appendix A.3).

The exciton–phonon interaction is caused by the deformation potential and the strength of exciton–phonon depends on the pulse area. Thus, the damping of Rabi oscillations depends on the pulse area of the laser. In [144] pure dephasing and phonon scattering on a single QD coupled to a cavity is studied in a weak regime. However this study is for off-resonant cavity mode emission, saying nothing about the resonant case. Figure 5.7 compares the damping of the Rabi oscillations for a bare QD (black dots) and a QD coupled with a cavity (red dots). The Rabi oscillations for a bare QD (black dots) were measured by the photocur-

rent technique and were reported in [145]. The damping is much stronger for the bare QD than for the QD coupled with the cavity. The black (red) line is the simulation assuming (very weak) exciton–phonon interaction. The simulations confirm that the phonon bath is indeed the main source of dephasing (black line) and that the exciton–phonon interaction is much weaker when the QD is coupled with a cavity (red line). This surprising new effect is not totally understood yet. Below the discussion of some possible contributing factors are presented.

The total time of the phonon–induced scattering between dressed states is determined by the laser pulse duration. Once the laser pulse is off, there will be no dressed states (see fig. 5.1). The laser linewidth is the same for both measurements: QD coupled with a cavity, and a bare QD. Thus, a similar dephasing rate should be expected.

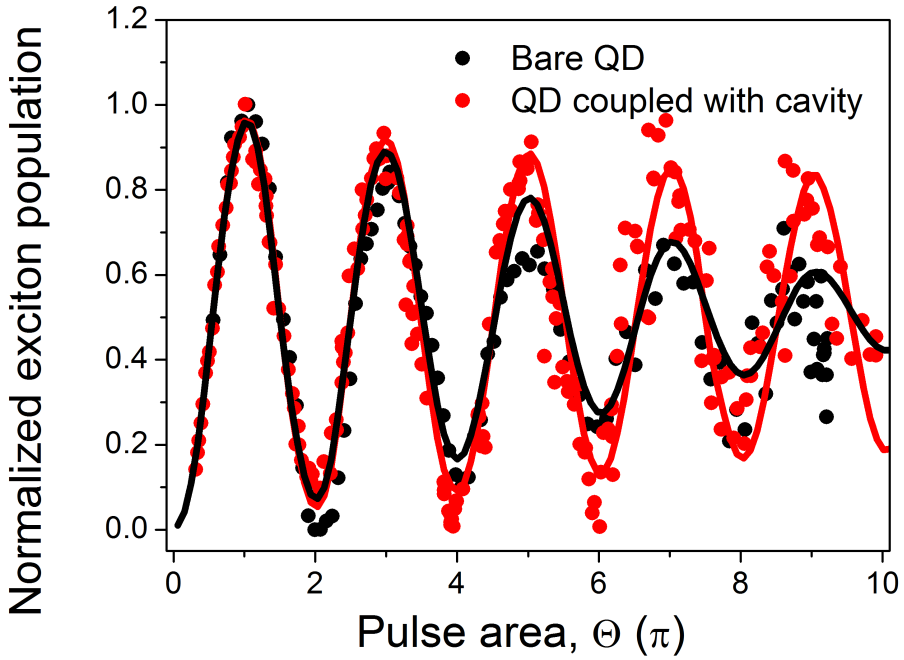

Figure 5.7: Power dependence measurement when laser is resonant with the QD for a bare QD (black dots) and a QD coupled and resonant with a cavity (red dots). The black and red lines are the results from simulation with strong and very weak exciton–phonon interaction, respectively.

For low driving regime, the typical dephasing time in a InGaAs bare QD is a few tens of picoseconds [146] or even hundreds [147, 148]. However, in this case, the spontaneous emission is so fast ($\approx$ 22 ps) due to the Purcell effect (see section 4.3), the phonons have a negligible effect, as is shown in fig. 5.7.

That means somehow the cavity affects the exciton–phonon coupling, reducing this interaction when the QD is resonant with cavity. Figure 5.8 shows the power dependence measurements for the QD resonant and detuned 0.5 meV relative to the cavity. The damping rate is larger when the QD is detuned relative to the cavity. This evidence that the cavity indeed affects the coupling exciton–phonon, reducing the damping rate of the Rabi oscillations. In other words the cavity enhancement overcomes the phonon dephasing. Such an effect was also observed in [149]. This shows that this artificial atom performs as if fully isolated from the solid-state environment.

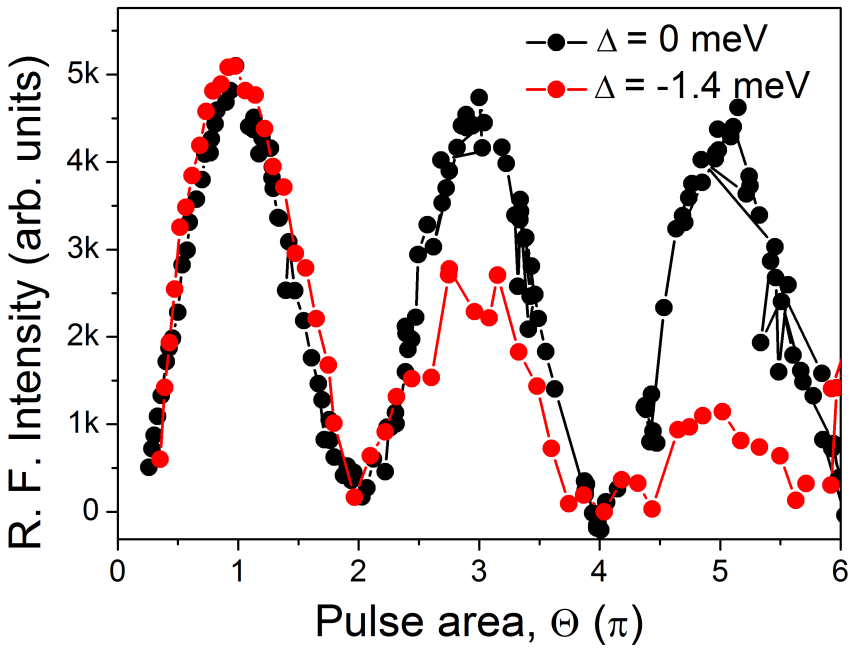

Figure 5.8: Rabi oscillations with QD resonant (black dots) and -1.4 meV detuned (red dots) relative to the cavity.

To observe more pronounced phonon effects in the intensity damping of the Rabi oscillations, the QD should be detuned well away from the cavity. Small detuning shows small effects, since the cavity is very broad (poor Q–factor). However, as the exciton detuning relative to the cavity is controlled by the DC–Stark effect, this affects the oscillator strength and also the slope of the potential barriers affecting tunnelling rates. Both effects alter the intensity of RF. Therefore, when the exciton is detuned away ($\Delta > -4.5$ meV) relative to the cavity, the RF intensity drops so much as to be impossible to measure. Hence it was not possible obtained data at large detunings

5.2.5 Mollow Triplet Evidence

Another piece of evidence of the influence of the cavity on exciton–phonon interactions is observed in the Mollow triplet spectrum. Figure 5.9(a) shows the

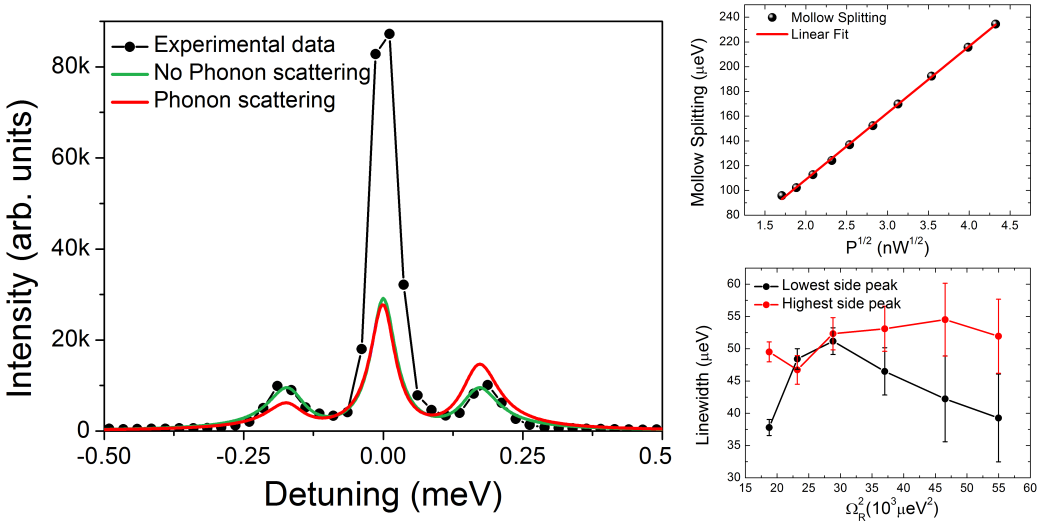

(a) (b)

Figure 5.9: a)Mollow triplet spectrum measured with 600 nW CW laser excitation and the linewidth of central peak as function of the laser excitation. The red and blue line are the simulation with and without phonon scattering. b) The Rabi splitting as a function of the laser power (top and fig. 4.13(b)) and the side peak line–width as a function of the square of the Rabi frequency (bottom).

Mollow triplet spectrum measured using CW excitation. The QD is the same as below and is resonant with the cavity. The side peaks in the experimental data agree well with the simulation when there is no phonon scattering (blue line). The central peak is much larger than the side peaks in the experimental data because the CW laser at that power was not completely suppressed. The central peak should be only twice as large as the side peaks. The red line takes into account the phonon bath. The Mollow spectrum is significantly modified when the exciton is coupled with the phonon bath. The asymmetry of the red line is owing to some phonon feeding effect. This was also reported in [137, 150, 151]. Calculation details can be found in appendix A.2.

Figure 5.9(b) shows the Rabi splitting as a function of the CW laser power (top) and the side peak line–widths as a function of the square of the Rabi frequency (bottom). The line–width of the side peaks should reflect the phonon induced pure dephasing [152]. This effect is linearly proportional to the square of the Rabi frequency. Thus, a linear dependence of the side peak line–width on the square of the Rabi frequency would be expected [120, 153]. However, in this case there is no trend of the side peaks line–width (see bottom fig. 5.9(b)). This reinforces the idea that the cavity reduces strongly the exciton–phonon interaction.

The mechanism behind this result is not entirely understood. A more accurate model should be developed to take into account the cavity–phonon interaction and further measurement should be done to understand how the cavity affects the exciton-phonon interaction. Nevertheless, this is a remarkable result. Long coherence times are a requirement of any QIP. Knowing that and how a cavity can extend the coherence times will permit devices more suitable to build quantum gates and consequently a quantum chip.

5.3 Exciton–Phonon Coupling Enhancement

Section 5.2.4 has identified the reduced damping of the Rabi oscillations when the QD is coupled to the cavity. This effect is not full understood yet. However as has been shown in chapter 4, one possible explanation may be due to the enhancement of the spontaneous emission. The cavity enhances the QD spontaneous emission in such a way as to overcome the exciton–phonon interaction. In this section the enhancement of the exciton–phonon coupling will be discussed. To observe the full exciton–phonon bath interaction, the exciton amplitude, which is related to the exciton population, was measured for different powers and detunings of the laser. Figure 5.10 a) shows the experimental configuration. The QD was resonant with the cavity and the power and detuning of the laser were scanned. The creation of an exciton via phonon assisted excitation is schematically shown in Figure 5.10 b). A blue shifted laser excites the QD. By phonon assisted relaxation an exciton is created. Then the exciton recombines radiatively, emitting a photon which is detected by the RF technique. The probability of emitting a phonon, and consequently creating an exciton, depends on, among other factors, the spectral density function shown in fig. 5.10 c). The assisted phonon processes have already been discussed in section 2.6.4.

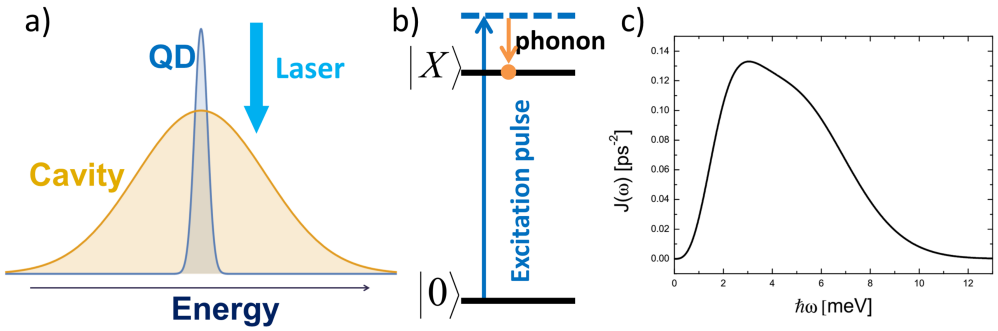

Figure 5.10: a) Experimental configuration to measure the phonon side band of the QD resonant with the cavity. b) Energy level diagram of the phonon emission. c) Spectral density function.

When the laser drives the exciton resonantly the Rabi oscillations are observed. At positive detuning the exciton is populated via phonon assisted emission. Due to the Purcell enhancement of the drive strength (see section 5.2), inversion population is achieved at much lower power compared with a bare QD. Previous work, in a bare QD, only reached 9π [59]. Therefore, in a QD coupled with a cavity, the full phonon side band is visible. This is the first time this has been reported. However the results presented in fig. 5.11 raise a few questions.

5.3.1 Vanishing of Phonon Side Band at High Pulse Areas

The phonon side band vanishes for high laser powers (high pulse areas) as is shown in fig. 5.11. To show clearly this vanishing, the exciton population is plotted as a function of laser power with the laser resonant (black line) and +0.5

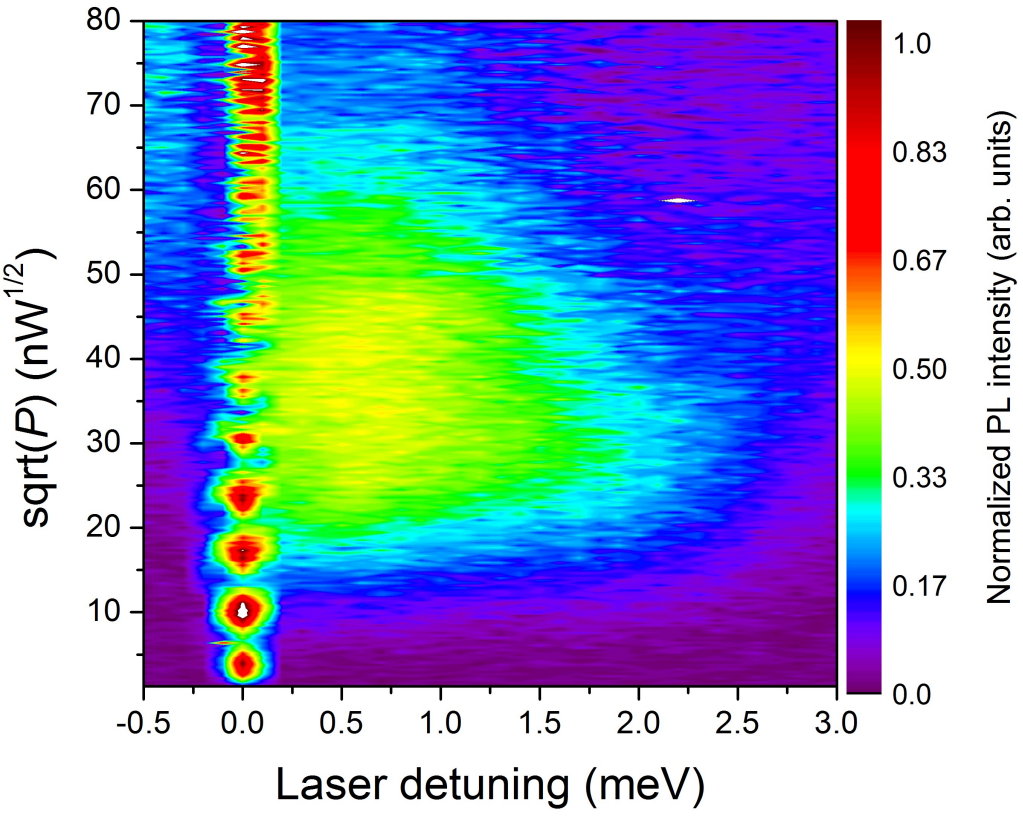

Figure 5.11: Normalized exciton population as function of power and laser detuning. The laser line–width is 16.5 ps. The QD is resonant with the cavity.

meV detuned relative to the QD (red line)(see fig. 5.12(a)). At resonance the Rabi oscillations are visible up to a pulse area of $13\,\pi$. The intensity at 3π is bigger than at π. This can be due to the re–excitation of the QD, since the exciton lifetime (22 ps) is comparable with the pulse duration (9 ps). However such a feature is not always observed. At higher pulse areas, for the resonant case, the oscillations are no longer visible due to the poor laser suppression. At quasi resonant excitation ($\Delta = +0.5$ meV), the exciton population increases till 0.7, reaching the maximum at $9\,\pi$ of pulse area and then decreases.

Taking another look at the spectrum density function (see fig. 5.10), it is clear that after the cut off energy (≈ 3 meV) the coupling between the exciton and the phonon decreases. This means that at the strong driving regime, the exciton is not coupled any more with the phonon bath. This non-monotonic power dependence of the exciton–phonon coupling explains the expected reappearance of Rabi oscillation predicted in [154]. In that paper square pulses are used. For Gaussian pulses the features discussed in that paper are less pronounced. Moreover, they only study the resonant case, not when the exciton is populated through the phonon side band. This argument is also used in [155]. The excitons were created by adiabatic rapid passage (ARP), using a chirped pulse laser [156]. For negative chirp, the signal rose, reaching $\approx 75\%$ of saturation and then decayed, followed by a rise at much higher excitation powers. This reappearance of ARP is analogous to the predicted reappearance of Rabi rotations at high pulse areas.

For the strong driving regime the exciton population must tend to 0.5, according with the theory [133]. The bottom graph of fig. 5.12(b) shows the exciton population obtained from simulation of eq. (A.23) for $\Delta = +0.83$ meV (see appendix A). For quasi resonant laser detuning and at strong driving regime the exciton population tends to the perfect mixed state ($C_X = 0.5$).

The reason why at strong pulse areas the exciton tends to a pure mixed

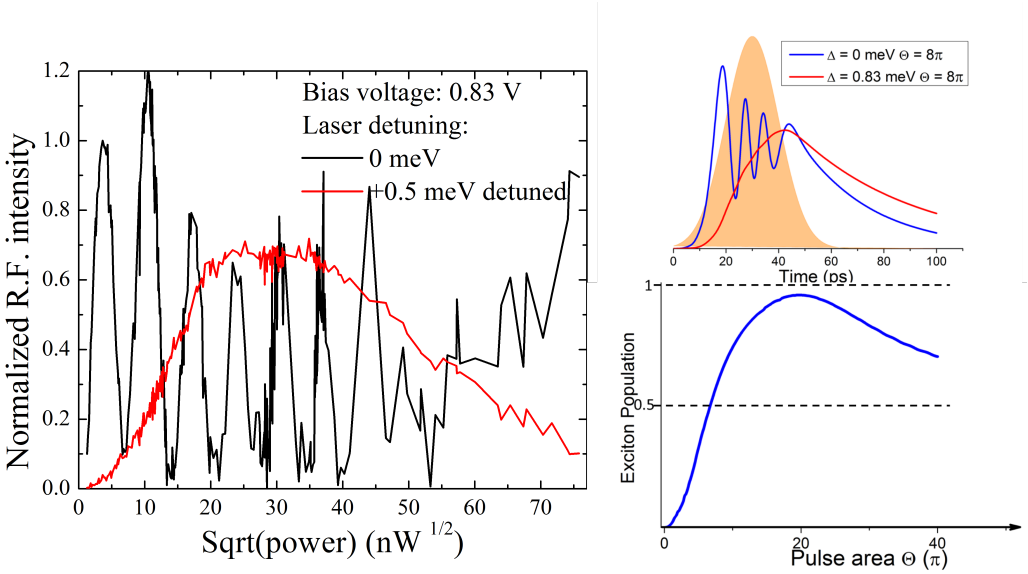

(a) (b)

Figure 5.12: (a) RF Power dependence for QD coupled with cavity. Black line, the laser is resonant with the QD and red line the laser is 0.83 meV detuned. (b) top: shaded orange is the Gaussian laser profile, the blue line and red line are the exciton population as function of time when the laser is resonant with QD and with 8π pulse area and the laser is 0.83 meV detuned and with 8π pulse area, respectively. bottom: illustration of the exciton population as function of the pulse area with QD resonant with cavity and the laser 0.83 meV detuned

state is shown in the top graph of fig. 5.12(b). The graph shows the pulse laser profile and the exciton population for $\Delta = +0.83$ meV, $\Omega = 8\,\pi$ (red line) and $\Delta = 0$ meV, $\Omega = 8\pi$ (blue line) as a function of time. Since the excitation is by a pulsed laser (FWHM of 16.8 ps), the Rabi frequency is not constant. Thus, at the start of the pulse, the exciton experiences weak driving when the coupling to the exciton–phonon bath is strong. The pulse laser scans the spectral density function. Thus, if the laser is powerful enough to reach the cut off energy, the probability to create a exciton via phonon assisted excitation is maximum. Once the exciton is created, if there is still remaining laser, this cannot de-populated the QD because is an off resonant excitation. However, the phonon channel is open while the laser is on, and allows phase exchange between the exciton and the phonon bath, leading the exciton to the pure mixed state. Moreover, because of the Purcell enhancement, and because the laser line–width is comparable with

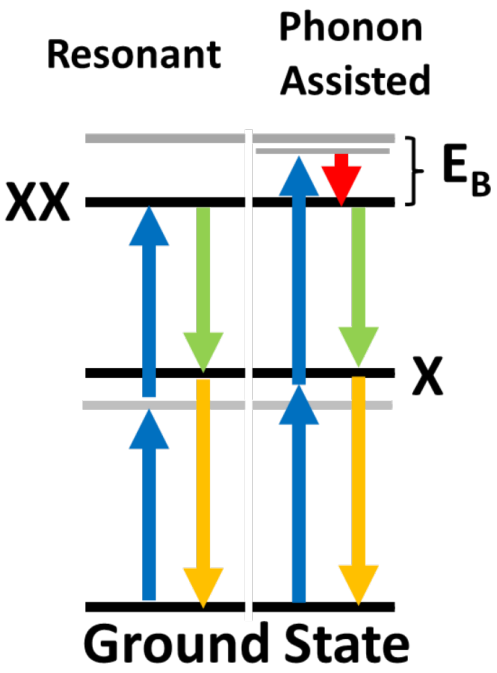

Figure 5.13: Bi–exciton energy level diagram. The blue arrows correspond to two photon transition excitation. The green and orange arrow correspond to bi–exciton and exciton emission, respectively. For the phonon assisted process, a phonon is emitted (red arrow) in order to conserve the energy.

radiative lifetime, the exciton population does not reach population 1

To try to understand the reason for the vanishing of the phonon side band, the bi–exciton was measured. Figure 5.13 shows schematically the bi–exciton energy level diagram. The bi–exciton (XX) is excited by two photons red shifted relative to the exciton (X) energy (blue arrows). This shifting corresponds to half of the bi–exciton binding energy, in the resonant case. Once the bi–exciton is created, it decays emitting two photons: one with energy equal to the exciton energy minus binding energy (green arrow); and another with same energy as the exciton. Thus, the bi-exciton population can be measured either from the bi–exciton peak (fig. 5.14) or from the exciton peak (fig. 5.15). Therefore, the exciton can be populated even at negative laser detuning, through two–photon emission or through bi–exciton phonon side band (see fig. 5.2). Both graphs, fig. 5.14 and fig. 5.15 show the Rabi oscillations when the laser is resonant with the two–photon

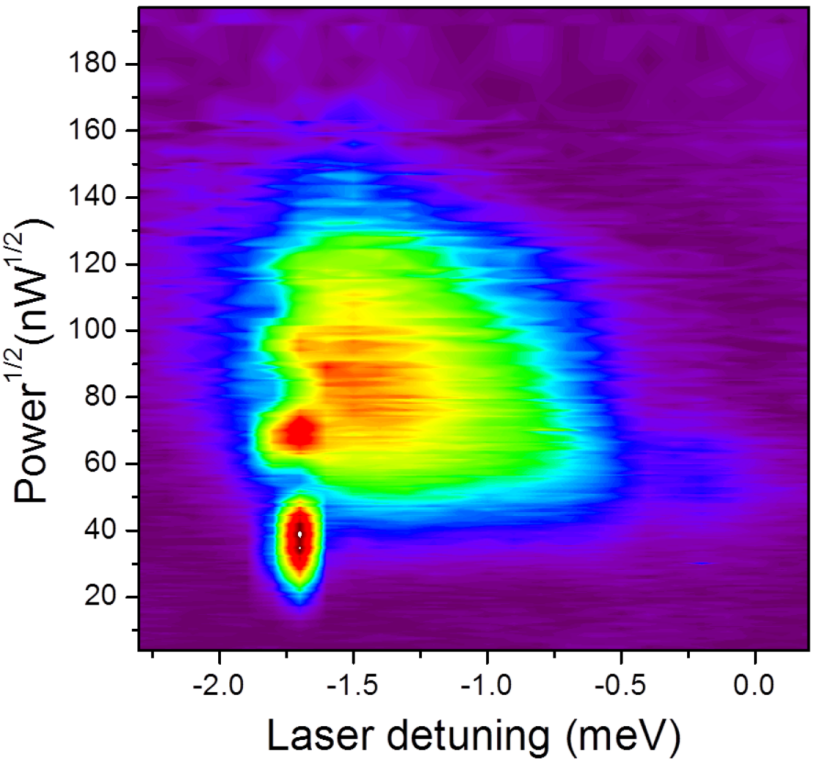

Figure 5.14: a) Normalized biexciton emission as a function of the power and detuning of the laser relative to the cavity.

transition, which occurs at -1.7 meV relative to the neutral exciton. At higher laser detunings than -1.7 meV the phonon side band of two–photon transition is observed. The phonon side band vanishes at high powers as well as the exciton phonon side band. However, as for bi–exciton measurements the laser and the RF signal are spectrally separated, the vanishing of the Rabi oscillation at high pulse area is visible in this case. This is further discussed below.

Figure 5.16 shows the bi–exciton population as a function of the laser power for 0 (black circles) and +0.4 meV (red circles) laser detuned relative to the bi–exciton two–photon energy. So like the side band of the exciton, shown in fig. 5.12(a), the side band of the bi–exciton also vanishes for strong pulse areas. Surprisingly, the same happens for the Rabi oscillations of the bi–exciton, instead of tending to 0.5 as expected (red line). A possible explanation for this

is the following: at high laser powers the exciton/bi–exciton energy system is no longer valid. This means that the laser couples with the exciton in such a way that there is formation of Rabi-split dressed states involving more than one photon [157,158]. This explains also why the theory fails at high pulse area. The current theory does not take into account such coupling between the laser and the exciton states.

For pulsed laser excitation the Mollow triplet is not visible due to the poor laser suppression at high laser powers. However with CW excitation the Mollow triplet is observable as shown in fig. 5.9.

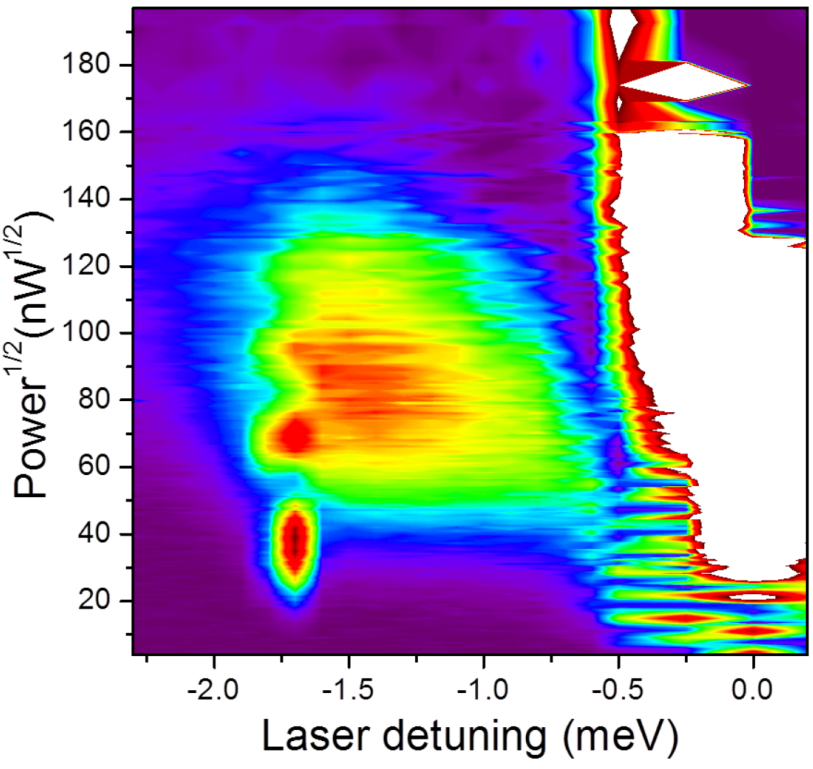

Figure 5.15: a) Normalized exciton emission as a function of the power and detuning of the laser relative to the cavity.

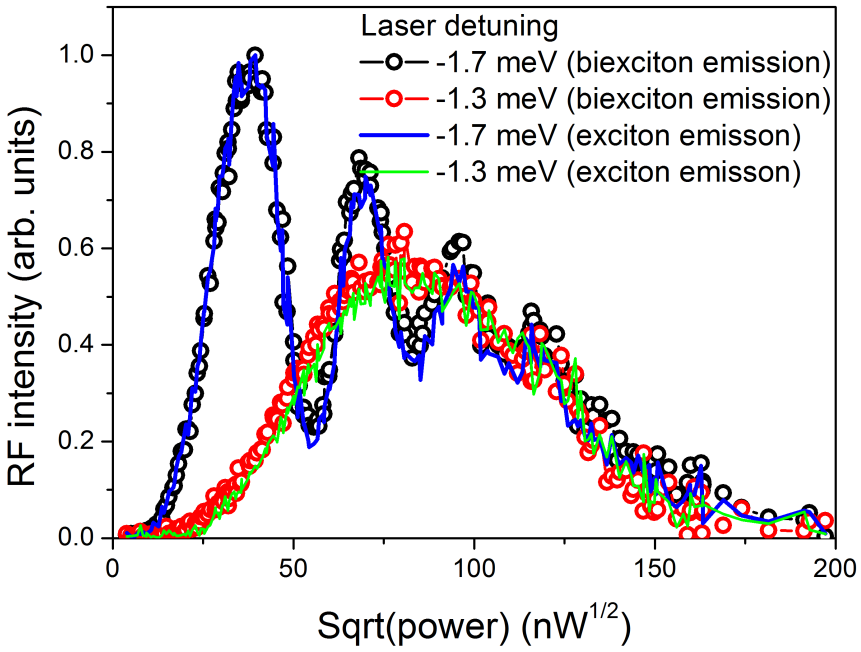

Figure 5.16: RF power dependence of bi–exciton (circles) and exciton emission (lines) in the case of: i) for laser resonant with two photon transition (black circles and blue line) and ii) laser 0.4 meV detuned relative to the two photon transition (red circles and green line). The QD is resonant with the cavity and the detuning values given in legend are relative to the cavity.

5.3.2 Low Inversion Population via Phonon Assisted Excitation

Another unexpected result is the low inversion population obtained via phonon assisted process. The original proposal of the exciton population via phonon assisted emission predicted maximum inversion close to 1 [126]. Figures 5.12(a) and 5.16 show the exciton population as a function of the laser power for resonant and quasi resonant excitation for exciton and bi–exciton, respectively. In both cases the maximum of inversion population by the phonon assisted process is always below 0.7. The same fact is visible in fig. 5.17 where the exciton population is plotted as a function of the laser detuning for a pulse area of 9π.

As mentioned above, the cavity enhances the electric field, thus much less

power is needed to reach π pulse area. This enhancement renormalizes the power axis. This means, the inversion population as a function of pulse area should be similar to the bare QD. To verify this, the inversion population measured in a single bare QD (Quilter *et al* [59]) is compared with the simulation and measurement in a single QD coupled with a photonic cavity (see fig. 5.18). The black dots are the data reported in [59] and the blue line is the simulation for a bare QD. The orange dots are the exciton population for the QD in this study, coupled with a cavity. The red line is the simulation taking into account the cavity enhancement. The data in both cases agree very well with the simulations. The exciton–phonon coupling parameter was the fitting parameter. To obtained so good agreement between the data and the simulation, the exciton–phonon coupling parameter was a 0.43 of the value used in the bare QD case (see fig. A.2). The simulations were obtained solving eq. (A.23) in appendix A.

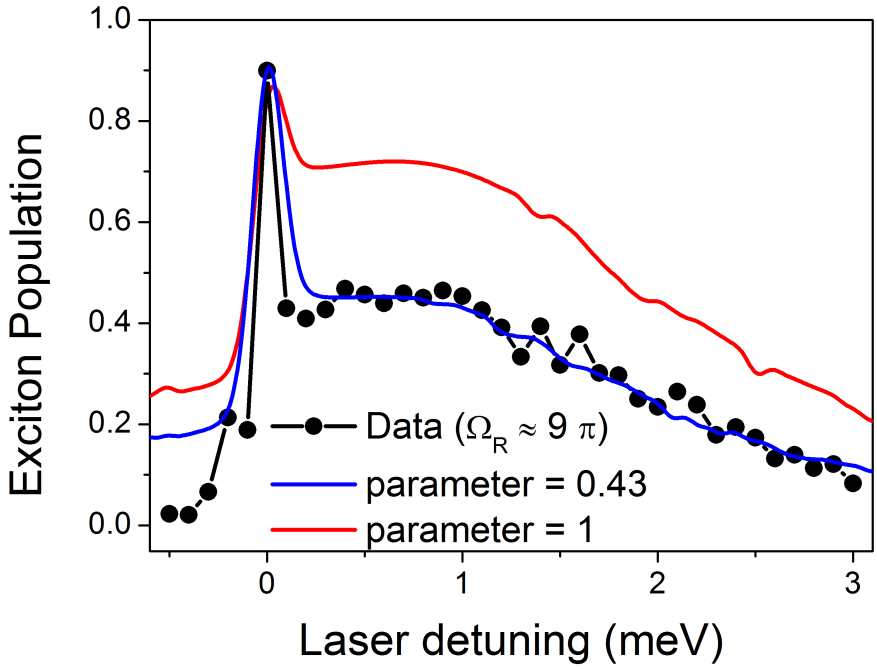

Figure 5.17: Exciton population measured as function of laser detuning for pulse area of $\approx 9\pi$ (black dots). The red and blue line are the the simulations for exciton–phonon parameter 1 and 0.43 respectively. These simulations were obtained from master equation (appendix A).

In section 5.1.1 the cavity enhancement of the Rabi oscillation was demonstrated. As explained above, this happens because of the enhancement of the optical field eq. (5.3). This enhancement depends on laser cavity detuning (Δ_{LC}). As consequence of renormalising the pulse area axis at $\Delta_{LC} = 0$, the results of both the QD coupled with cavity, and the bare QD, would match. Thus, the exciton population difference between the bare QD and the QD coupled with a cavity is a result of the weaker phonon-QD coupling experienced by the QD coupled with a cavity than by a bare QD.

Simulations indicate that the maximum inversion population reached by phonon assisted process must occur around 20π pulse area [133]. Such pulse areas are not achievable in a bare QD system as huge laser power is required. For a QD coupled with cavity the laser power constraints should not be an issue.

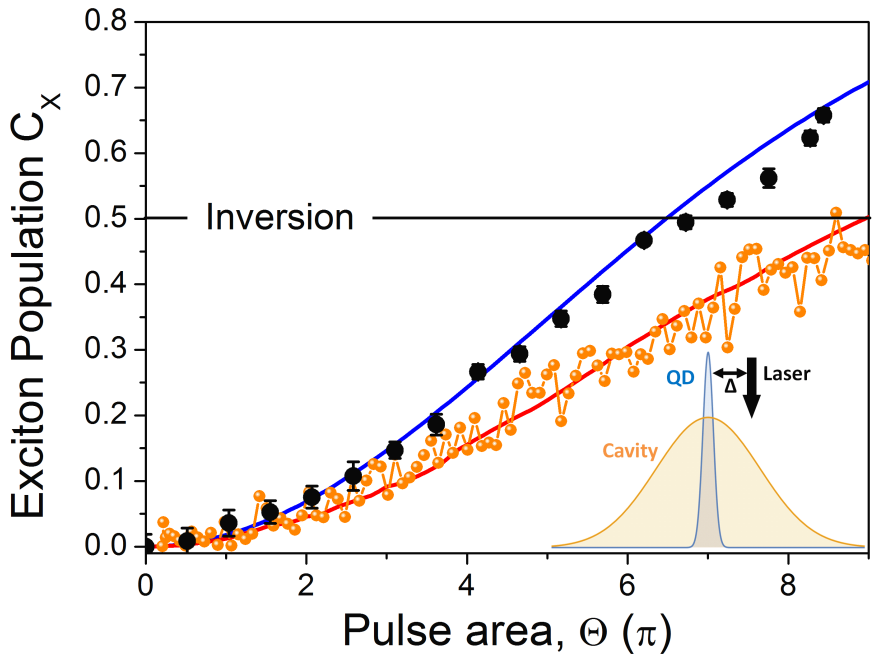

Figure 5.18: Exciton population as function of pulse area measured in a bare QD (black squares [59]) and in a QD coupled with a cavity (orange dots) by the pump pulse $\Delta = +0.83$ meV with. The blue and red lines are the simulation from the master equation for the bare QD and the QD coupled with cavity respectively. Inset: Scheme of the relative position of the cavity, the QD and the laser.

However as explained in section 5.3.1 the two–level system approximation of a QD, described by eq. (5.1) is no longer valid at high laser powers. Thus, for the pulse area range available (before the vanishing of the phonon side band), it is not possible for higher exciton populations to be reached.

Higher inversion populations can be achieved by moving the exciton out of resonance with the cavity and keeping the laser resonant with the cavity. In this way, the maximum enhancement of the optical field is reached, and a higher exciton population is expected the radiative lifetime increases and higher exciton population is expected. Figure 5.19 shows the power dependence measurement of the exciton population when the laser is resonant with cavity and the QD tuned to -0.65 meV relative to the cavity as shown the in inset figure of fig. 5.19. The normalization of the exciton population was obtained from the Rabi oscil-

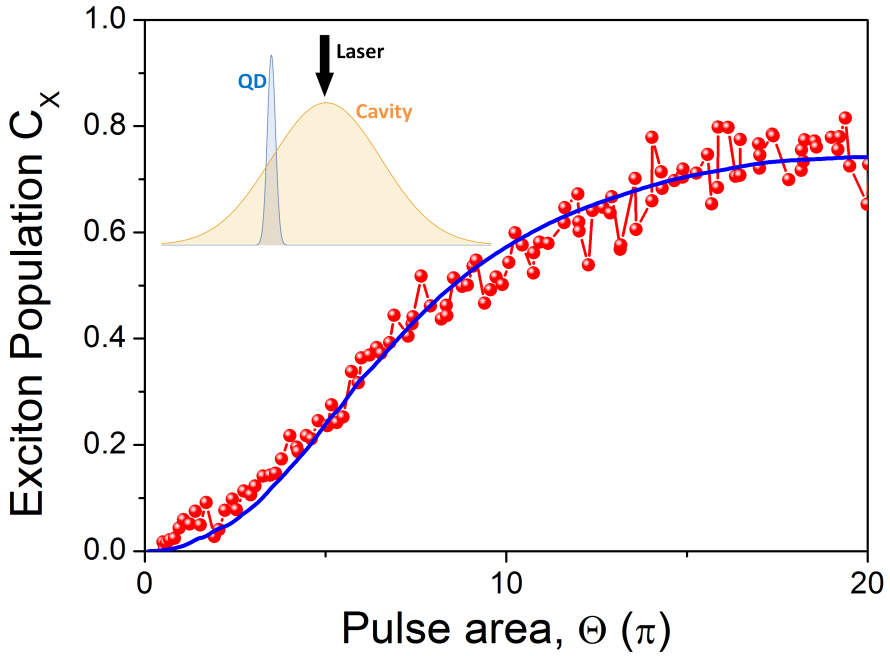

Figure 5.19: Exciton population as function of the pulse area for the laser resonant with the cavity and -0.65 meV detuned relative to the QD. Inset shows the relative place of laser, cavity and QD. The blue line is the result obtained from simulation for the same conditions appendix A.

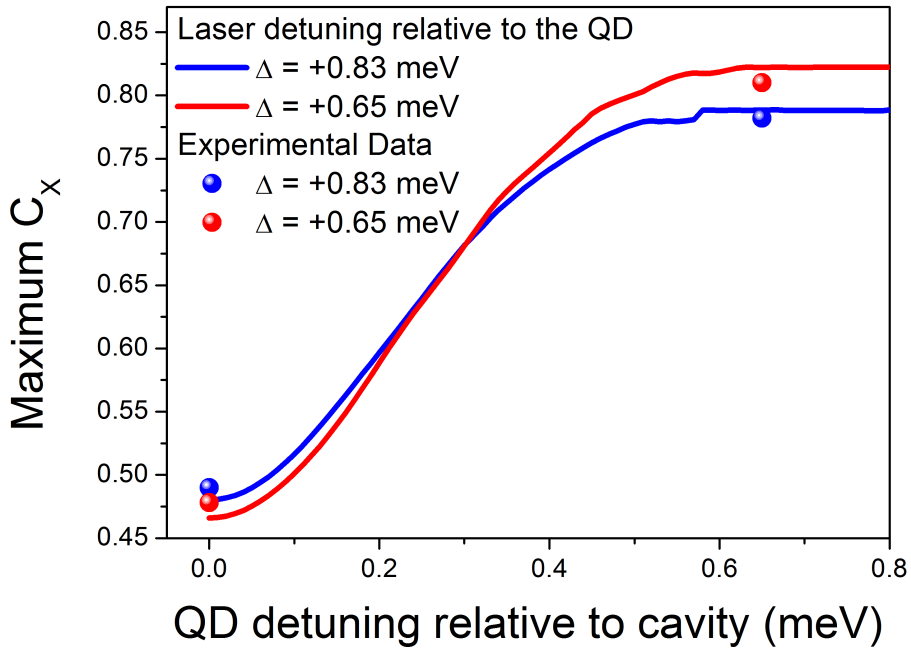

Figure 5.20: Maximum exciton population through phonon side band pumping at +0.65 meV (red dots) and +0.83 meV (blue dots) laser detuning relative to the QD. The blue and red line were obtained solving the equations in appendix A and assuming the power at which side band reaches the maximum, follows the cavity mode.

lation measurement as in the previous case section 5.3.1. In this experimental configuration the exciton is populated via the phonon assisted process. As shown in fig. 5.19 a higher exciton population is reached in this case (≈ 0.8) through the side band. This occurs because the QD is -0.65 meV detuned relative to the cavity and laser. Thus, the exciton–phonon coupling is expected higher than 0.43 and the two–level system approximation is valid for larger pulse area (≈ 20 before starting to vanish), even more power being necessary to achieve the same pulse area. The simulation (blue line) supports this interpretation. To further support this, the maximum inversion population as a function of the QD detuning relative to the cavity was simulated. Figure 5.20 shows the results of the simulation for laser–QD detunings of +0.65 meV (red line) and +0.83 meV (blue line). This simulation was obtained assuming that the power at which maximum

phonon side band occurs follows the cavity mode, as will be explained in the next section (section 5.3.3). The experimental data agrees with the simulation. However, more data is needed to fully confirm this interpretation.

As explained above, the QD can not be tuned further away, because the RF regime has a small bias range.

5.3.3 Cavity Influences in Phonon-Assisted Excitation

To see the full influence of the cavity on phonon assisted excitation, the RF of QDb was measured. This QD is -4.47 meV tuned relative to the cavity mode M1. Thus, the phonon side band must experience the cavity enhancement instead of the QD itself. As previously, the exciton population of QD is plotted as a function of the power and laser detuning. The graph is shown in fig. 5.21.

For this QD the phonon side band is much wider (≈ 10 meV) than for the previous QD (≈ 4 meV). The spectral density function for this QD is unknown. When the QD is driven resonantly, the Rabi oscillations would be expected. However, blinking emission was measured instead. [159,160]. As the Rabi oscillations are not visible there is no way to convert the RF emission to a calibrated exciton population.

A wide phonon side band is observed at positive detunings relative to the QDb [132]. The cavity enhances the phonon emission. As there are two cavity modes, the phonon side band has a W shape. This W shape is a piece of evidence of the cavity enhancement. When the side band is excited resonantly with the cavity modes (M1 and M2) the power needed to reach the maximum population is the lowest, as expected.

To see this enhancement clearly, several cross profiles of fig. 5.21 are shown in fig. 5.22. Here, the RF emission of QDb is plotted as a function of the square

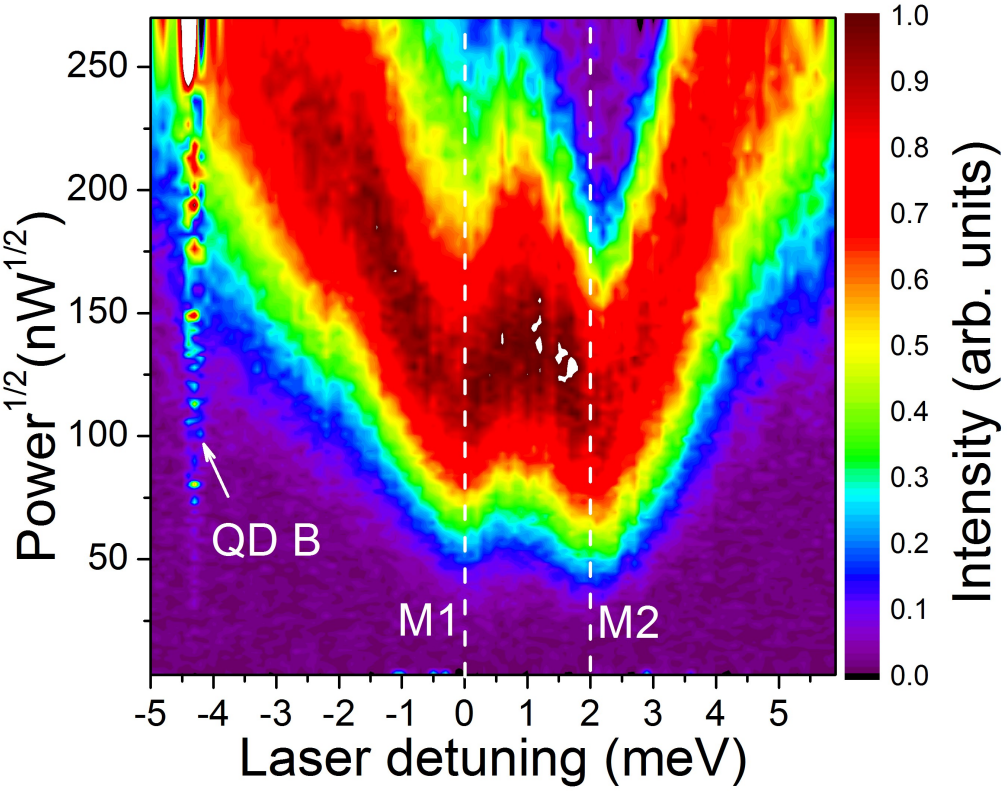

Figure 5.21: Exciton emission of QDb as function of power and detuning of the laser. QDb is -4.47 meV detuned relative to the mode $M1$.

root of laser power for four different laser detunings relative to M1, -3.5 meV, -2.5 meV, 0 meV (resonant with M1) and $+2.0$ meV (resonant with M2). P_{Max} is defined as the power at which the emission is strongest for each laser detuning. Figure 5.23 shows the $1/P_{\mathrm{Max}}$ as a function of the laser detuning. The shape matches with the cavity modes. This is a strong proof that the phonon side band is also enhanced by the cavity, and the explanation of this was presented in detail in section 5.2. This power enhancement is of the order of 6. This means, when the laser is resonant with cavity, 6 times less power is needed to obtained the maximum emission than when the laser is detuned far away relative to the cavity (> 3 meV). For the previous QD (see section 5.2) the enhancement of the π power was around a factor of 20.

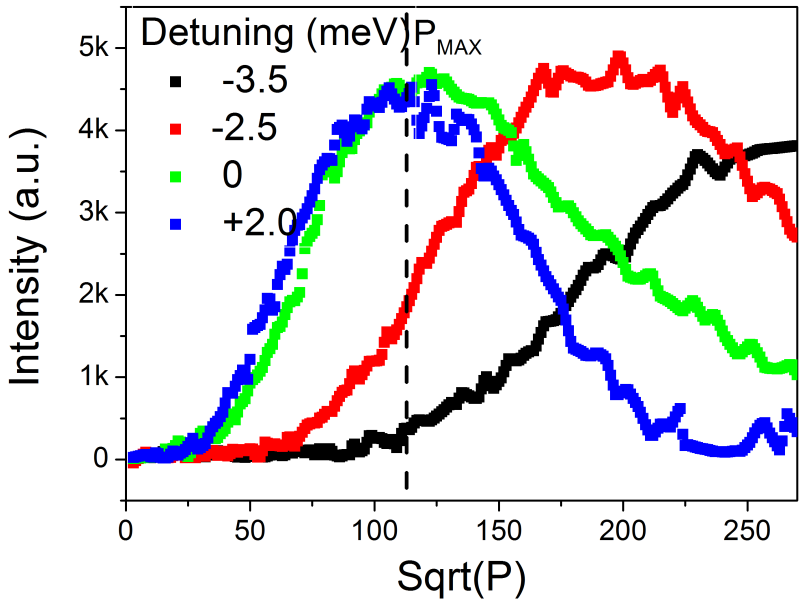

Figure 5.22: Exciton emission as function of the laser power for different laser detunings: −3.5 meV (black square), −2.5 meV (red square), 0 meV (green squares) and +2.0 meV (blue square). P_{Max} is the power at which the exciton emission is strongest.

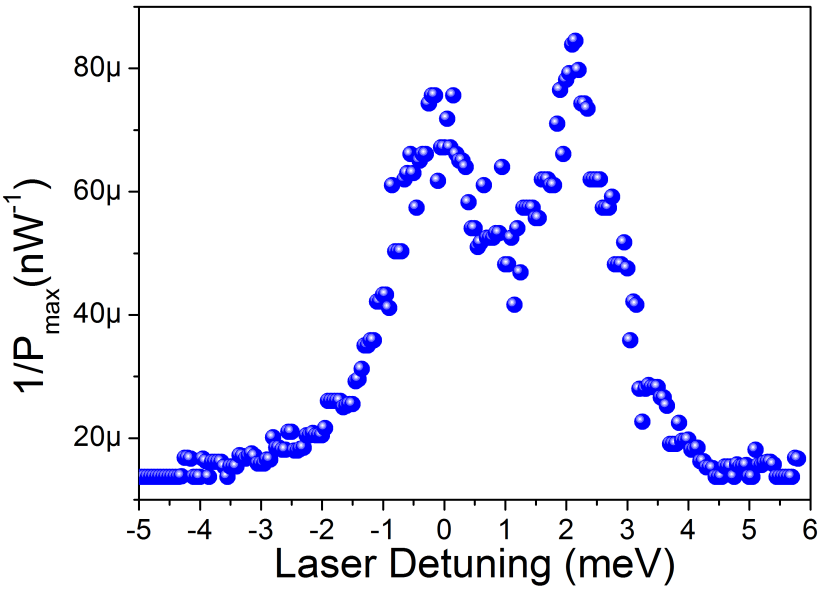

Figure 5.23: Inverses of the P_{Max} as function of the laser detuning relative to the mode $M1$.

5.4 Discussion & Conclusions

In this chapter the exciton–phonon interaction in a photonic crystal cavity was studied. In the "bad cavity" limit ($\kappa \gg \lambda, g$), the cavity enhances the electric field experienced by the QD as well as the exciton–phonon interaction. In this limit, the problem essentially is reduced to the spontaneous emission in the free space, since the cavity works as an electromagnetic reservoir [161]. However, even without any change in the physics of the exciton–phonon interaction, the cavity changes the environment in such a way that the results are very different from those observed for a bare QD.

The electric field enhancement by the cavity reduces the power necessary to create an exciton when the QD is at resonance with the cavity as seen in section 5.2. The cavity also enhances the spontaneous emission (as was discussed in the previous chapter). These two effects are enough to change radically the dynamics of the exciton–phonon interaction. In this chapter the main consequences due to the cavity enhancement were listed: lack of asymmetry in Mollow triplet; slow damping of Rabi oscillations; vanishing of the phonon side band at high pulse areas, and low inversion exciton population via phonon assisted process. All of them were extensively discussed and the interpretation was supported (whenever possible) by the theoretical simulations obtained from the master equation model presented in appendix A. These results are very important for Quantum Information Processing (QIP). The manipulation of a qubit using a very low number of photons is very attractive [162]. This allows the efficient and coherent transfer of the information from the photon to the QD. These results also give a bigger picture of the influence of the cavity on exciton–phonon interaction.

A new theoretical model and further measurements are necessary to complete the puzzle of the cavity and phonon effects on a QD. However, the results obtained so far show that a QD coupled with a cavity has some advantage when

compared with a bare QD. In the next chapter these advantages will be further explored.

Chapter 6

Ultrafast Optical Control of Light Scattering in a QD–Cavity System

6.1 Introduction

The nonlinear interaction between light and matter allows the possibility of building optical devices at a single–photon level. Devices such as single–photon switches/transistors [66, 67, 163] or controlled phase gates [9] have been demonstrated. In this chapter results on the nonlinear interaction between a quantum dot resonant with a cavity and photons inside the cavity will be presented. In the strong coupling regime it has also been shown that the quantum dot modifies the cavity transmission and reflection spectra [66, 67, 164]. This provides a mechanism for a large nonlinearity. However, the strong coupling regime requires a high Q–factor cavity and a precisely positioned QD where the electric field of the photonic crystal defect is at its maximum. Such requirements pose challenges to the fabrication techniques. Moreover, when other devices are coupled to the

cavity, such as, for example, waveguides, they create extra loss channels affecting the Q–factor of the cavity.

However, in the weak coupling regime a related nonlinear phenomenon has been observed. The change of the cavity transmission spectra is mediated by the local refractive index. This is modified when the QD is populated. Such phenomena have been reported in [165, 166] for self-assembled GaAs/AlGaAs QDs. In these works, the change of the refractive index induced by the quantum dots is quantified by measuring the optical phase shift (18^o) [165]. Thus, the QD works as a switcher. A similar phenomenon has been reported recently in [167]. In this case, the refractive index changes when the pump frequency is tuned relative to the semiconductor bandgap (optical Kerr effect). This change of the refractive index modifies the cavity transmission spectra.

Based on this phenomenon, an ultrafast control (few picoseconds) of the cavity emission is shown in this chapter. Moreover, a relative change of the cavity emission of 30% for π pulse is achieved. This opens the door to the single–photon devices.

6.2 Experimental Technique

To show the control of a scattered probe laser by the pump laser, the two pulse setup was used (see fig. 3.6). As the cavity frequency mode depends weakly on the bias voltage (see fig. 3.10), and consequently can affect the scattered light from the cavity, the setup was slightly modified. Modulation of the pump laser was used instead of the Differential Resonance Fluorescence technique (see section 3.5.3). To perform this, a chopper wheel was added in the pump laser path (see fig. 6.1(a)). The chopper wheel rotates at 22 Hz and was synchronized with the CCD (see fig. 6.1(b)). Thus, spectra with and without pump laser were

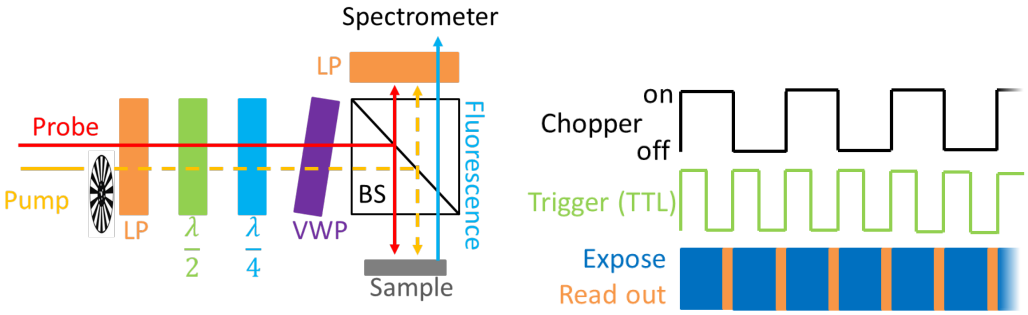

(a) (b)

Figure 6.1: a) Scheme of the experimental setup comprising of a chopper wheel, a linear polariser (LP), a half wave plate ($\lambda/2$), a quarter wave plate ($\lambda/4$), a variable wave plate (VWP) and a cube beam splitter (BS). b) Modulation scheme - the chopper wheel modulates the pump laser, exciting the QD (on) and blocking the laser (off).

measured multiple times, creating enough statistics to minimise the fluctuations (see inset of fig. 6.2(a). By subtracting one spectrum from the other, the change of the scattered light induced by the pump laser was obtained, as shown in fig. 6.2(a).

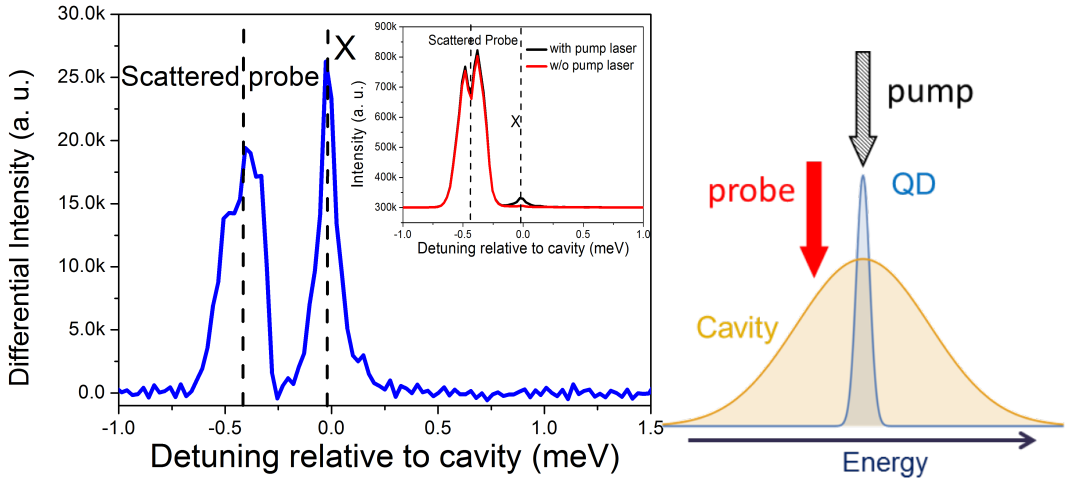

(a) (b)

Figure 6.2: a) Differential spectrum obtained by the subtraction of the spectra with and without the pump laser (inset graph). b) Schematic diagram of the configuration used to observe the change of the scattered light. The pump laser chopped by the chopper wheel is resonant with the QD. The probe laser is -0.40 meV detuned relative to the exciton (X). The exciton is resonant with cavity. The time delay between the pump and the probe laser is 20 ps.

6.3 Dependence of scattered light on pumping the QD

The nonlinear effect observed in the weak and strong coupling regime has a different nature. Whilst in the strong coupling regime the nonlinearity comes from the coupling between the exciton states and light states (polaritons) [164], in the weak coupling regime the nonlinear effect is mediated by the refractive index. Thus, the change of the scattered light is observed due to the change of the refractive index. Figure 6.3 shows the calculated refractive index (Δn) and the absorption for a QD exciton [165, 168–174]. These were easily computed using the Drude-Lorentz model [27].

$$\Re\left(\tilde{\epsilon}\right) = \Delta n = 1 + f\frac{\omega_0^2 - \omega^2}{\left(\omega_0^2 - \omega^2\right)^2 + \omega^2\Gamma^2} \tag{6.1}$$

and

$$\Im\left(\tilde{\epsilon}\right) \propto \alpha \propto \frac{\omega\Gamma}{\left(\omega_0^2 - \omega^2\right)^2 + \omega^2\Gamma^2}\,, \tag{6.2}$$

where f is the strength of the oscillator, ω_0 is the natural frequency of the oscillator and Γ is the damping rate. In the case under study, $\hbar\omega_0 = \hbar\omega_X = 1.3545$ eV, which is the exciton energy (resonant with cavity mode) and $\hbar\Gamma = \hbar\Delta\omega_X = 46\,\mu$eV is the linewidth of the exciton. These values were measured accurately. Figure 6.3 shows the variation of the refractive index (real part of the dielectric function – red line) and the absorption (proportional to the imaginary part of the dielectric function – black line). The imaginary and real part are related by the Kramers-Kronig relation.

The absorption and variation of the refractive index shown in fig. 6.3 is for a QD exciton. The QD becomes transparent when it is populated, which means that the QD cannot absorb light. Thus, the absorption profile for a populated QD

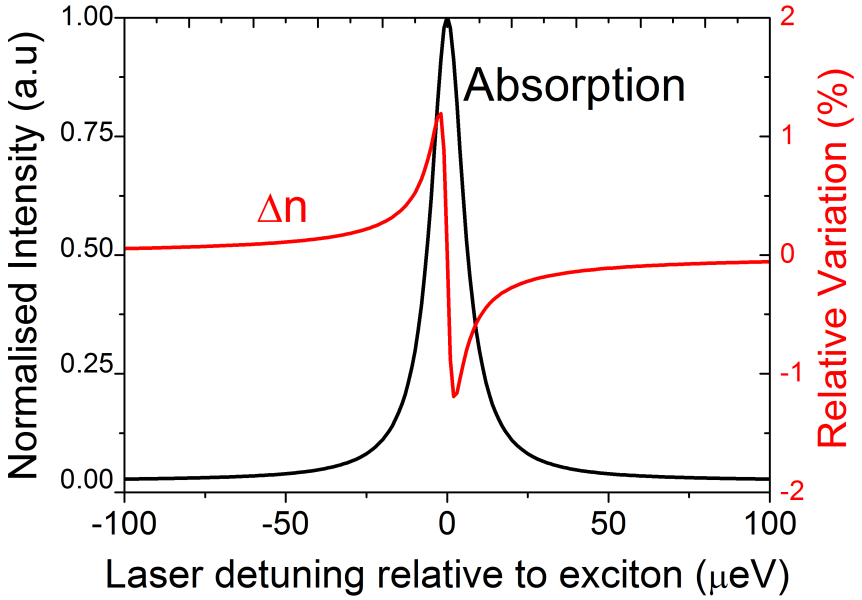

Figure 6.3: Change of the refractive index (Δn) when the exciton is excited (absorption line) [171].

becomes a flat line. Consequently, the variation of the refractive index vanishes to zero. This small variation of the refractive index due to the exciton (X) is enough to significantly change the scattered light from the cavity. The inset of fig. 6.2(a) shows the raw spectra measurement with (black line) and without (red line) the pump laser. The pump laser resonantly excites the QD with a pulse area of π. The QD is only visible when the pump is on, as expected. The probe is -0.5 meV detuned relative to the exciton as shown by the scheme in fig. 6.2(b). By subtracting the spectra from each other the differential spectrum is obtained and shows the exciton peak and the change in the scattered probe laser (see fig. 6.2(a)).

To confirm that the change of the scattered light is indeed due to the exciton population, the QD was moved out of the pump resonance, changing the voltage bias from 0.83 V to 0.89 V. In this way, the QD is detuned positively with respect to the pump laser, in order to avoid exciting the exciton via phonon assisted process. Therefore, the pump laser does not populate the QD. Figure 6.4(a)

shows the differential spectra for the QD resonant (black line) and off resonant (red line) with pump laser. The change of scattered light is only visible when the QD is excited (black line). When the pump laser is not resonant with the QD, the change of the scattered light drops to the background level. So far, the data presented just intended show the technique and the dependence of scattered probe light on pumping the QD. In the next section this dependence is studied for different probe detunings.

These results show clearly that the change of the scattered light depends on the exciton population. This fact is consistent with the theory. When the QD is populated the refractive index changes. This causes a change in the scattered light. Therefore, the QD works as a switcher, allowing the changes of the scattered light to turn on or off through the change of the refractive index.

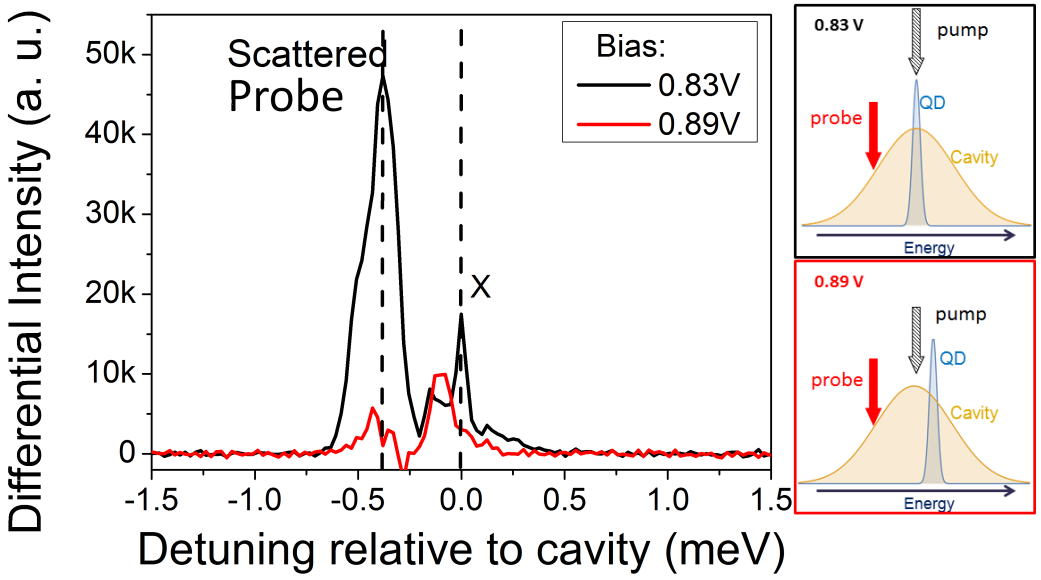

(a) (b)

Figure 6.4: a) Differential spectra for the QD resonant (black line) and the off–resonant (red line) with the pump laser (and cavity). The probe laser is -0.4 meV detuned relative to the cavity, the time delay between pump and probe laser is 20 ps and the pump and probe power is 25 nW (pulse area of π) and 263 nW, respectively. b) Schematic of the configuration used to observe the change of the scattered light. For 0.89 V the pump laser is not resonant with the QD.

The key quantity of this work is the relative change of the scattered light, $\Delta R/R_{\mathrm{w/o}}$, where $\Delta R = R_{\mathrm{w}} - R_{\mathrm{w/o}}$, R_{w} and $R_{\mathrm{w/o}}$ are, respectively, the intensity of scattered light measured with and without the pump laser. For clearness $\Delta R/R_{\mathrm{w/o}}$ is called $\Delta R/R$. The probe power dependence was measured to find the power which maximises the relative change of the scattered light. Figure 6.5 shows $\Delta R/R$ as a function of the probe power. The probe laser was +0.5 meV detuned relative to the QD. Note that previously the probe was −0.5 meV detuned. However, the oscillations of scattered probe laser as a function of square root of the pump laser is expected for different probe detunings. The maximum of $\Delta R/R$ is reached at 263 nW.

Note that the scattered laser light suppression was optimized at the QD energy. Thus the maximum $\Delta R/R$ is limited by the suppression quality at probe

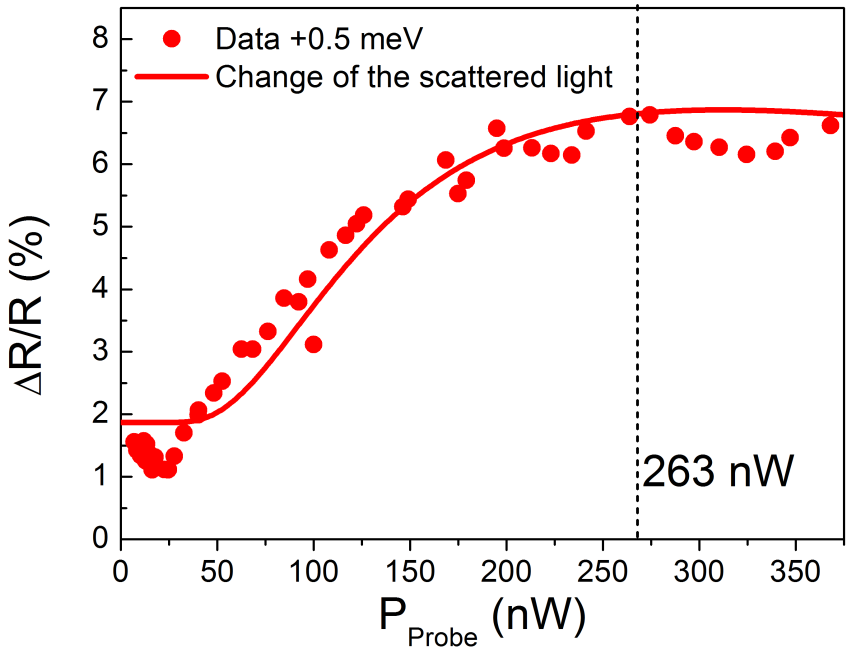

Figure 6.5: $\Delta R/R$ as a function of the probe power. The probe laser is +0.5 meV detuned relative to the QD and 20 ps delayed relative to the pump laser. The pump laser is resonant with QD (and cavity) and its power is 25 nW. The red line is just help to guide the eye of the reader.

energy and the detuning of probe laser. However the optimized power must not be affected by the quality of the suppression laser neither the detuning of the probe laser. In this chapter, all of the following results were measured with the optimized probe power (263 nW).

6.4 Time Dynamics

To understand the dynamics of this phenomenon, the time–dependence of the scattered probe light was measured. Figures 6.6(b) and 6.7(b) show the differential integrated intensity of the scattered probe light as a function of the time delay between the pump and probe laser for a blue–shifted (+0.5 meV) and red–shifted (−0.5 meV) probe laser, respectively. At negative time delays, as the probe arrives first, there is no change in the scattered light. At positive time delays, as the pump laser arrives first, the change in the probe scattered light is observed. This change follows the exciton population dynamics. From zero time delay the intensity rises abruptly until it reached the maximum at ≈ 16 ps. Since this corresponds to the laser pulse–width ($FWHM = 16.8$ ps), the change of the refractive index must occur at the same time scale or even faster. The change of scattered light is maximised when the probe laser finds the exciton fully populated. Then, the intensity of the probe scattered light decreases with the same decay time as the exciton lifetime (22.2 ps). This is illustrated in fig. 6.13. This is another piece of evidence that the probe scattered light is controlled by the exciton population. Figures 6.6(a) and 6.7(a) show the differential spectra for different time delays for blue–shifted and red–shifted probe laser, respectively.

To fit the differential integrated intensity data displayed in figs. 6.6(b)

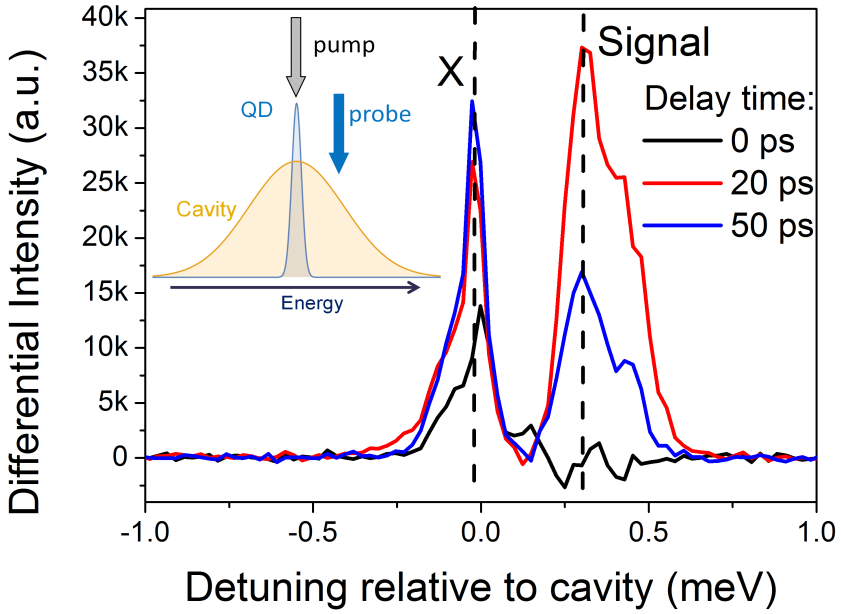

(a)

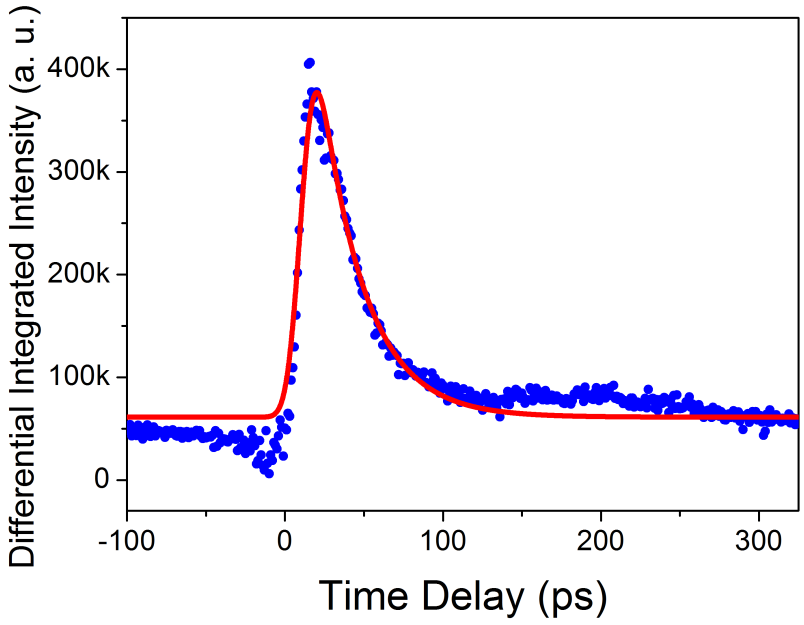

(b)

Figure 6.6: a) Differential spectra for 0, 20 and 50 ps. Inset: schematics of the experimental configuration. b) Differential integrated intensity of scattered blue shift probe light (blue dots). The red line was obtained fitting eq. (6.3). From the fit it was obtained the exciton lifetime of $\tau = 22.5$ ps.

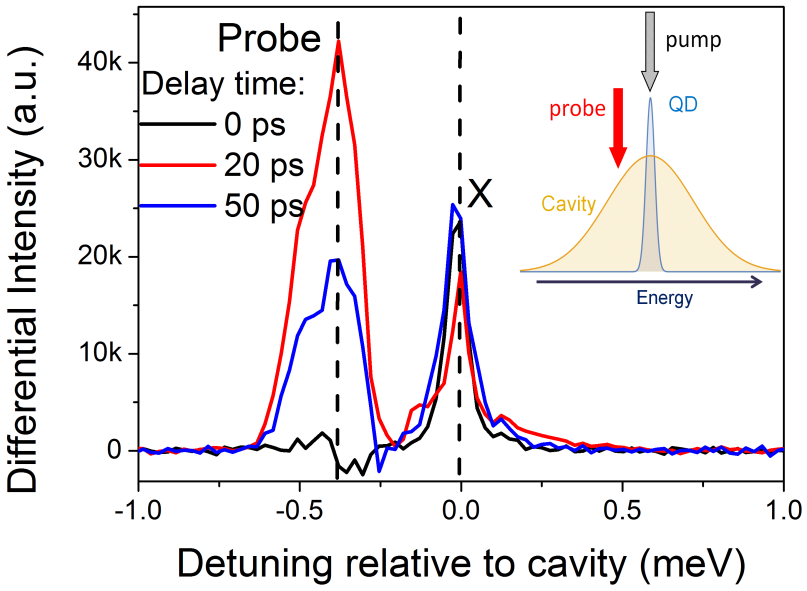

(a)

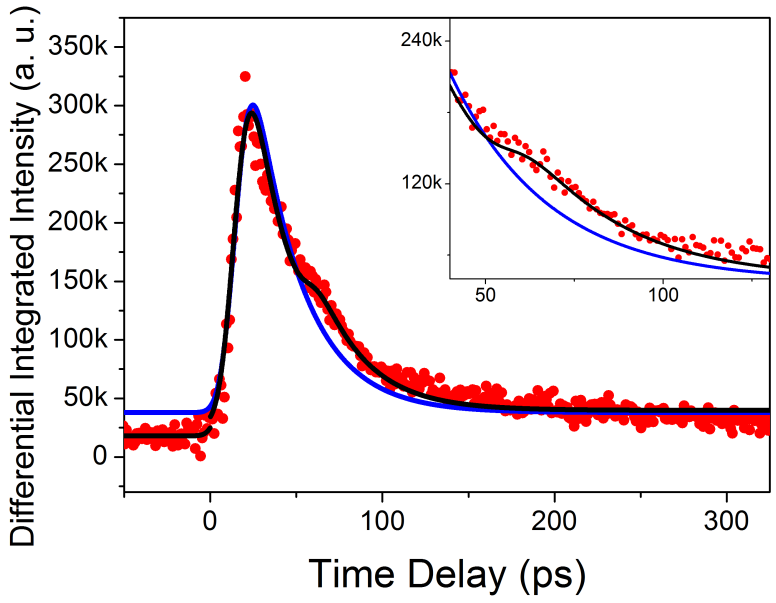

(b)

Figure 6.7: a) Differential spectra for 0, 20 and 50 ps. Inset: schematics of the experimental configuration. b) Differential integrated intensity of scattered red–shifted probe laser (red dots). The blue line was obtained by fitting eq. (6.3) assuming that the exciton lifetime is $\tau = 22.5$ ps. The black line was obtained fitting the eq. (6.5). Inset: Detail of the fitting where the agreement between the data and the fittings are clearer.

and 6.7(b) the following function was used:

$$f(t) = y_0 + \frac{A}{\tau} \exp\left(\frac{\omega^2}{2\tau^2} - \frac{t}{\tau}\right) \int_{-\infty}^{z} \frac{1}{\sqrt{2\pi}} \exp\left(-\frac{y^2}{2}\right) dy\,, \tag{6.3}$$

where $z = \frac{t-t_0}{\tau_0} - \frac{\tau_0}{t_0}$. Equation (6.3) corresponds to the convolution of a Gaussian laser centered at $t_0 = 0$ ps, with a FWHM $\tau_0 = 16.8$ ps and an exciton exponential decay function with a decay rate of τ. Besides A and y_0, τ is the only fitting parameter.

From the fitting it is possible to extract the exciton lifetime. The fitting curves displayed in figs. 6.6(b) and 6.7(b) assume that $\tau = 22$ ps. This value agrees with the exciton lifetime measured accurately (see section 4.3.2). These fittings agree very well when the probe is +0.5 meV detuned (see fig. 6.6(b)), but not quite so well when the probe is −0.5 meV detuned (see the blue line in fig. 6.7(b)). A possible reason for this discrepancy can be the stimulated photon emission from the de–excitation by the phonon assisted process as will be explained in section section 6.7.

6.5 Rabi Oscillations

In the previous section, the pump power used corresponded to the π pulse area. To calculate the π pulse area, the exciton amplitude was measured as a function of the square root of the pump power. The experimental configuration of this power dependence measurement is the same as in fig. 6.2(b). The probe laser power was constant (263 nW) and the delay time between pump and probe was $\approx$ 20 ps, which corresponds to the maximum relative change of scattered light, as shown in section 6.4. As the pump laser is resonant with the exciton, the Rabi oscillations of the exciton peak are observed as shown at the bottom of fig. 6.8. The scattered light follows the Rabi oscillation of the exciton, showing

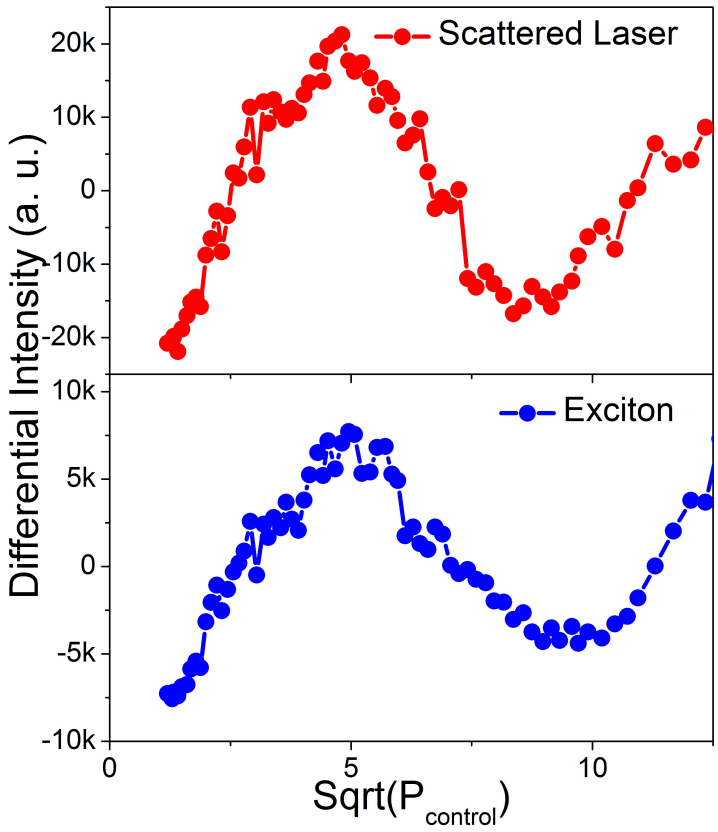

Figure 6.8: Differential intensity of scattered light (red) and the intensity of exciton peak (blue) as a function of the square root of the pump laser power. The exciton is resonant with cavity and with the pump laser. The probe laser power is constant (263 nw) and it is 0.5 meV detuned relative to the exciton. The delay time between the pump and probe laser is $\approx$ 20 ps. The linear laser background was subtracted from the data.

a direct relation between the scattered light and the exciton population (see top of fig. 6.8). This means, the relative variation of scattered light is proportional to the exciton population. Note that, the negative intensity is a consequence of the linear background subtraction, does not have any physical meaning. The π power of 25 nW was extracted from the data in fig. 6.8. From DFTD simulations (see section 4.4.1), this π power corresponds to 7 photons. As shown in previous chapters such π power can be reduced to 8 nW (see fig. 5.6(a)), which corresponds to 2.44 photons.

6.6 Relative Change of Scattered Light

In the previous sections, the deep relationship between the probe scattered light and the exciton population was shown. Here, the origin of the scattered light is studied. This relationship between the scattered light and the exciton is due to the change of the refractive index, when the QD is populated (see section 6.3). The refractive index is given by eq. (6.1) [165,168–174]. This change of refractive index is very small ($\approx 1\%$) and is plotted in fig. 6.3 (red line).

The cavity emission follows a Lorentzian function of the form:

$$I_C = A\frac{\Delta}{4\left(\omega-\omega_C\right)^2+\Delta^2}\,, \tag{6.4}$$

where A is the amplitude, $\Delta = 2.22$ meV is the width of the cavity emission and $\omega_C = 1.3545$ eV is the resonant energy mode of the cavity. The PL of the cavity is shown in fig. 6.9 as the black line. From a Lorentzian fit (black dotted line), the parameters Δ and ω_C were obtained.

The resonant energy mode of the cavity is proportional to $\omega_C \propto 1/n$ [175]. Thus, eq. (6.4) is the cavity emission when no exciton is present. When an exciton is present the refractive index changes and the resonant energy mode of the cavity is now proportional to $\omega'_C \propto 1/(n-\Delta n)$, where Δn is given by eq. (6.1). Replacing ω'_C by ω_C in eq. (6.4), the cavity emission in the presence of the exciton is obtained, I'_C. Figure 6.9 shows the relative change of the cavity emission, $\left(I'_C - I_C\right)/I_C$ (blue line). This data was obtained suppressing the probe laser instead the pump as in fig. 6.5. This difference explains the different $\left(I'_C - I_C\right)/I_C$ values presented in figs. 6.5 and 6.9.

The data measured (red dots) agree very well with the theoretical calculation (blue line). The only fitting parameters to calculate the theoretical relative change of the cavity emission were the amplitude and the maximum of the change

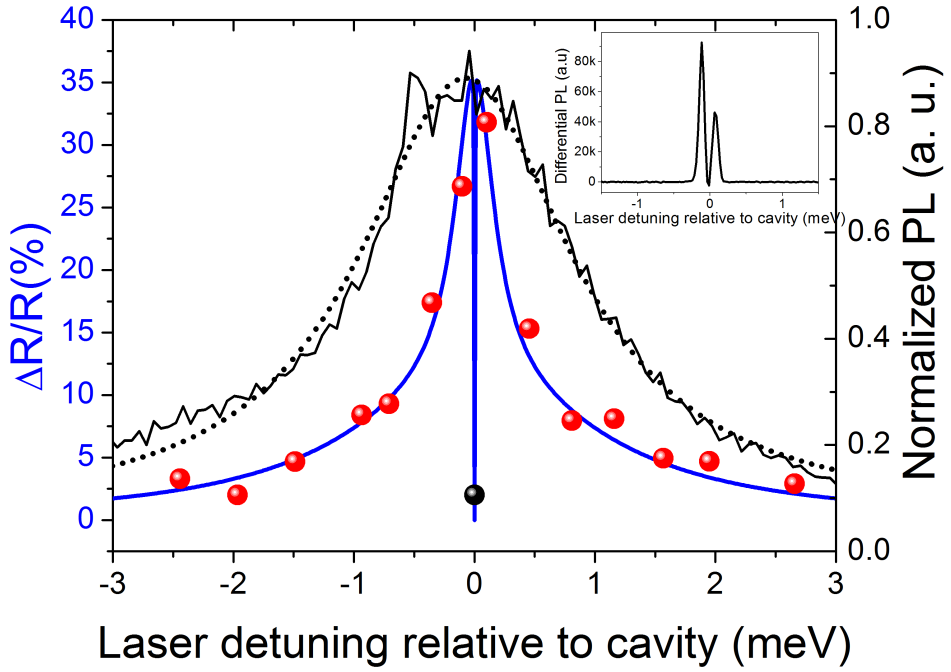

Figure 6.9: Relative change of the scattered light as a function of probe detuning laser (red dots). The blue line is the theoretical function (only the amplitude and the maximum of the refractive index were used as fitting parameters). The cavity mode is the solid black line and the dot line is the Lorentzian fit of the cavity mode. The experimental value measured at 0 detuning is represented as a black dot to highlight the uncertainty associated to this value. Inset: Differential spectrum at 0 detuning (black dot).

of the refractive index. $\Delta n_{\text{maximum}}$ obtained was $\approx 1\%$. This value is consistent with the literature [168–170,174]. At 0 meV detuning, the RF of exciton overlaps with scattered light from the cavity, so the $\Delta R/R$ (black dot) is not accurate. The inset of fig. 6.9 shows the differential spectrum of the measurement at 0 meV detuning. Two peaks and a valley are observed because the probe laser is 0.2 meV wide. The valley corresponds to the exciton energy. Since it is not possible to separate the exciton RF from the cavity scattered light, the calculation of the relative change of scattered light is not accurate. However, assuming that the exciton RF is smaller than the scattered light, the relative change of scattered light at 0 meV drops significantly. Moreover, a similar phenomenon has been reported in [176]. They shown that the QD dipole induces transparency on resonant cavity

transmission, such as the phenomenological model (blue line) predicts.

This excellent agreement between the experimental data and this simple model indicates that the scattered light is from the cavity and not from the probe laser. Since the π power (25 nW) corresponds to 7 photons (being possible to reduce it to 2.44 photons), a relative change of the scattered light of 33% is controlled by few photons on average.

6.7 Exciton coupled with a Phonon Bath

The inset of fig. 6.7(b) shows that the blue fitting function does not agree with the data (red dots). In this section a possible explanation is purposed and discussed. As the probe is detuned relative to the QD, the phonon assisted processes have to be taken into account. In the previous chapter the effects of LA phonons on a QD coupled with a cavity were discussed in detail.

The side bands due to the phonon emission process are shown in fig. 6.11. The pump laser modulation technique allows the measurement of both de–excitation and excitation side bands when the probe laser energy is scanned. These two processes were introduced in section 2.6.4. Figure 6.10 shows schematically respec-

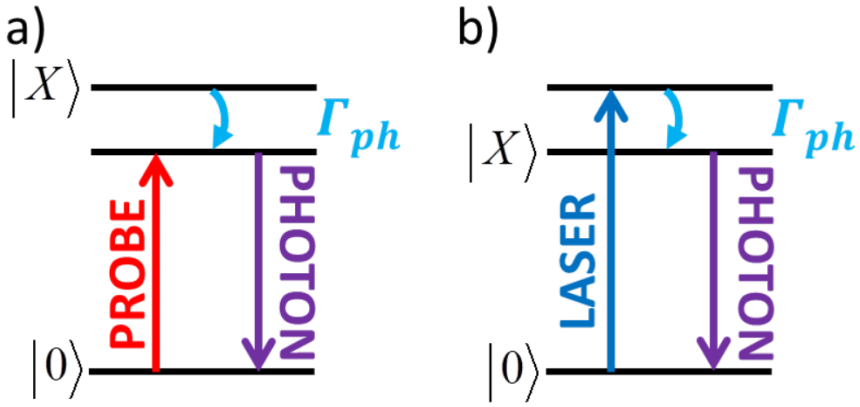

Figure 6.10: Phenomenological energy level diagrams of de–excitation (a) and excitation (b) of an exciton by emission of a phonon (blue arrow).

tively the de–excitation and excitation of an exciton by assisted phonon emission. The spectra with the pump and probe laser enable the de–excitation side band to be obtained. The pump excites the QD with π pulse area, creating an exciton. The detuning of the probe laser, 20 ps delayed, is scanned. When the probe is at negative detuning energies, it de-excites the exciton. At positive detunings the probe does nothing, once the QD is populated (fig. 6.10a)). This corresponds to the red line spectrum in inset of fig. 6.11. On the other hand the excitation side band is visible in the spectrum measured only with the probe laser. At negative detunings the probe can not excite the QD because, as mentioned in section 2.6.4, the absorption of a phonon is very unlikely at cryogenic temperatures. Otherwise, at positive detunings the probe can create an exciton by phonon emission process. This corresponds to the black line in the inset of fig. 6.11. Subtracting them, both phonon side bands are visible in the differential spectrum (fig. 6.11).

As a result of the phonon assisted de–excitation (fig. 6.10 (a)), a phonon and a stimulated photon are emitted (see inset of fig. 6.13). Since the probe and the stimulated photon emitted have the same energy, stimulated photon emission contributes to the probe scattered light. For phonon assisted excitation (fig. 6.10 (b)), as the photon emitted has the same energy as the exciton, the probe scattered light measured is not affected.

To take into account the extra stimulated photon, the time dynamics of the exciton population was measured using two pulses, pump and probe, which is -0.5 meV detuned (see fig. 6.12). The dip at 0 time delay is due to the AC-Stark shift (see section 2.5.2). The AC Stark shift is only observable when the red–shifted laser arrives first. This shift follows the Gaussian envelope of the laser electric field as would be expected from the $\Omega_R(t)$ term in eq. (2.8). At zero time delay, as the pump and the probe lasers overlap, the AC Stark shift starts to vanish and consequently the pump laser starts to excite the exciton. This

depends only on the laser line–width.

As with in fig. 6.7(b) a *bump* is also observed in fig. 6.12. This is because of the phonon assisted de–excitation. The amount of exciton de–excited (same amount of stimulated photons emitted) depends on the amount of the exciton previously existent and the relaxation time of the phonon. Thus, at time delays near 0 ps, the exciton population is very low, so the probe laser does not have any exciton to de–excite. For a longer time delay the probe laser finds the QD empty, this is because the exciton lifetime is very short ($\approx$ 22 ps). For time delays shorter than the exciton lifetime, the probe laser de–excites the exciton.

The black line plotted in fig. 6.7(b) is the fitting which takes into account the extra stimulated photons. These extra stimulated photons result from the

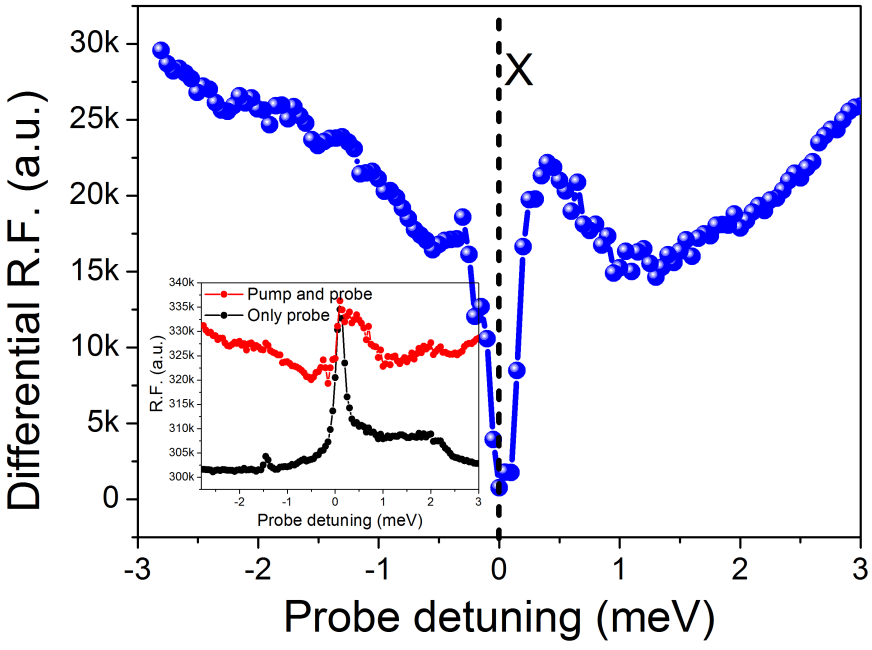

Figure 6.11: Differential exciton intensity as function of probe detuning energy. The positive (excitation) and negative (de–excitation) phonon side band are visible. X indicates the exciton energy position. Inset: Raw data of exciton intensity measured with (red dots) and without (black dots) pump laser. The time between the pump and the probe laser was 20 ps

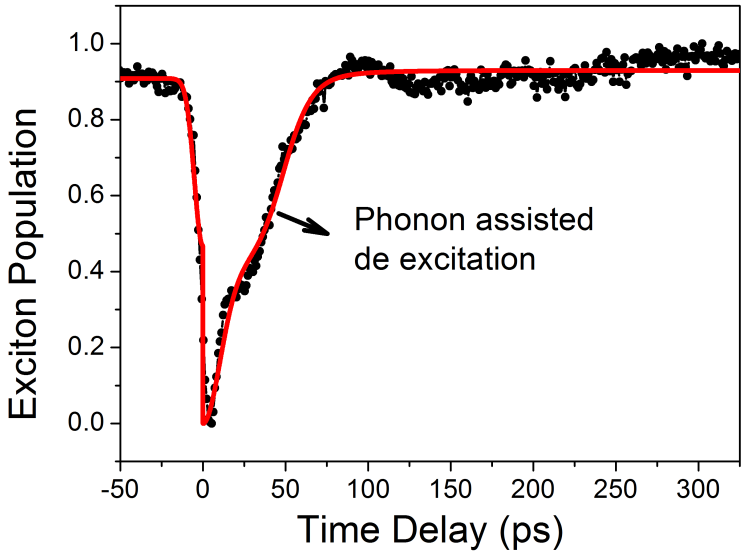

Figure 6.12: Exciton population as a function of the time delay between the pump and the probe laser, for probe laser -0.5 meV detuned relative to the QD (black dots). The phonon assisted de–excitation is indicated by the arrow. The red line was obtained by fitting eq. (6.5).

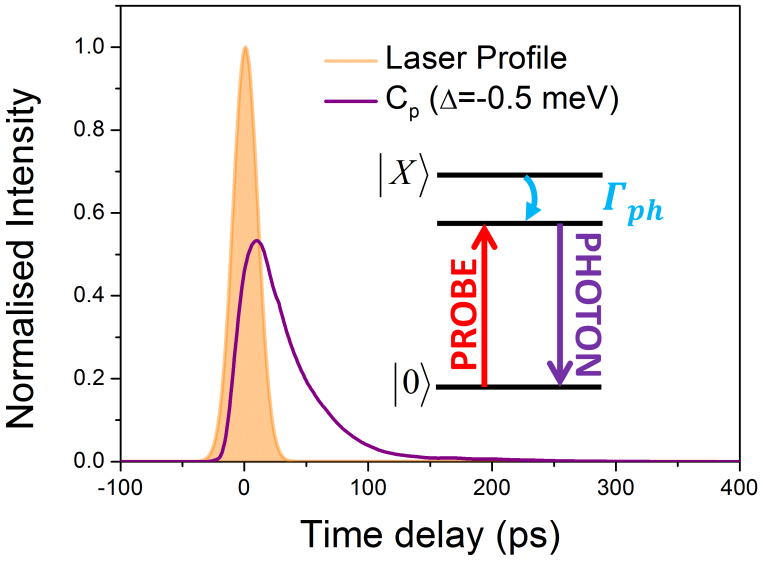

Figure 6.13: Temporal evolution of the stimulated photon emission (purple line) for the laser -0.5 meV detuning relative to the QD. The orange line corresponds to the laser profile. In inset the energy diagram of the de–excitation of an exciton via phonon emission. The purple arrow corresponds to the stimulated photon emission, which has the same frequency as the probe laser.

phonon assisted de–excitation. Thus, the function has the form:

$$f_{\text{phonon}}(t) = f(t) \times (1 + C_P(t - t_p)) \ , \tag{6.5}$$

where $f(t)$ is the function in eq. (6.3), $C_P(t-t_p)$ is the fraction of the exciton de–excited by the phonon assisted process as a function of the time delay. $C_P(t-t_p)$ was computed by solving numerically eq. (A.23). The solution is displayed as the purple line in fig. 6.13. The orange line represents the laser profile. Note that the solution takes into account the exciton lifetime of 22.5 ps. The red line in fig. 6.12 is obtained using the same function (eq. (6.5)), since the principle behind it is the same. The same fitting parameters, $t_p = 48.58$ ps and $\tau_p = 4.17$ ps, were used for both graphs. τ_p (the phonon relaxation time) agrees with the values in literature [147, 148, 154]. However t_p (centered time of phonon emission) is ≈ 50 ps, when the expected would be 0. This difference is not yet understood. Regardless of the difference between the t_p expected and obtained, the good level of agreement between the results and the fittings, and the fact that the same fitting parameters were used for both graphs, helps to support the interpretation that the *bump* observed in fig. 6.7(b) is indeed due to the stimulated emitted photon resulting from the phonon assisted de–excitation process [56]. However, further measurements are needed to confirm the stimulated emitted phonon interpretation.

6.8 Discussion & Conclusions

In this chapter, the control of the scattered probe laser was presented. The mechanism causing the change of scattered light is the change of the refractive index when the exciton is created (see fig. 6.3). This phenomenon is rather different than what has been present in previous studies [66, 67, 164]. The advantages of

this are:

a) The scattered light is related to the cavity emission. As the cavity is very broad (low Q–factor), the change of the scattered light is visible in a wide range;

b) The maximum value of $\Delta R/R$ measured was $\approx$ 33 %. This value was caused by a small change of the refractive index ($\approx$ 1%). $\Delta R/R \approx 33\%$ is comparable with the values presented by few papers such as [66, 67, 164], (8%–44%). However, the scheme where the strong coupling regime is used is limited by the QD–cavity coupling strength. Here the relative change of scattered light is limited by the quality of the laser suppression and the lifetime of the cavity (see fig. 6.5);

c) The schemes where the strong coupling regime is used, need a very precise fabrication process to achieve high Q–factors. Here, the quality of the cavity is not a constraint; thus the scheme presented in this chapter can be easily achieved and can even be integrated on a chip with waveguides and other devices.

The scattered light can be controlled on an ultrashort time scale, 16 ps (see section 6.4). This is only limited by the temporal pump laser width. As the change of scattered light is mediated by the refractive index, it would be possible to reduce the control time of the scattered light, simply by reducing the time width of the pump laser.

The influence of the phonons was also discussed in this chapter (see section 6.7). To explain the difference between the scattered light time dynamics between the red (fig. 6.7(b)) and blue (fig. 6.6(b)) shifted laser, the phonon assisted de–excitation mechanism was assumed as the hypothesis. However further measurements are needed to confirm this interpretation.

Chapter 7

Conclusions & Outlook

7.1 Conclusions

In this thesis an extensive study of the QD–PhCC system in the weak coupling regime has been presented. The majority of the experimental results were obtained by driving the QD resonantly with an ultrafast pulse laser and detecting its resonance fluorescence (RF) signal. This required the development of new techniques: the Differential Resonance Fluorescence (see section 3.5.3), which allows measurements of QD RF even at high pulse area, and the Two Pulse Resonance Fluorescence, which enables measurements of very high time resolution (see section 4.2). A wide range of topics was explored in this thesis and from those experimental results, the following conclusion can be drawn:

- The spontaneous emission of the QD can be strongly enhanced, by coupling a QD with a photonic crystal H1 cavity. A huge Purcell factor of 42 and a very short exciton life time of 22 ps were obtained when the QD was resonant with the cavity mode. To measure such a short lifetime a new technique was developed (TPRF–see section 4.2). This is the largest Purcell factor and the shortest exciton lifetime reported so far. This enhancement is one

of the main results presented in this thesis. One of the consequences of this huge enhancement is that the QD can be fully populated with only few photons. In fact, following the FDTD simulations, only 2.44 photons on average are necessary to fully populate the QD.

- Due to the short life time, a near–ideal single photon source (86% of purity and 90% of indistinguishability), was measured. The source was coupled on–chip to output waveguides. The source operated with only a few photons creating the exciton. This was a huge step forward in overcoming the scalability issue.

- Furthermore, it was shown that the relative variation of the cavity emission depends on the exciton population. Thus, the cavity emission can be controlled only using a few photons. This control occurs in an ultrafast time scale (16 ps).

- Last but not least, the cavity plays a huge role in the exciton–phonon interaction. This is not yet completely understood. However, the results in chapters 4 and 5 show that the fast spontaneous emission overcomes the dephasing, so long coherence times were obtained. Moreover, as the cavity also enhances phonon emission, the full monotonic phonon side band was observed. The simulations obtained from the master equation simulations agreed with the data.

Summarizing, the cavity enhances the QD emission in such a way as to bring semiconductor QD physics to near the single photon level. This is a remarkable result, even more so in a weak coupling regime.

7.2 Future Work

The work presented in this thesis shows that a QD–cavity system is rich in physics phenomena and has many potentialities. To explore further this versatile system, some possible future directions for research can be suggested:

7.2.1 QD Source in Quantum Circuits

The large Purcell factor reported in this thesis is the largest measured so far. This is remarkable taking into account the poor Q–factor of the cavity. The new technique used here (namely the TPRF technique) had better time resolution than the techniques used in previous studies and allows measurement of such strong Purcell factors. This new technique based on resonant excitation avoids the relaxation jitter times, which occur for p–shell and above band gap excitations. Therefore, a very short exciton lifetime was measured. Such short exciton lifetimes open up a range of new experiments on–chip, as for example time multiplexed output [177] and HOM measurements [178]. This may be possible because the delay time required for such a fast quantum emitter is able to be fabricated on–chip.

However before such on–chip measurements, it would be worth investigates the Purcell factor for different QD–cavity systems, using the new TPRF technique, for better quality cavities (higher–Q factors).

7.2.2 Spin Photon Coupled to a Cavity

In this thesis it has been seen how the cavity enhances the QD optical properties. This enhancement brings advantages for spin control, and quantum networks. The initialisation, rotation and read out of a single electron spin qubit coupled to

a photonic crystal cavity has been demonstrated [179, 180]. Schemes such these are possible because single carriers have longer lifetimes than the exciton. For this purpose a three energy level in a Λ configuration (with two ground states and an optically excited state) is used. The optically excited state corresponds to a charged state. For cavity–dot coupling strengths as strong as the one shown in this thesis, the initialisation time could decrease to picosecond timescales, improving qubit operation speed, as has been shown in this thesis. Moreover, as the quantum dot eigenstates are aligned to the cavity polarization, the cavity-enhanced transitions could be used for single-shot readout, since this results in a very bright cycling transition.

Appendix A

Theoretical Model of Exciton coupled to a Phonon Bath

A.1 Master Equation

The model that describes the interaction of a two–level system coupled to a phonon bath and with an optical cavity is [135, 136]:

$$H = \Delta\sigma_+\sigma_- + \frac{\Omega_c(t)}{2}\left(a^\dagger + a\right) + \sum_{\mathbf{q}} \omega_{\mathbf{q}} b^\dagger_{\mathbf{q}} b_{\mathbf{q}} + \hbar f\left(\sigma_- a^\dagger + \sigma_+ a\right) + \sigma_+\sigma_- \sum_q \left(g_{\mathbf{q}} b^\dagger_{\mathbf{q}} + g^*_{\mathbf{q}} b_{\mathbf{q}}\right) , \quad \text{(A.1)}$$

where $g_{\mathbf{q}}$ (f) defines the exciton-phonon (exciton-photon) coupling, $b_{\mathbf{q}}$ $(a)$are the phonon (photon) annihilation operators and $\sigma_+ = |0\rangle\langle X|$ $(\sigma_- = |X\rangle\langle 0|)$. The rotating wave approximation was used to obtain eq. (A.1) .

The above Hamiltonian can be simplified assuming a bad cavity limit.

Thus the Hamiltonian becomes:

$$H = \Delta\sigma_+\sigma_- + \frac{\Omega_{eff}(t)}{2}\sigma_x + \sum_{\mathbf{q}} \omega_{\mathbf{q}} b^\dagger_{\mathbf{q}} b_{\mathbf{q}} + \sigma_+\sigma_- \sum_q \left(g_{\mathbf{q}} b^\dagger_{\mathbf{q}} + g^*_{\mathbf{q}} b_{\mathbf{q}}\right) , \qquad (A.2)$$

where $\Delta = \omega_X - \omega_L$ is the laser detuning relative to the exciton. The exciton is driven by an optical pulse $\Omega(t) = g\Omega'(t)/\sqrt{\kappa^2 + \Delta^2_{Lc}}$ where Δ_{Lc} is the laser detuning relative to the cavity, κ is the cavity decay rate and $\Omega'(t) = \Theta \exp\left(-t^2/(2\tau_p^2)\right)/(\tau_p\sqrt{2})$, τ_p being the pulse half width and $\Theta = \int_{-\infty}^{+\infty} \Omega(t')dt'$ the pulse area. In this way, the cavity enhancement is taken into account as explained in section 5.1.1. The phonon bath consists of harmonic oscillators with wave vector $\mathbf{q}$ and frequency $\omega_{\mathbf{q}} = v_s|\mathbf{q}|$, where v_s is the speed of sound. It is assumed here that only acoustic phonons need to be considered due to the near resonant conditions.

The deformation potential coupling strength is

$$g_{\mathbf{q}} = \frac{q}{\sqrt{2\hbar\omega_{\mathbf{q}}\eta V}} \left(D_e P\left[\psi^e(\mathbf{r})\right] - D_h P\left[\psi^h(\mathbf{r})\right]\right) , \qquad (A.3)$$

where η is the mass density of the host material, V the lattice volume, D_e (D_h) the respective bulk electron (hole) deformation potential constants, and $P[\psi^{e(h)}]$ denotes the form factor of the electron (hole) wavefunction.

The total Hamiltonian can be divided into $H = H_0 + H_I$, where $H_0 = H_X + H_B$ is the non interaction Hamiltonian given by the sum of the exciton and phonon bath Hamiltonians:

$$H_X = \Delta\sigma_+\sigma_- + \frac{\Omega(t)}{2}\sigma_x \, , \qquad (A.4)$$

$$H_B = \sum_{\mathbf{q}} \omega_{\mathbf{q}} b^\dagger_{\mathbf{q}} b_{\mathbf{q}} \, , \qquad (A.5)$$

and the interaction Hamiltonian H_I is given by:

$$H_I = \sigma_+\sigma_- \sum_q \left(g_{\mathbf{q}} b^\dagger_{\mathbf{q}} + g^*_{\mathbf{q}} b_{\mathbf{q}}\right) . \tag{A.6}$$

The interaction Hamiltonian can also be written as $H_I = S \otimes B$, where $S = \sigma_+\sigma_-$ and $B = \sum_q \left(g_{\mathbf{q}} b^\dagger_{\mathbf{q}} + g^*_{\mathbf{q}} b_{\mathbf{q}}\right)$. To derive the master equation [181, 182] the Hamiltonian must be written in the interaction picture:

$$H_I(t) = S(t) \otimes \sum_q \left(g_{\mathbf{q}} b^\dagger_{\mathbf{q}} e^{i\omega_{\mathbf{q}}t} + g^*_{\mathbf{q}} b_{\mathbf{q}} e^{-i\omega_{\mathbf{q}}t}\right) . \tag{A.7}$$

To derive $S(t)$ the diagonal system of H_X has to be found. The eigenvectors of H_X are the dressed states:

$$|\Psi_1\rangle = \frac{1}{\sqrt{2\Lambda}}\left[-\sqrt{\Lambda-\Delta}|0\rangle + \sqrt{\Lambda+\Delta}|X\rangle\right] \tag{A.8}$$

$$|\Psi_2\rangle = \frac{1}{\sqrt{2\Lambda}}\left[\sqrt{\Lambda+\Delta}|0\rangle + \sqrt{\Lambda-\Delta}|X\rangle\right] , \tag{A.9}$$

where $\Lambda = \sqrt{\Delta^2+\Omega^2}$ and the eigenvalues are $\lambda_\pm = \Delta/2 \pm \Lambda/2$. Thus, S in interaction picture becomes:

$$\begin{aligned} S(t) =& \frac{1}{4\Lambda^2}\begin{bmatrix} -\sqrt{\Lambda-\Delta} & \sqrt{\Lambda+\Delta} \\ \sqrt{\Lambda+\Delta} & \sqrt{\Lambda-\Delta} \end{bmatrix}\begin{bmatrix} e^{-i\lambda_+ t} & 0 \\ 0 & e^{-i\lambda_- t} \end{bmatrix}\begin{bmatrix} -\sqrt{\Lambda-\Delta} & \sqrt{\Lambda+\Delta} \\ \sqrt{\Lambda+\Delta} & \sqrt{\Lambda-\Delta} \end{bmatrix} \\ =& \frac{1}{4\Lambda^2}\left[\Omega\left(\sigma_+ e^{i\Lambda t} + \sigma_- e^{-i\Lambda t}\right) - \Delta\sigma_z + \Lambda I\right] . \end{aligned} \tag{A.10}$$

To simplify $S(t)$, $\Lambda(t)$ is assumed constant once the width of the excitation laser is larger than the phonon relaxation time 1 ps [147, 148, 154].

To compute the master equation two assumptions are made. First, the coupling between the exciton and the phonon bath is weak such that $\rho(t) =$

$\rho_X(t) \otimes \rho_B$, where ρ_B is the density matrix of the phonon bath in thermal equilibrium. Second, the memory effects of the phonon bath are neglected since the excitonic systems varies much slower than the phonon relaxation. These two conditions correspond to the Born-Markov approximation. Thus the time local Redfield equation becomes

$$\dot{\rho} = -\frac{1}{\hbar^2}\int_0^{+\infty} ds' \mathrm{Tr}\left([H_I(t),[H_I(t-s'),\rho(t)\otimes\rho_B]]\right) . \tag{A.11}$$

The upper limit of integration can be $+\infty$ once the bath memory time is very short. Expanding out the commutator

$$\begin{aligned}\dot{\rho}(t) = -\frac{1}{\hbar^2}\int_0^{+\infty} ds \Big[& S(t)S(t-s)\rho(t)\left(\langle R^\dagger(t)R(t-s)\rangle + \langle R(t)R^\dagger(t-s)\rangle\right) \\ & -S(t)\rho(t)S(t-s)\left(\langle R(t-s)R^\dagger(t)\rangle + \langle R^\dagger(t-s)R(t)\rangle\right) \\ & -S(t-s)\rho(t)S(t)\left(\langle R(t)R^\dagger(t-s)\rangle + \langle R^\dagger(t)R(t-s)\rangle\right) \\ & +\rho(t)S(t-s)S(t)\left(\langle R^\dagger(t-s)R(t)\rangle + \langle R(t-s)R^\dagger(t)\rangle\right)\Big] ,\end{aligned} \tag{A.12}$$

where $R(t) = \sum_{\mathbf{q}} g_{\mathbf{q}} b_{\mathbf{q}} e^{-i\omega_{\mathbf{q}}t}$ and the terms $\langle R^\dagger R^\dagger\rangle = \langle RR\rangle = 0$. In thermal equilibrium $\langle b_{\mathbf{q}} b^\dagger_{\mathbf{q}'}\rangle = \delta_{\mathbf{qq}'}(N(\omega_{\mathbf{q}})+1)$ and $\langle b^\dagger_{\mathbf{q}} b_{\mathbf{q}'}\rangle = \delta_{\mathbf{qq}'}N(\omega_{\mathbf{q}})$, where $N(\Lambda) = (\exp(\beta\hbar\Lambda)-1)^{-1}$ ($\beta = (k_B T)^{-1}$) is the Bose–Einstein distribution. So, replacing these relations in eq. (A.12), we obtain:

$$\begin{aligned}\dot{\rho}(t) = & -S(t)\left[\int_0^{+\infty} ds \sum_{\mathbf{q}} |g_{\mathbf{q}}|^2 \left(N(\omega_{\mathbf{q}})e^{i\omega_{\mathbf{q}}s} + \left(N(\omega_{\mathbf{q}})e^{-i\omega_{\mathbf{q}}s}+1\right)\right) S(t-s)\right]\rho(t) \\ & + \left[\int_0^{+\infty} ds \sum_{\mathbf{q}} |g_{\mathbf{q}}|^2 \left(N(\omega_{\mathbf{q}})e^{-i\omega_{\mathbf{q}}s} + \left(N(\omega_{\mathbf{q}})e^{i\omega_{\mathbf{q}}s}+1\right)\right) S(t-s)\right]\rho(t)S(t) + H.c. .\end{aligned} \tag{A.13}$$

To compute the two integrals, $S(t-s)$ is replaced in eq. (A.13) by eq. (A.10)

and the following relation is used

$$\int_0^\infty ds e^{\pm\epsilon s} = \pi\delta(\epsilon) \pm i\frac{\mathcal{P}}{\epsilon}\,, \tag{A.14}$$

where $\mathcal{P}$ is the Cauchy's principal value. The $\mathcal{P}$ does not contribute to dephasing, thus this can be neglected [183]. Furthermore, only the terms $\delta(\omega_{\mathbf{q}} - \Lambda)$ are considered.

$$\dot{\rho}(t) = \frac{\pi}{2}J(\Lambda)\left(N(\Lambda)\left[S(t), \sigma_+ e^{i\Lambda t}\rho(t)\right] + (N(\Lambda)+1)\left[S(t), \sigma_- e^{-i\Lambda t}\rho(t)\right]\right) + H.c.\,, \tag{A.15}$$

where $J(\Lambda)$ is the spectral density function (eq. (A.3)),

$$J(\Lambda) = \frac{1}{\hbar^2}\sum_{\mathbf{q}}|g_{\mathbf{q}}|^2\delta(\omega_{\mathbf{q}} - \Lambda) = \frac{\left(D_e P\left[\psi^e(\mathbf{r})\right] - D_h P\left[\psi^h(\mathbf{r})\right]\right)^2}{4\pi^2\hbar\eta v_s^5}\,. \tag{A.16}$$

To come back to the excitonic basis, the Schrödinger transformation has to be made, where $\dot{\rho}(t) \rightarrow \dot{\rho}(t) + i\left[H_0, \rho(t)\right]/\hbar$, $S(t) \rightarrow (I + \sigma_z)/2$ and $\sigma_\pm e^{\pm i\Lambda t} \rightarrow (-\Omega\sigma_z - \Delta\sigma_x \mp i\Lambda\sigma_y)/4\Lambda^2$. The master equation then becomes

$$\begin{aligned}\dot{\rho}(t) =& -i\frac{\Omega}{2}\left[\sigma_x, \rho(t)\right] - i\frac{\Delta}{2}\left[\sigma_z, \rho(t)\right] - \frac{\Gamma}{2}\left(\sigma_+\sigma_-\rho(t) - 2\sigma_-\rho(t)\sigma_+ + \rho(t)\sigma_+\sigma_-\right)\\ &- \frac{\mathcal{K}(\Lambda)}{4\Lambda^2}\left(\Omega^2\left[\sigma_z, \sigma_z\rho(t)\right] + \Delta\Omega\left[\sigma_z, \sigma_x\rho(t)\right]\right) - i\frac{iJ(\Lambda)\Omega}{4\Lambda}\left[\sigma_z, \sigma_y\rho(t)\right]\\ &+ \frac{\mathcal{K}(\Lambda)}{4\Lambda^2}\left(\Omega^2\left[\sigma_z, \rho(t)\sigma_z\right] + \Delta\Omega\left[\sigma_z, \rho(t)\sigma_x\right]\right) + i\frac{J(\Lambda)\Omega}{4\Lambda}\left[\sigma_z, \rho(t)\sigma_y\right]\,,\end{aligned} \tag{A.17}$$

where $\mathcal{K}(\omega) = \int_0^\infty dt e^{i\omega t}\mathcal{K}(t)$ and $\mathcal{K}(t) = \int_0^\infty d\omega J(\omega)\left(\coth\left(\frac{\hbar\omega}{2k_BT}\right)\cos(\omega t) - i\sin(\omega t)\right)$. Assuming wave functions given by the ground-state solution of a harmonic potential $P\left[\Psi^{e,h}(\omega)\right] = \exp\left(-\omega^2 a_{e,h}^2/4\right)$, and $\sum_{\mathbf{q}} \rightarrow \frac{V}{(2\pi)^3}\int d^3\mathbf{q}$, the spectra density function becomes [62]:

$$J(\omega) = \frac{\omega^3}{4\pi^2\eta\hbar v_s^5}\left\{D_e\exp\left(-\frac{\omega^2 a_c^2}{4v_s^2}\right) - D_h\exp\left(-\frac{\omega^2 a_h^2}{4v_s^2}\right)\right\}^2\,, \tag{A.18}$$

where $a_e + 4.5$ nm and $a_h = 1.8$ nm are the electron and hole confinement lengths, the deformation potential constants are $D_e = 7$ eV and $D_h = -3.5$ eV, $\eta = 5370$ kg/m^3 and $v_s = 5110$ m/s. These material parameters for GaAs are given in [146]. The exciton lifetime (Γ) is also included in the master equation eq. (A.17).

A.2 CW excitation

Although CW excitation was not considered extensively in this thesis, it is an interesting theoretical case, since it makes the simulations much easier. The emission spectrum into a reservoir is the main goal. For the CW case, this can be analytically obtained. The intensity is given by

$$I(\nu) \propto -Re\left[\int_0^\infty dt e^{i\nu t}\langle\sigma_+(t)\sigma_-(0)\rangle\right] = Re\left[\int_0^\infty dt e^{i\nu t}\mathrm{Tr}\left[\sigma_+\rho(t)\sigma_-\right]\right] . \quad \text{(A.19)}$$

The last integral has included the Quantum regression theorem [183]. In the CW case the master equation (eq. (A.17)) can be reduced to $\dot{\rho(t)} = \mathbf{M}.\rho(t)$ where $\rho = \{\rho_{11}, \rho_{12}, \rho_{21}, \rho_{22}\}$ and $\mathbf{M}$ is a linear super operator. This can be easily solved by Laplace transformation:

$$\mathbf{M}\rho(s) - s\rho(s) = \sigma_-\rho(0) . \quad \text{(A.20)}$$

Solving eq. (A.20) in orders of $\rho(s)$ and replacing it in eq. (A.19), the

following expression for the intensity spectrum is obtained [184]:

$$I(\nu) \propto -2Re\left\{ \begin{bmatrix} 0 & 0 & 1 & 0 \end{bmatrix} [\mathbf{M} + i\nu]^{-1} \begin{bmatrix} 0 \\ 0 \\ \rho_{11}(0) \\ \rho_{12}(0) \end{bmatrix} \right\}, \tag{A.21}$$

where $\rho(0)$ is the solution for the stationary case $\mathbf{M}.\rho = 0$ and $\mathbf{M}$ is

$$\begin{bmatrix} 0 & i\Omega & i\Omega & \Gamma \\ \frac{\Delta\Omega\mathcal{K}(\Lambda)}{2\Lambda^2} - i\Omega & -\frac{\Gamma}{2} - \frac{\Omega^2\mathcal{K}(\Lambda)}{\Lambda^2} - i\Delta & 0 & -\frac{\Delta\Omega\mathcal{K}(\Lambda)}{2\Lambda^2} - \frac{\Omega J(\Lambda)}{2\Lambda} - i\Omega \\ \frac{\Delta\Omega\mathcal{K}(\Lambda)}{2\Lambda^2} - \frac{\Omega J(\Lambda)}{2\Lambda} + i\Omega & 0 & -\frac{\Gamma}{2} + \frac{\Omega^2\mathcal{K}(\Lambda)}{\Lambda^2} - i\Delta & -\frac{\Delta\Omega\mathcal{K}(\Lambda)}{2\Lambda^2} - i\Omega \\ 0 & i\Omega & -i\Omega & -\Gamma \end{bmatrix} \tag{A.22}$$

Computing eq. (A.21) the resonance fluorescence spectrum for CW excitation is obtained. Figure A.1 shows the simulated RF spectra for different cases: QD resonant with the cavity (green and orange line) and positive and negative detuned relative to the cavity (blue and red line, respectively). It is interesting to see the influence of the phonon bath on the Mollow triplet (orange line). Both the cavity or phonon bath affect strongly the Mollow triplet emission as is shown in fig. A.1. For a QD resonant with the cavity (orange line), the asymmetry of Mollow side peaks is due to the phonon-induced effect. In the absence of a phonon bath, the asymmetry is due to the cavity coupling effects as shown in the bottom graph of fig. A.1 [185].

The simulated results presented in fig. A.1 are consistent with the results presented in [151]. Their master equation has the cavity terms explicitly, so the simulated spectra shows the cavity mode as well. Here, eq. (A.17) takes into account the cavity by the "bad cavity" limit.

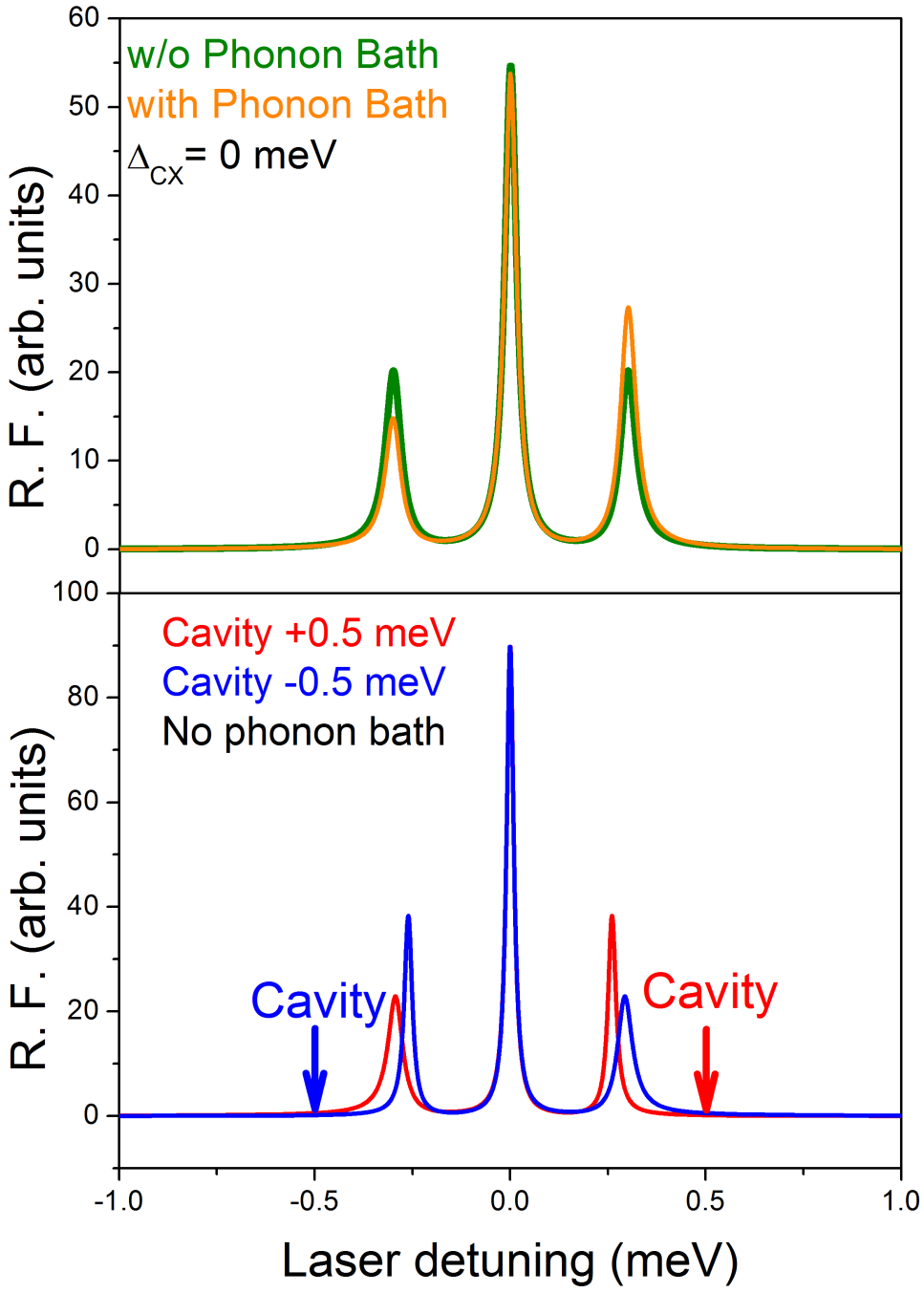

Figure A.1: Simulated Mollow triplet spectra (eq. (A.21)). Mollow triplet spectra for QD resonant with cavity, $\Delta_{CX} = 0$, (top graph) with (orange line) and without (green line) the exciton–phonon interaction. In the bottom graph the Mollow triplet spectra for a cavity detuned +0.5 meV (blue line) and −0.5 meV (red line) relative to the QD without exciton–phonon interaction is shown. The arrows indicate the spectral position of the cavity relative to the QD.

A.3 Pulsed laser excitation

Knowing $\langle \dot{A} \rangle = \dot{\rho} A$, where A is a quantum operator and $\dot{\rho}$ is given by the master equation eq. (A.17), the equations of motion are obtained:

$$\dot{\sigma_x} = \Delta\sigma_y - \left(\frac{\Omega^2 Re[K(\Lambda)]}{\Lambda^2} + \frac{\Gamma}{2}\right)\sigma_x - \frac{\Delta\Omega Re[K(\Lambda)]}{\Lambda^2}\sigma_z - \frac{\pi\Omega J(\Lambda)}{2\Lambda}\,, \quad \text{(A.23a)}$$

$$\dot{\sigma_y} = \Omega\sigma_z - \Delta\sigma_x - \left(\frac{\Omega^2 Re[K(\Lambda)]}{\Lambda^2} + \frac{\Gamma}{2}\right)\sigma_y\,, \quad \text{(A.23b)}$$

$$\dot{\sigma_z} = -\Omega\sigma_y - \Gamma\left(\sigma_z + 1\right)\,. \quad \text{(A.23c)}$$

From eq. (A.23) the causes of dephasing are identified (see section 2.6.1). The term in Γ is the responsible for longitudinal dephasing (T_1), whist either Γ and the phonon bath ($Re[K(\Lambda)]$) contribute to transverse dephasing (T_2).

To test the model in eq. (A.23), the exciton population C_X ($C_X = (\sigma_z + 1)/2$) was computed using the parameters presented in [59]. Figure A.2 compares the result obtained experimentally by [59] and the result computed by eq. (A.23). The agreement between both results is very good. This validates this model.

This model has been widely used to support the results presented in chapter 5. The simulations obtained from this model help to interpret the results, with excellent agreements found between the experimental data and the theoretical model.

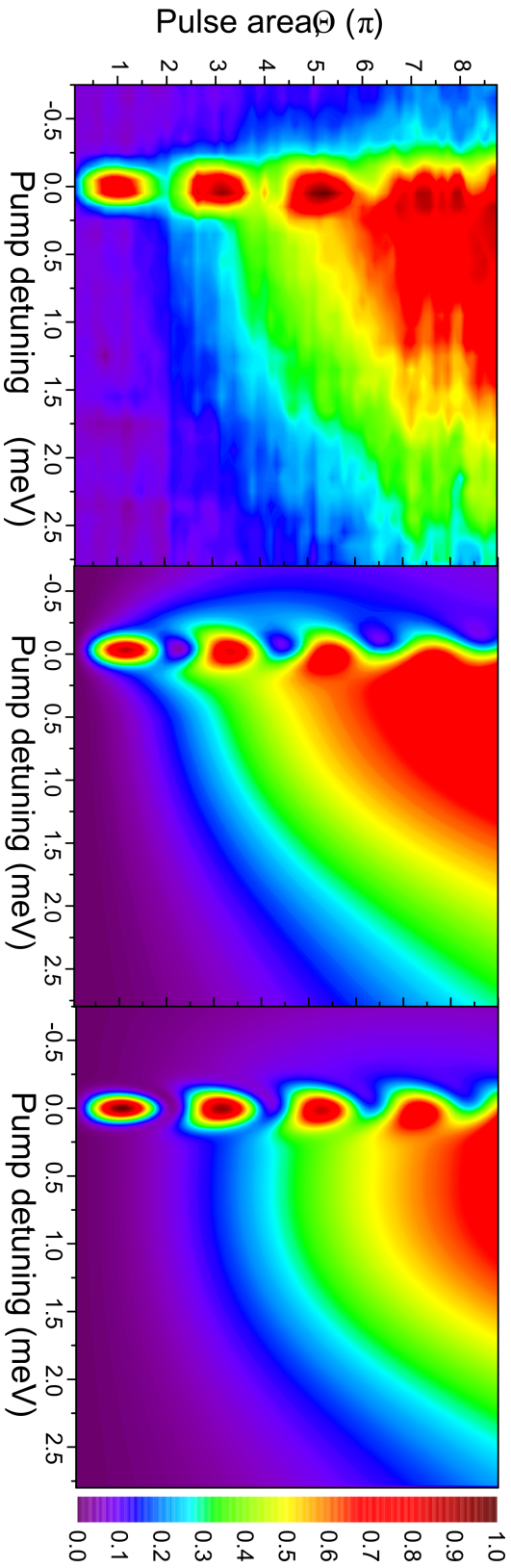

Figure A.2: C_X as a function of pulse area Ω and laser detuning $\hbar\Delta$ obtained experimentally (top graph), by solving eq. (A.23) (middle graph) and, by Path-integral simulation (performed by A. M. Barth of Institut für Theoretische Physik III, Universität Bayreuth) with permission of [59].

Appendix B

Deconvolution of Time Resolved Data

In the exciton time dynamics measurements presented in section 4.3, the QD RF signal is affected by the finite laser pulse–width (two pulse resonance fluorescence technique section 4.2) or by the instrument function response (*i.e* detector response time) in the time resolved PL (TRPL). Therefore, the signal detected is the convolution of the exciton dynamics and the laser/APD modulation function. To accurately extract the exciton lifetime, the deconvolution of the data is computed. Deconvolution is a mathematical tool which restores the individual signals.

B.1 Time Resolved PL (TRPL)

Figure B.1 shows the exciton TRPL lifetime data (black circles) of a QD uncoupled with the cavity, measured using a APD. The blue line is the response instrument of the APD. The response time of the detector, for this data, was

≈ 400 ps. The red line is the convolution curve obtained from the function:

$$f(x) = y_0 + \frac{A}{\tau} e^{\frac{1}{2}\frac{\tau_0^2}{\tau^2} - \frac{x-x_c}{\tau}} \int_{-\infty}^{z} \frac{1}{\sqrt{2\pi}} e^{-\frac{y^2}{2}} dy \,, \tag{B.1}$$

where $z = \frac{x-x_c}{\tau_0} - \frac{\omega}{\tau}$. Equation (B.1) is the convolution function $(g(x) * h(x))$ of a Gaussian $(g(x))$, which describes the detector response and an exponential function $(h(x))$, which models the emission of the dot. The instrumental and signal functions are thus given by:

$$g(x) = \frac{1}{\sqrt{2\pi}\omega} e^{-\frac{(x-x_c)^2}{2\omega^2}} \tag{B.2a}$$

$$h(x) = \frac{A}{\tau} e^{-\frac{x}{\tau}} \,, \tag{B.2b}$$

where ω and x_c are, respectively the width of and the central position of the Gaussian function and τ is the characteristic time decay of the exponential function, which corresponds to the exciton lifetime. Thus, by fitting eq. (B.1) the exciton life time can be obtained. The deconvolution of the TRPL data was used to obtained the average exciton lifetime of uncoupled QDs in bulk. This data is presented in fig. 4.4. The exciton life time obtained fitting a single exponential would be 1.19 ns instead 0.94 ns obtained from the deconvolution.

B.2 Time Resolved RF (TRRF)

The deconvolution of the data obtained from Two Pulse Resonance Fluorescence technique (TPRF) is more complicated. Whilst the SPAD detector collecting the photons is triggered by the laser, therefore, only positive delay times between the laser and the PL signal are measured, the TPRF technique is triggered by the first pulse and both pulses have a pulse area of π. Thus, the RF is measured either for positive or negative delay times. This is the reason why the data is

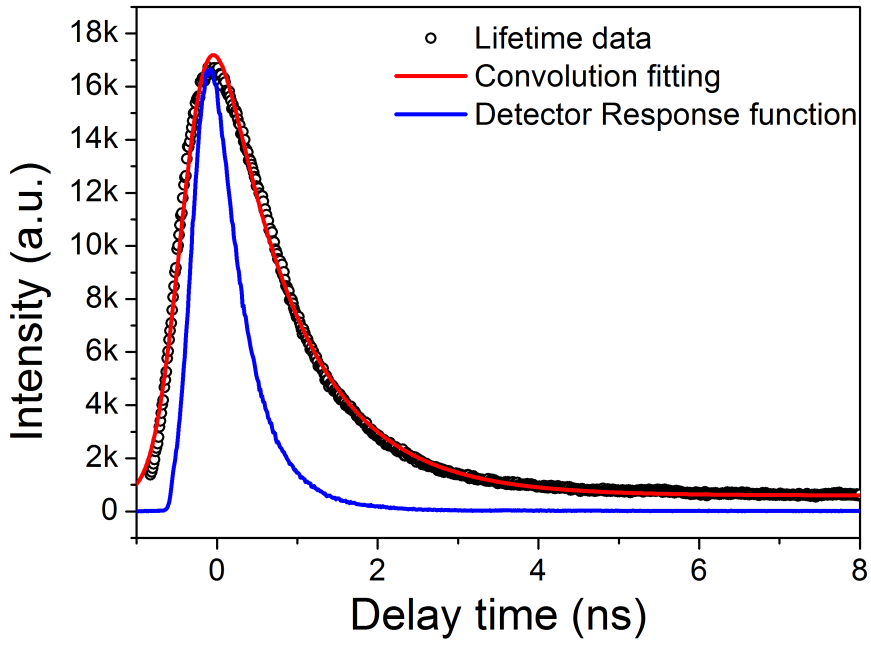

Figure B.1: Exciton lifetime data measured from an APD (black circles). The convolution fitting and the response function are respectively the red and the blue line.

symmetrical. So, to fit the data obtained from the TPRF technique, a new fitting function was used

$$f_{TPRF}(x) = f(x) + f(-x)\,, \tag{B.3}$$

where $f(x)$ is the convolution function given by eq. (B.1). Thus, the symmetry of the data is taken into account as shown in fig. B.2. The fitting agrees well with the data and an exciton lifetime of $\tau = 22.5 \pm 0.9$ ps was obtained when the QD was resonant with the cavity. This is the shortest exciton lifetime observed in InGaAs QDs. In this case the instrument response corresponds to the laser pulse–width. As the two pulses had different pulse–widths, the instrument response was in this case $\tau_0 = \sqrt{FMHW^2_{\text{pulse1}} + FMHW^2_{\text{pulse2}}} \approx 16$ ps. This deconvolution technique was used to obtain the exciton lifetime of the QD coupled with the cavity. This data is displayed in fig. 4.6.

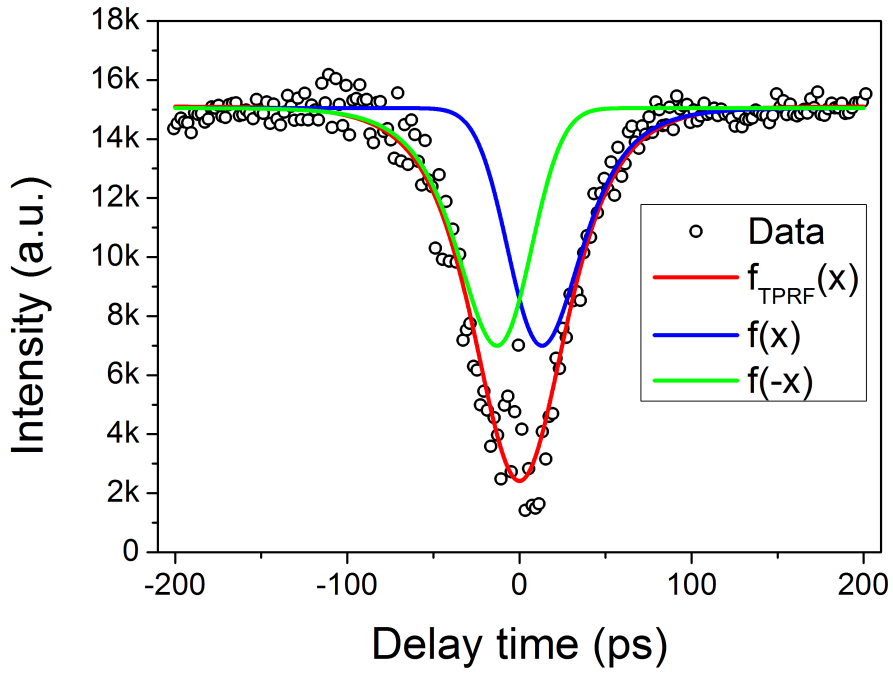

Figure B.2: Exciton lifetime data measured from an TPFR technique (black circles). The $f(x)$ and $f(-x)$ are respectively the blue and the green line. The red line is the $f_{TPRF}(x) = f(x) - f(-x)$.

Bibliography

[1] G. E. Moore. Cramming more components onto integrated circuits, reprinted from electronics, volume 38, number 8, april 19, 1965, pp.114 ff. *IEEE Solid-State Circuits Society Newsletter*, 11(5):33–35, Sept 2006.

[2] Richard P. Feynman. Simulating physics with computers. *International Journal of Theoretical Physics*, 21(6):467–488, 1982.

[3] D. Deutsch. Quantum theory, the church-turing principle and the universal quantum computer. *Proceedings of the Royal Society of London A: Mathematical, Physical and Engineering Sciences*, 400(1818):97–117, 1985.

[4] Peter W. Shor. Polynomial-time algorithms for prime factorization and discrete logarithms on a quantum computer. *SIAM J. Comput.*, 26(5):1484–1509, October 1997.

[5] David P. DiVincenzo. The physical implementation of quantum computation. *Fortschritte der Physik*, 48(9-11):771–783, 9 2000.

[6] E. Knill, R. Laflamme, and G. J. Milburn. A scheme for efficient quantum computation with linear optics. *Nature*, 409(6816):46–52, Jan 2001.

[7] Gavin K. Brennen, Carlton M. Caves, Poul S. Jessen, and Ivan H. Deutsch. Quantum logic gates in optical lattices. *Phys. Rev. Lett.*, 82:1060–1063, Feb 1999.

[8] D. Jaksch, H. J. Briegel, J. I. Cirac, C. W. Gardiner, and P. Zoller. Entanglement of atoms via cold controlled collisions. *Phys. Rev. Lett.*, 82:1975–1978, Mar 1999.

[9] C. Monroe, D. M. Meekhof, B. E. King, W. M. Itano, and D. J. Wineland. Demonstration of a fundamental quantum logic gate. *Phys. Rev. Lett.*, 75:4714–4717, Dec 1995.

[10] F. Jelezko, T. Gaebel, I. Popa, A. Gruber, and J. Wrachtrup. Observation of coherent oscillations in a single electron spin. *Phys. Rev. Lett.*, 92:076401, Feb 2004.

[11] R. Vrijen, E. Yablonovitch, K. Wang, H. W. Jiang, A. Balandin, V. Roychowdhury, T. Mor, and D. DiVincenzo. Electron-spin-resonance transistors for quantum computing in silicon-germanium heterostructures. *Phys. Rev. A*, 62:012306, Jun 2000.

[12] B. E. Kane. A silicon-based nuclear spin quantum computer. *Nature*, 393(6681):133–137, May 1998.

[13] L. M. K. Vandersypen and I. L. Chuang. NMR techniques for quantum control and computation. *Rev. Mod. Phys.*, 76:1037–1069, Jan 2005.

[14] D.V. Averin. Adiabatic quantum computation with cooper pairs. *Solid State Communications*, 105(10):659 – 664, 1998.

[15] A. Shnirman, G. Schön, and Z. Hermon. Quantum manipulations of small josephson junctions. *Phys. Rev. Lett.*, 79:2371–2374, Sep 1997.

[16] J. E. Mooij, T. P. Orlando, L. Levitov, Lin Tian, Caspar H. van der Wal, and Seth Lloyd. Josephson persistent-current qubit. *Science*, 285(5430):1036–1039, 1999.

[17] S. Fafard, H. C. Liu, Z. R. Wasilewski, J. P. McCaffrey, M. Spanner, S. Raymond, C. N. Allen, K. Hinzer, J. Lapointe, C. Struby, M. Gao, P. Hawrylak, C. Gould, A. Sachrajda, and P. Zawadzki. Quantum dot devices. *Proc. SPIE*, 4078:100–114, 2000.

[18] A. Zrenner, L. V. Butov, M. Hagn, G. Abstreiter, G. Böhm, and G. Weimann. Quantum dots formed by interface fluctuations in AlAs/GaAs coupled quantum well structures. *Phys. Rev. Lett.*, 72:3382–3385, May 1994.

[19] G. H. Carey, A. L. Abdelhady, Z. Ning, S. M. Thon, O. M. Bakr, and E. H. Sargent. Colloidal quantum dot solar cells. *Chemical Reviews*, 115(23):12732–12763, 2015.

[20] R. Hanson, L. P. Kouwenhoven, J. R. Petta, S. Tarucha, and L. M. K. Vandersypen. Spins in few-electron quantum dots. *Rev. Mod. Phys.*, 79:1217–1265, Oct 2007.

[21] T. Ishikawa, S. Kohmoto, and K. Asakawa. Site control of self-organized inas dots on GaAs substrates by in situ electron-beam lithography and molecular-beam epitaxy. *Applied Physics Letters*, 73(12):1712–1714, 1998.

[22] M. H. Baier, S. Watanabe, E. Pelucchi, and E. Kapon. High uniformity of site-controlled pyramidal quantum dots grown on prepatterned substrates. *Applied Physics Letters*, 84(11):1943–1945, 2004.

[23] K. H. Lee, A. M. Green, R. A. Taylor, D. N. Sharp, J. Scrimgeour, O. M. Roche, J. H. Na, A. F. Jarjour, A. J. Turberfield, F. S. F. Brossard, D. A. Williams, and G. A. D. Briggs. Registration of single quantum dots using cryogenic laser photolithography. *Applied Physics Letters*, 88(19):3106, 2006.

[24] D. Bimberg, M. Grundmann, and N.N. Ledentsov. *Quantum Dot Heterostructures*. Wiley, 1999.

[25] D J Mowbray and M S Skolnick. New physics and devices based on self-assembled semiconductor quantum dots. *Journal of Physics D: Applied Physics*, 38(13):2059, 2005.

[26] D. M. Bruls, J. W. A. M. Vugs, P. M. Koenraad, H. W. M. Salemink, J. H. Wolter, M. Hopkinson, M. S. Skolnick, F. Long, and S. P. A. Gill. Determination of the shape and indium distribution of low-growth-rate inas quantum dots by cross-sectional scanning tunneling microscopy. *Applied Physics Letters*, 81(9):1708–1710, 2002.

[27] M. Fox. *Optical Properties of Solids*. Oxford Master Series in Physics. OUP Oxford, 2010.

[28] L. Jacak, P. Hawrylak, and A. Wójs. *Quantum dots*. NanoScience and Technology Series. Springer, 1998.

[29] P. Michler. *Single Quantum Dots: Fundamentals, Applications and New Concepts*. Physics and Astronomy Online Library. Springer, 2003.

[30] A. Wojs, P. Hawrylak, S. Fafard, and L. Jacak. Electronic structure and magneto-optics of self-assembled quantum dots. *Phys. Rev. B*, 54:5604–5608, Aug 1996.

[31] A. Wojs and P. Hawrylak. Theory of photoluminescence from modulation-doped self-assembled quantum dots in a magnetic field. *Phys. Rev. B*, 55:13066–13071, May 1997.

[32] M. Bayer, A. Kuther, A. Forchel, A. Gorbunov, V. B. Timofeev, F. Schäfer, J. P. Reithmaier, T. L. Reinecke, and S. N. Walck. Electron and hole g factors and exchange interaction from studies of the exciton fine structure in $In_{0.60}Ga_{0.40}As$ quantum dots. *Phys. Rev. Lett.*, 82:1748–1751, Feb 1999.

[33] M. Bayer, G. Ortner, O. Stern, A. Kuther, A. A. Gorbunov, A. Forchel, P. Hawrylak, S. Fafard, K. Hinzer, T. L. Reinecke, S. N. Walck, J. P.

Reithmaier, F. Klopf, and F. Schäfer. Fine structure of neutral and charged excitons in self-assembled In(Ga)As/(Al)GaAs quantum dots. *Phys. Rev. B*, 65:195315, May 2002.

[34] R. J. Young, R. M. Stevenson, A. J. Shields, P. Atkinson, K. Cooper, D. A. Ritchie, K. M. Groom, A. I. Tartakovskii, and M. S. Skolnick. Inversion of exciton level splitting in quantum dots. *Phys. Rev. B*, 72:113305, Sep 2005.

[35] M. Bayer, O. Stern, A. Kuther, and A. Forchel. Spectroscopic study of dark excitons in $In_xGa_{1-x}As$ self-assembled quantum dots by a magnetic-field-induced symmetry breaking. *Phys. Rev. B*, 61:7273–7276, Mar 2000.

[36] J. Zhang, E. Zallo, B. Höfer, Y. Chen, R. Keil, M. Zopf, S. Böttner, F. Ding, and O. G. Schmidt. Electric-field-induced energy tuning of on-demand entangled-photon emission from self-assembled quantum dots. *Nano Letters*, 17(1):501–507, 2017.

[37] P. W. Fry, J. J. Finley, L. R. Wilson, A. Lematre, D. J. Mowbray, M. S. Skolnick, M. Hopkinson, G. Hill, and J. C. Clark. Electric-field-dependent carrier capture and escape in self-assembled InAs/GaAs quantum dots. *Applied Physics Letters*, 77(26):4344–4346, 2000.

[38] J. J. Finley, M. Sabathil, P. Vogl, G. Abstreiter, R. Oulton, A. I. Tartakovskii, D. J. Mowbray, M. S. Skolnick, S. L. Liew, A. G. Cullis, and M. Hopkinson. Quantum-confined stark shifts of charged exciton complexes in quantum dots. *Phys. Rev. B*, 70:201308, Nov 2004.

[39] A. V. Kuhlmann, J. Houel, A. Ludwig, L. Greuter, D. Reuter, A. D. Wieck, M. Poggio, and R. J. Warburton. Charge noise and spin noise in a semiconductor quantum device. *Nat Phys*, 9(9):570–575, Sep 2013.

[40] J. Houel, A. V. Kuhlmann, L. Greuter, F. Xue, M. Poggio, B. D. Gerardot, P. A. Dalgarno, A. Badolato, P. M. Petroff, A. Ludwig, D. Reuter,

A. D. Wieck, and R. J. Warburton. Probing single-charge fluctuations at a GaAs/AlAs interface using laser spectroscopy on a nearby ingaas quantum dot. *Phys. Rev. Lett.*, 108:107401, Mar 2012.

[41] P.-L. Ardelt, T. Simmet, K. Müller, C. Dory, K. A. Fischer, A. Bechtold, A. Kleinkauf, H. Riedl, and J. J. Finley. Controlled tunneling-induced dephasing of rabi rotations for high-fidelity hole spin initialization. *Phys. Rev. B*, 92:115306, Sep 2015.

[42] A. J. Brash, L. M. P. P. Martins, F. Liu, J. H. Quilter, A. J. Ramsay, M. S. Skolnick, and A. M. Fox. High-fidelity initialization of long-lived quantum dot hole spin qubits by reduced fine-structure splitting. *Phys. Rev. B*, 92:121301, Sep 2015.

[43] W. Langbein, P. Borri, U. Woggon, V. Stavarache, D. Reuter, and A. D. Wieck. Radiatively limited dephasing in InAs quantum dots. *Phys. Rev. B*, 70:033301, Jul 2004.

[44] P. A. Dalgarno, J. M. Smith, J. McFarlane, B. D. Gerardot, K. Karrai, Antonio Badolato, P. M. Petroff, and R. J. Warburton. Coulomb interactions in single charged self-assembled quantum dots: Radiative lifetime and recombination energy. *Phys. Rev. B*, 77:245311, Jun 2008.

[45] T. M. Godden, J. H. Quilter, A. J. Ramsay, Yanwen Wu, P. Brereton, S. J. Boyle, I. J. Luxmoore, J. Puebla-Nunez, A. M. Fox, and M. S. Skolnick. Coherent optical control of the spin of a single hole in an InAs/GaAs quantum dot. *Phys. Rev. Lett.*, 108:017402, Jan 2012.

[46] J. R. Petta, A. C. Johnson, J. M. Taylor, E. A. Laird, A. Yacoby, M. D. Lukin, C. M. Marcus, M. P. Hanson, and A. C. Gossard. Coherent manipulation of coupled electron spins in semiconductor quantum dots. *Science*, 309(5744):2180–2184, 2005.

[47] A. J. Ramsay, Achanta Venu Gopal, E. M. Gauger, A. Nazir, B. W. Lovett, A. M. Fox, and M. S. Skolnick. Damping of exciton rabi rotations by acoustic phonons in optically excited InGaAs/GaAs quantum dots. *Phys. Rev. Lett.*, 104:017402, Jan 2010.

[48] A. J. Ramsay, T. M. Godden, S. J. Boyle, E. M. Gauger, A. Nazir, B. W. Lovett, A. M. Fox, and M. S. Skolnick. Phonon-induced rabi-frequency renormalization of optically driven single InGaAs/GaAs quantum dots. *Phys. Rev. Lett.*, 105:177402, Oct 2010.

[49] A. Greilich, S. G. Carter, D. Kim, A. S. Bracker, and D. Gammon. Optical control of one and two hole spins in interacting quantum dots. *Nat Photon*, 5(11):702–708, Nov 2011.

[50] A. Abragam. *The principles of nuclear magnetism.* International series of monographs on physics. Clarendon Press, 1983.

[51] J. Fischer, W. A. Coish, D. V. Bulaev, and D. Loss. Spin decoherence of a heavy hole coupled to nuclear spins in a quantum dot. *Phys. Rev. B*, 78:155329, Oct 2008.

[52] J. Puebla, E. A. Chekhovich, M. Hopkinson, P. Senellart, A. Lemaitre, M. S. Skolnick, and A. I. Tartakovskii. Dynamic nuclear polarization in InGaAs/GaAs and GaAs/AlGaAs quantum dots under nonresonant ultralow-power optical excitation. *Phys. Rev. B*, 88:045306, Jul 2013.

[53] E. A. Chekhovich, M. M. Glazov, A. B. Krysa, M. Hopkinson, P. Senellart, A. Lemaitre, M. S. Skolnick, and A. I. Tartakovskii. Element-sensitive measurement of the hole-nuclear spin interaction in quantum dots. *Nat Phys*, 9(2):74–78, February 2013.

[54] E. A. Chekhovich, A. B. Krysa, M. S. Skolnick, and A. I. Tartakovskii. Direct measurement of the hole-nuclear spin interaction in single InP/GaInP

quantum dots using photoluminescence spectroscopy. *Phys. Rev. Lett.*, 106:027402, Jan 2011.

[55] A. Högele, S. Seidl, M. Kroner, K. Karrai, R. J. Warburton, B. D. Gerardot, and P. M. Petroff. Voltage-controlled optics of a quantum dot. *Phys. Rev. Lett.*, 93:217401, Nov 2004.

[56] E. Stock, M-R. Dachner, T. Warming, A. Schliwa, A. Lochmann, A. Hoffmann, A. I. Toropov, A. K. Bakarov, I. A. Derebezov, M. Richter, V. A. Haisler, A. Knorr, and D. Bimberg. Acoustic and optical phonon scattering in a single In(Ga)As quantum dot. *Phys. Rev. B*, 83:041304, Jan 2011.

[57] S. Werner, P. Zimmer, A. Strittmatter, and A. Hoffmann. Phonon interaction in InGaAs/GaAs quantum dots. *MRS Proceedings*, 1053, 2007.

[58] E. A. Muljarov and R. Zimmermann. Exciton dephasing in quantum dots due to lo-phonon coupling: An exactly solvable model. *Phys. Rev. Lett.*, 98:187401, May 2007.

[59] H. Quilter, J. J. Brash, A. F. Liu, M. Glässl, M. Barth, A. M. Axt, V. J. Ramsay, A. S. Skolnick, M. and M. Fox, A.˙Phonon-assisted population inversion of a single InGaAs/GaAs quantum dot by pulsed laser excitation. *Phys. Rev. Lett.*, 114:137401, Mar 2015.

[60] F. Liu, L. M. P. Martins, A. J. Brash, A. M. Barth, J. H. Quilter, V. M. Axt, M. S. Skolnick, and A. M. Fox. Ultrafast depopulation of a quantum dot by la-phonon-assisted stimulated emission. *Phys. Rev. B*, 93:161407, Apr 2016.

[61] A. J. Brash, L. M. P. P. Martins, A. M. Barth, F. Liu, J. H. Quilter, M. Glässl, V. M. Axt, A. J. Ramsay, M. S. Skolnick, and A. M. Fox. Dynamic vibronic coupling in InGaAs quantum dots [invited]. *J. Opt. Soc. Am. B*, 33(7):C115–C122, Jul 2016.

[62] A. Vagov, M. D. Croitoru, M. Glässl, V. M. Axt, and T. Kuhn. Real-time path integrals for quantum dots: Quantum dissipative dynamics with superohmic environment coupling. *Phys. Rev. B*, 83:094303, Mar 2011.

[63] H. Kim, R. Bose, T. C. Shen, G. S. Solomon, and E. Waks. A quantum logic gate between a solid-state quantum bit and a photon. *Nat Photon*, 7(5):373–377, May 2013.

[64] A. Faraon, A. Majumdar, H. Kim, P. Petroff, and J. Vučković. Fast electrical control of a quantum dot strongly coupled to a photonic-crystal cavity. *Phys. Rev. Lett.*, 104:047402, Jan 2010.

[65] D. Englund, A. Faraon, A. Majumdar, N. Stoltz, P. Petroff, and J. Vučković. An optical modulator based on a single strongly coupled quantum dot - cavity system in a p-i-n junction. *Opt. Express*, 17(21):18651–18658, Oct 2009.

[66] T. Volz, A. Reinhard, M. Winger, A. Badolato, K. J. Hennessy, E. L. Hu, and A. Imamoglu. Ultrafast all-optical switching by single photons. *Nat Photon*, 6(9):605–609, Sep 2012.

[67] R. Bose, D. Sridharan, H. Kim, G.nn S. Solomon, and E. Waks. Low-photon-number optical switching with a single quantum dot coupled to a photonic crystal cavity. *Phys. Rev. Lett.*, 108:227402, May 2012.

[68] D. Englund, A. Majumdar, M. Bajcsy, A. Faraon, P. Petroff, and J. Vučković. Ultrafast photon-photon interaction in a strongly coupled quantum dot-cavity system. *Phys. Rev. Lett.*, 108:093604, Mar 2012.

[69] X. Ding, Y. He, Z.-C. Duan, N. Gregersen, M.-C. Chen, S. Unsleber, S. Maier, C. Schneider, M. Kamp, S. Höfling, C.-Y. Lu, and J.-W. Pan. On-demand single photons with high extraction efficiency and near-unity

indistinguishability from a resonantly driven quantum dot in a micropillar. *Phys. Rev. Lett.*, 116:020401, Jan 2016.

[70] N. Somaschi, V. Giesz, L. De Santis, Almeida M. P.and Hornecker G. Loredo, J. C. and., L. S. Portalupi, T. Grange, C. Antón, J. Demory, C. Gómez, I. Sagnes, N. D. Lanzillotti-Kimura, A. Lemaítre, A. Auffeves, A. G. White, L. Lanco, and P. Senellart. Near-optimal single-photon sources in the solid state. *Nat Photon*, 10(5):340–345, May 2016.

[71] Y. Arakawa, S. Iwamoto, M. Nomura, A. Tandaechanurat, and Y. Ota. Cavity quantum electrodynamics and lasing oscillation in single quantum dot-photonic crystal nanocavity coupled systems. *IEEE Journal of Selected Topics in Quantum Electronics*, 18(6):1818–1829, Nov 2012.

[72] S. M. Thon, M. T. Rakher, H. Kim, J. Gudat, W. T. M. Irvine, P. M. Petroff, and D. Bouwmeester. Strong coupling through optical positioning of a quantum dot in a photonic crystal cavity. *Applied Physics Letters*, 94(11):1115, 2009.

[73] Proceedings of the american physical society. *Physical Review*, 69(11-12):674–674, 1946.

[74] T. D. Happ, I. I. Tartakovskii, V. D. Kulakovskii, J.-P. Reithmaier, M. Kamp, and A. Forchel. Enhanced light emission of $In_xGa_{1-x}As$ quantum dots in a two-dimensional photonic-crystal defect microcavity. *Phys. Rev. B*, 66:041303, Jul 2002.

[75] A. Badolato, K. Hennessy, M. Atatüre, E. Hu, P. M. Petroff, and A. Imamoğlu. Deterministic coupling of single quantum dots to single nanocavity modes. *Science*, 308(5725):1158–1161, 2005.

[76] S. Laurent, S. Varoutsis, L. Le Gratiet, A. Lematre, I. Sagnes, F. Raineri, A. Levenson, I. Robert-Philip, and I. Abram. Indistinguishable single pho-

tons from a single-quantum dot in a two-dimensional photonic crystal cavity. *Applied Physics Letters*, 87(16):163107, 2005.

[77] G. Khitrova, H. M. Gibbs, M. Kira, S. W. Koch, and A. Scherer. Vacuum rabi splitting in semiconductors. *Nat Phys*, 2(2):81–90, Feb 2006.

[78] K. J. Vahala. Optical microcavities. *Nature*, 424(6950):839–846, Aug 2003.

[79] L. C. Andreani, G. Panzarini, and J. M. Gérard. Strong-coupling regime for quantum boxes in pillar microcavities: Theory. *Phys. Rev. B*, 60:13276–13279, Nov 1999.

[80] E.T. Jaynes and F.W. Cummings. Comparison of quantum and semiclassical radiation theories with application to the beam maser. *Proceedings of the IEEE*, 51(1):89–109, Jan 1963.

[81] Michael Tavis and Frederick W. Cummings. Exact solution for an $\boldsymbol{n}$–molecule radiation–field hamiltonian. *Physical Review*, 170(2):379–384, 1968.

[82] J. D. Joannopoulos, Pierre R. Villeneuve, and S. Fan. Photonic crystals: putting a new twist on light. *Nature*, 386(6621):143–149, Mar 1997.

[83] A. C. T. Thijssen, M. J. Cryan, J. G. Rarity, and R. Oulton. Transfer of arbitrary quantum emitter states to near-field photon superpositions in nanocavities. *Opt. Express*, 20(20):22412–22428, Sep 2012.

[84] R. J. Coles, N. Prtljaga, B. Royall, I. J. Luxmoore, A. M. Fox, and M. S. Skolnick. Waveguide-coupled photonic crystal cavity for quantum dot spin readout. *Opt. Express*, 22(3):2376–2385, Feb 2014.

[85] C. Bentham, I. E. Itskevich, R. J. Coles, B. Royall, E. Clarke, J. O'Hara, N. Prtljaga, A. M. Fox, M. S. Skolnick, and L. R. Wilson.

On-chip electrically controlled routing of photons from a single quantum dot. *Applied Physics Letters*, 106(22), 2015.

[86] M. Shirane, S. Kono, J. Ushida, S. Ohkouchi, N. Ikeda, Y. Sugimoto, and A. Tomita. Mode identification of high-quality-factor single-defect nanocavities in quantum dot-embedded photonic crystals. *Journal of Applied Physics*, 101(7):073107, 2007.

[87] R. S. Kolodka, A. J. Ramsay, J. Skiba-Szymanska, P. W. Fry, H. Y. Liu, A. M. Fox, and M. S. Skolnick. Inversion recovery of single quantum-dot exciton based qubit. *Phys. Rev. B*, 75:193306, May 2007.

[88] A F A Khatab, A J Ramsay, S J Boyle, A M Fox, and M S Skolnick. Inversion recovery measurements of exciton fine-structure beats in a single quantum dot. *Journal of Physics: Conference Series*, 245(1):012010, 2010.

[89] A. Patanè, R. J. A. Hill, L. Eaves, P. C. Main, M. Henini, M. L. Zambrano, A. Levin, N. Mori, C. Hamaguchi, Yu. V. Dubrovskii, E. E. Vdovin, D. G. Austing, S. Tarucha, and G. Hill. Probing the quantum states of self-assembled inas dots by magnetotunneling spectroscopy. *Phys. Rev. B*, 65:165308, Apr 2002.

[90] R. J. Coles, D. M. Price, B. Royall, E. Clarke, M. S. Skolnick, A. M. Fox, and M. N. Makhonin. Path-dependent initialization of a single quantum dot exciton spin in a nanophotonic waveguide. *Phys. Rev. B*, 95:121401, Mar 2017.

[91] W. J. Silverstone, D. Bonneau, K. Ohira, N. Suzuki, H. Yoshida, N. Iizuka, M. Ezaki, M. C. Natarajan, G. M. Tanner, H. R. Hadfield, V. Zwiller, D. G. Marshall, J. G. Rarity, L. J. O'Brien, and M. G. Thompson. On-chip quantum interference between silicon photon-pair sources. *Nat Photon*, 8(2):104–108, Feb 2014.

[92] P. Lodahl, S. Mahmoodian, and S. Stobbe. Interfacing single photons and single quantum dots with photonic nanostructures. *Rev. Mod. Phys.*, 87:347–400, May 2015.

[93] R. J. Coles, D. M. Price, J. E. Dixon, B. Royall, E. Clarke, P. Kok, M. S. Skolnick, A. M. Fox, and M. N. Makhonin. Chirality of nanophotonic waveguide with embedded quantum emitter for unidirectional spin transfer. *Nature Communications*, 7:11183, Mar 2016.

[94] A. Laucht, S. Pütz, T. Günthner, N. Hauke, R. Saive, S. Frédérick, M. Bichler, M.-C. Amann, A. W. Holleitner, M. Kaniber, and J. J. Finley. A waveguide-coupled on-chip single-photon source. *Phys. Rev. X*, 2:011014, Mar 2012.

[95] T. Lund-Hansen, S. Stobbe, B. Julsgaard, H. Thyrrestrup, T. Sünner, M. Kamp, A. Forchel, and P. Lodahl. Experimental realization of highly efficient broadband coupling of single quantum dots to a photonic crystal waveguide. *Phys. Rev. Lett.*, 101:113903, Sep 2008.

[96] M. N. Makhonin, J. E. Dixon, R.ki J. Coles, B. Royall, I. J. Luxmoore, E. Clarke, M. Hugues, M. S. Skolnick, and A. M. Fox. Waveguide coupled resonance fluorescence from on-chip quantum emitter. *Nano Letters*, 14(12):6997–7002, 2014. PMID: 25381734.

[97] G. Reithmaier, M. Kaniber, F. Flassig, S. Lichtmannecker, K Müller, A. Andrejew, J. Vučković, R. Gross, and J. J. Finley. On-chip generation, routing, and detection of resonance fluorescence. *Nano Letters*, 15(8):5208–5213, 2015. PMID: 26102603.

[98] K. Müller, A. Rundquist, K. A. Fischer, T. Sarmiento, K. G. Lagoudakis, Y. A. Kelaita, C. Sánchez Muñoz, E. del Valle, F. P. Laussy, and J. Vučković. Coherent generation of nonclassical light on chip via detuned

photon blockade. *Phys. Rev. Lett.*, 114:233601, Jun 2015.

[99] I. Söllner, S. Mahmoodian, S. L. Hansen, L. Midolo, A. Javadi, Gabija Kiršanské, T. Pregnolato, H. El-Ella, E. H. Lee, J. D. Song, S. Stobbe, and P. Lodahl. Deterministic photonemitter coupling in chiral photonic circuits. *Nat Nano*, 10(9):775–778, September 2015.

[100] B. J. M. Hausmann, B. Shields, Q. Quan, P. Maletinsky, M. McCutcheon, J. T. Choy, T. M. Babinec, A. Kubanek, A. Yacoby, M. D. Lukin, and M. Lončar. Integrated diamond networks for quantum nanophotonics. *Nano Letters*, 12(3):1578–1582, 2012. PMID: 22339606.

[101] L.J. Rogers, K.D. Jahnke, T. Teraji, L. Marseglia, C. Mller, B. Naydenov, H. Schauffert, C. Kranz, J. Isoya, L.P. McGuinness, and F. Jelezko. Multiple intrinsically identical single-photon emitters in the solid state. *Nature Communications*, 5:4739–, August 2014.

[102] C. Santori, D. Fattal, J. Vučković, G. S. Solomon, and Y. Yamamoto. Indistinguishable photons from a single-photon device. *Nature*, 419(6907):594–597, Oct 2002.

[103] L. Sapienza, M. Davanço, A. Badolato, and K. Srinivasan. Nanoscale optical positioning of single quantum dots for bright and pure single-photon emission. *Nature Communications*, 6:7833–, Jul 2015.

[104] A. C. Dada, T. S. Santana, R. N. E. Malein, A. Koutroumanis, Y. Ma, J. M. Zajac, J. Y. Lim, J. D. Song, and B. D. Gerardot. Indistinguishable single photons with flexible electronic triggering. *Optica*, 3(5):493–498, May 2016.

[105] Y.-M. He, Y. He, Y.-J. Wei, D. Wu, M. Atatüre, C. Schneider, S. Hofling, M. Kamp, C.-Y. Lu, and J.-W. Pan. On-demand semiconductor single-photon source with near-unity indistinguishability. *Nat Nano*, 8(3):213–217, Mar 2013.

[106] J. C. Loredo, N. A. Zakaria, N. Somaschi, C. Anton, L. de Santis, V. Giesz, T. Grange, M. A. Broome, O. Gazzano, G. Coppola, I. Sagnes, A. Lemaitre, A. Auffeves, P. Senellart, M. P. Almeida, and A. G. White. Scalable performance in solid-state single-photon sources. *Optica*, 3(4):433–440, Apr 2016.

[107] K. A. Fischer, L. Hanschke, J. Wierzbowski, T. Simmet, C. Dory, J. J. Finley, J. Vučković, and K. Muller. Signatures of two-photon pulses from a quantum two-level system. *Nat Phys*, Feb 2017.

[108] K W Sun, J W Chen, B C Lee, C P Lee, and A M Kechiantz. Carrier capture and relaxation in inas quantum dots. *Nanotechnology*, 16(9):1530, 2005.

[109] S. Buckley, K. Rivoire, and J. Vučković. Engineered quantum dot single-photon sources. *Reports on Progress in Physics*, 75(12):126503, 2012.

[110] C. K. Hong, Z. Y. Ou, and L. Mandel. Measurement of subpicosecond time intervals between two photons by interference. *Phys. Rev. Lett.*, 59:2044–2046, Nov 1987.

[111] Dirk Englund, David Fattal, Edo Waks, Glenn Solomon, Bingyang Zhang, Toshihiro Nakaoka, Yasuhiko Arakawa, Yoshihisa Yamamoto, and Jelena Vučković. Controlling the spontaneous emission rate of single quantum dots in a two-dimensional photonic crystal. *Phys. Rev. Lett.*, 95:013904, Jul 2005.

[112] H. Kurtze, J. Seebeck, P. Gartner, D. R. Yakovlev, D. Reuter, A. D. Wieck, M. Bayer, and F. Jahnke. Carrier relaxation dynamics in self-assembled semiconductor quantum dots. *Phys. Rev. B*, 80:235319, Dec 2009.

[113] Peter Lodahl, A. Floris van Driel, Ivan S. Nikolaev, Arie Irman, Karin Overgaag, Daniel Vanmaekelbergh, and Willem L. Vos. Controlling the

dynamics of spontaneous emission from quantum dots by photonic crystals. *Nature*, 430(7000):654–657, August 2004.

[114] Olivier Gazzano and Glenn S. Solomon. Toward optical quantum information processing with quantum dots coupled to microstructures [invited]. *J. Opt. Soc. Am. B*, 33(7):C160–C175, Jul 2016.

[115] Jian-Wei Pan, Zeng-Bing Chen, Chao-Yang Lu, Harald Weinfurter, Anton Zeilinger, and Marek Żukowski. Multiphoton entanglement and interferometry. *Rev. Mod. Phys.*, 84:777–838, May 2012.

[116] H. S. Nguyen, G. Sallen, C. Voisin, Ph. Roussignol, C. Diederichs, and G. Cassabois. Ultra-coherent single photon source. *Applied Physics Letters*, 99(26):261904, 2011.

[117] C. Matthiesen, A. Nickolas Vamivakas, and M. Atatüre. Subnatural linewidth single photons from a quantum dot. *Phys. Rev. Lett.*, 108:093602, Feb 2012.

[118] E. B. Flagg, A. Muller, J. W. Robertson, S. Founta, D. G. Deppe, M. Xiao, W. Ma, G. J. Salamo, and C. K. Shih. Resonantly driven coherent oscillations in a solid-state quantum emitter. *Nat Phys*, 5(3):203–207, Mar 2009.

[119] H. Wang, Z.-C. Duan, Y.-H. Li, S. Chen, J.-P. Li, Y.-M. He, M.-C. Chen, Y. He, X. Ding, C.-Z. Peng, C. Schneider, M. Kamp, S. Höfling, C.-Y. Lu, and J.-W. Pan. Near-transform-limited single photons from an efficient solid-state quantum emitter. *Phys. Rev. Lett.*, 116:213601, May 2016.

[120] S. M. Ulrich, S. Ates, S. Reitzenstein, A. Löffler, A. Forchel, and P. Michler. Dephasing of triplet-sideband optical emission of a resonantly driven InAs/GaAs quantum dot inside a microcavity. *Phys. Rev. Lett.*, 106:247402, Jun 2011.

[121] A. Ulhaq, S. Ates, S. Weiler, S. M. Ulrich, S. Reitzenstein, A. Löffler, S. Höfling, L. Worschech, A. Forchel, and P. Michler. Linewidth broadening and emission saturation of a resonantly excited quantum dot monitored via an off-resonant cavity mode. *Phys. Rev. B*, 82:045307, Jul 2010.

[122] A. Thoma, P. Schnauber, M. Gschrey, M. Seifried, J. Wolters, J.-H. Schulze, A. Strittmatter, S. Rodt, A. Carmele, A. Knorr, T. Heindel, and S. Reitzenstein. Exploring dephasing of a solid-state quantum emitter via time- and temperature-dependent hong-ou-mandel experiments. *Phys. Rev. Lett.*, 116:033601, Jan 2016.

[123] S. Varoutsis, S. Laurent, P. Kramper, A. Lemaître, I. Sagnes, I. Robert-Philip, and I. Abram. Restoration of photon indistinguishability in the emission of a semiconductor quantum dot. *Phys. Rev. B*, 72:041303, Jul 2005.

[124] A. Reigue, J. Iles-Smith, F. Lux, L. Monniello, M. Bernard, F. Margaillan, A. Lemaitre, A. Martinez, D. P. McCutcheon, J. Mørk, R. Hostein, and V. Voliotis. Probing electron-phonon interaction through two-photon interference in resonantly driven semiconductor quantum dots. *ArXiv e-prints*, December 2016.

[125] V. Giesz, N. Somaschi, G. Hornecker, T. Grange, B. Reznychenko, L. De Santis, J. Demory, C. Gomez, I. Sagnes, A. Lemaitre, O. Krebs, N. D. Lanzillotti-Kimura, L. Lanco, A. Auffeves, and P. Senellart. Coherent manipulation of a solid-state artificial atom with few photons. *Nat Commun*, 7:11986, Jun 2016.

[126] M. Glässl, A. M. Barth, and V. M. Axt. Proposed robust and high-fidelity preparation of excitons and biexcitons in semiconductor quantum dots making active use of phonons. *Phys. Rev. Lett.*, 110:147401, Apr 2013.

[127] S Hughes and H J Carmichael. Phonon-mediated population inversion in a semiconductor quantum-dot cavity system. *New Journal of Physics*, 15(5):053039, 2013.

[128] J. H. Quilter, R. J. Coles, A. J. Ramsay, A. M. Fox, and M. S. Skolnick. Enhanced photocurrent readout for a quantum dot qubit by bias modulation. *Applied Physics Letters*, 102(18):1108, Apr 2013.

[129] P.-L. Ardelt, L. Hanschke, K. A. Fischer, K. Müller, A. Kleinkauf, M. Koller, A. Bechtold, T. Simmet, J. Wierzbowski, H. Riedl, G. Abstreiter, and J. J. Finley. Dissipative preparation of the exciton and biexciton in self-assembled quantum dots on picosecond time scales. *Phys. Rev. B*, 90:241404, Dec 2014.

[130] S. Bounouar, M. Müller, A. M. Barth, M. Glässl, V. M. Axt, and P. Michler. Phonon-assisted robust and deterministic two-photon biexciton preparation in a quantum dot. *Phys. Rev. B*, 91:161302, Apr 2015.

[131] A. J. Leggett, S. Chakravarty, A. T. Dorsey, Matthew P. A. Fisher, Anupam Garg, and W. Zwerger. Dynamics of the dissipative two-state system. *Rev. Mod. Phys.*, 59:1–85, Jan 1987.

[132] K. H. Madsen, S. Ates, J. Liu, A. Javadi, S. M. Albrecht, I. Yeo, S. Stobbe, and P. Lodahl. Efficient out-coupling of high-purity single photons from a coherent quantum dot in a photonic-crystal cavity. *Phys. Rev. B*, 90:155303, Oct 2014.

[133] R. Manson, K. Roy-Choudhury, and S. Hughes. Polaron master equation theory of pulse-driven phonon-assisted population inversion and single-photon emission from quantum-dot excitons. *Phys. Rev. B*, 93:155423, Apr 2016.

[134] F. Liu, L. M. P. P. Martins, A. J. Brash, A. M. Barth, J. H. Quilter, V. M.

Axt, M. S. Skolnick, and A. M. Fox. Ultrafast depopulation of a quantum dot by la-phonon-assisted stimulated emission. arXiv 1602.00628., April 2016.

[135] Ahsan Nazir. Photon statistics from a resonantly driven quantum dot. *Phys. Rev. B*, 78:153309, Oct 2008.

[136] E. M. Gauger, S. C. Benjamin, A. Nazir, and B.don W. Lovett. High-fidelity all-optical control of quantum dot spins: Detailed study of the adiabatic approach. *Phys. Rev. B*, 77:115322, Mar 2008.

[137] A. Majumdar, E. D. Kim, Y. Gong, M. Bajcsy, and J. Vučković. Phonon mediated off-resonant quantum dot cavity coupling under resonant excitation of the quantum dot. *Phys. Rev. B*, 84:085309, Aug 2011.

[138] A. Majumdar, M. Bajcsy, A. Rundquist, E. Kim, and J. Vučković. Phonon-mediated coupling between quantum dots through an off-resonant microcavity. *Phys. Rev. B*, 85:195301, May 2012.

[139] A. J. Ramsay, T. M. Godden, S. J. Boyle, E. M. Gauger, A. Nazir, B. W. Lovett, Achanta Venu Gopal, A. M. Fox, and M. S. Skolnick. Effect of detuning on the phonon induced dephasing of optically driven ingaas/gaas quantum dots. *Journal of Applied Physics*, 109(10):102415, 2011.

[140] H. Wang, X. Fan, T. Takagahara, and J. E. Cunningham. Pure dephasing induced by exciton-phonon interactions in GaAs quantum dots. In *Technical Digest. Summaries of Papers Presented at the International Quantum Electronics Conference. Conference Edition.*, volume 7, pages 162–163, May 1998.

[141] J. Förstner, C. Weber, J. Danckwerts, and A. Knorr. Phonon-assisted damping of rabi oscillations in semiconductor quantum dots. *Phys. Rev. Lett.*, 91:127401, Sep 2003.

[142] V. M. Axt, T. Kuhn, A. Vagov, and F. M. Peeters. Phonon-induced pure dephasing in exciton-biexciton quantum dot systems driven by ultrafast laser pulse sequences. *Phys. Rev. B*, 72:125309, Sep 2005.

[143] L. Besombes, K. Kheng, L. Marsal, and H. Mariette. Acoustic phonon broadening mechanism in single quantum dot emission. *Phys. Rev. B*, 63:155307, Mar 2001.

[144] C. Jarlov, É. Wodey, A. Lyasota, M. Calic, P. Gallo, B. Dwir, A. Rudra, and E. Kapon. Effect of pure dephasing and phonon scattering on the coupling of semiconductor quantum dots to optical cavities. *Phys. Rev. Lett.*, 117:076801, Aug 2016.

[145] John Howard Quilter. *Coherent Spectroscopy of Single Quantum Dots*. PhD thesis, University of Sheffield, Dezember 2014.

[146] B. Krummheuer, V. M. Axt, and T. Kuhn. Theory of pure dephasing and the resulting absorption line shape in semiconductor quantum dots. *Phys. Rev. B*, 65:195313, May 2002.

[147] P. Borri, W. Langbein, S. Schneider, U. Woggon, R. L. Sellin, D. Ouyang, and D. Bimberg. Ultralong dephasing time in InGaAs quantum dots. *Phys. Rev. Lett.*, 87:157401, Sep 2001.

[148] P. Borri, W. Langbein, U. Woggon, V. Stavarache, D. Reuter, and A. D. Wieck. Exciton dephasing via phonon interactions in InAs quantum dots: Dependence on quantum confinement. *Phys. Rev. B*, 71:115328, Mar 2005.

[149] T. Grange, C. Antón, N. Somaschi, L. de Santis, G. Coppola, V. Giesz, A. Lemaître, I. Sagnes, A. Auffèves, L. Lanco, and P. Senellart. Overcoming phonons in single-photon sources with cavity quantum electrodynamics. In *Quantum Information and Measurement (QIM) 2017*, page QW3C.3. Optical Society of America, 2017.

[150] C. Roy and S. Hughes. Phonon-dressed mollow triplet in the regime of cavity quantum electrodynamics: Excitation-induced dephasing and non-perturbative cavity feeding effects. *Phys. Rev. Lett.*, 106:247403, Jun 2011.

[151] C. Roy and S. Hughes. Polaron master equation theory of the quantum-dot mollow triplet in a semiconductor cavity-qed system. *Phys. Rev. B*, 85:115309, Mar 2012.

[152] Y.-J. Wei, Y. He, Y. H. He, C.-Y. Lu, C.-Y.Lu, C. Schneider, M. Kamp, S. Höfling, D. P. S. McCutcheon, and A. Nazir. Temperature-dependent mollow triplet spectra from a single quantum dot: Rabi frequency renormalization and sideband linewidth insensitivity. *Phys. Rev. Lett.*, 113:097401, Aug 2014.

[153] S. Unsleber, S. Maier, D. P. S. McCutcheon, Y.H. He, M. Dambach, M. Gschrey, N. Gregersen, J. Mørk, S. Reitzenstein, S. Höfling, C. Schneider, and M. Kamp. Observation of resonance fluorescence and the mollow triplet from a coherently driven site-controlled quantum dot. *Optica*, 2(12):1072–1077, Dec 2015.

[154] A. Vagov, M. D. Croitoru, V. M. Axt, T. Kuhn, and F. M. Peeters. Nonmonotonic field dependence of damping and reappearance of Rabi oscillations in quantum dots. *Phys. Rev. Lett.*, 98:227403, Jun 2007.

[155] T. Kaldewey, S. Lüker, A. V. Kuhlmann, S. R. Valentin, J.-M. Chauveau, A. Ludwig, A. D. Wieck, D. E. Reiter, T. Kuhn, and R. J. Warburton. Demonstrating the decoupling regime of the electron-phonon interaction in a quantum dot using chirped optical excitation. *ArXiv e-prints*, January 2017.

[156] V. S. Malinovsky and J. L. Krause. General theory of population transfer by adiabatic rapid passage with intense, chirped laser pulses. *Eur. Phys. J.*

D, 14(2):147–155, 2001.

[157] X. Xu, B. Sun, P. R. Berman, D. G. Steel, A. S. Bracker, D. Gammon, and L. J. Sham. Coherent optical spectroscopy of a strongly driven quantum dot. *Science*, 317(5840):929–932, 2007.

[158] A. N. Vamivakas, Y. Zhao, C.-Y. Lu, and M. Atatüre. Spin-resolved quantum-dot resonance fluorescence. *Nat Phys*, 5(3):198–202, Mar 2009.

[159] A. Ulhaq, S. Weiler, S. M. Ulrich, R. Roszbach, M. Jetter, and P. Michler. Cascaded single-photon emission from the mollow triplet sidebands of a quantum dot. *Nat Photon*, 6(4):238–242, Apr 2012.

[160] C. Matthiesen, M. J. Stanley, M. Hugues, E. Clarke, and M. Atatüre. Full counting statistics of quantum dot resonance fluorescence. *Scientific Reports*, 4:4911–, May 2014.

[161] J. I. Cirac. Interaction of a two-level atom with a cavity mode in the bad-cavity limit. *Phys. Rev. A*, 46:4354–4362, Oct 1992.

[162] H. J. Kimble. The quantum internet. *Nature*, 453(7198):1023–1030, Jun 2008.

[163] J. Hwang, M. Pototschnig, R. Lettow, G. Zumofen, A. Renn, S. Gotzinger, and V. Sandoghdar. A single-molecule optical transistor. *Nature*, 460(7251):76–80, Jul 2009.

[164] D. Englund, A. Faraon, I. Fushman, N. Stoltz, P. Petroff, and J. Vučković. Controlling cavity reflectivity with a single quantum dot. *Nature*, 450(7171):857–861, Dec 2007.

[165] C. Y. Jin, O. Kojima, T. Kita, O. Wada, and M. Hopkinson. Observation of phase shifts in a vertical cavity quantum dot switch. *Applied Physics Letters*, 98(23), 2011.

[166] C. Y. Jin, O. Kojima, T. Kita, O. Wada, M. Hopkinson, and K. Akahane. Vertical-geometry all-optical switches based on InAs/GaAs quantum dots in a cavity. *Applied Physics Letters*, 95(2):021109, 2009.

[167] E. Yüce, G. Ctistis, J. Claudon, J.-M. Gérard, and W. L. Vos. Optimal all-optical switching of a microcavity resonance in the telecom range using the electronic kerr effect. *Opt. Express*, 24(1):239–253, Jan 2016.

[168] T. Hartsfield, W.-S. Chang, S.-C. Yang, T. Ma, J. Shi, L. Sun, G. Shvets, S. Link, and X. Li. Single quantum dot controls a plasmonic cavity's scattering and anisotropy. *Proceedings of the National Academy of Sciences of the United States of America*, 112(40):12288–12292, Sep 2015.

[169] M. T. Crowley, J. Houlihan, T. Piwonski, I. O'Driscoll, D. P. Williams, E. P. O'Reilly, A. V. Uskov, and G. Huyet. Refractive index dynamics of InAs/GaAs quantum dots. *Applied Physics Letters*, 103(2), 2013.

[170] Xie Wen-Fang. Absorption spectra and refractive index changes of an exciton in a core/shell quantum dot. *Communications in Theoretical Physics*, 63(5):635, 2015.

[171] C. Thirstrup. Refractive index modulation based on excitonic effects in gainas-inp coupled asymmetric quantum wells. *IEEE Journal of Quantum Electronics*, 31(6):988–996, Jun 1995.

[172] K. Nakamura, A. Shimizu, K. Fujii, M. Koshiba, and K. Hayata. Numerical analysis of the absorption and the refractive index change in arbitrary semiconductor quantum-well structures. *IEEE Journal of Quantum Electronics*, 28(7):1670–1677, Jul 1992.

[173] Tohya Hiroshima. Electric field induced refractive index changes in $GaAsAl_xGa_{1-x}As$ quantum wells. *Applied Physics Letters*, 50(15):968–970,

1987.

[174] K. Mathan Kumar, A. John Peter, and C. W. Lee. Optical absorption and refraction index change of a confined exciton in a spherical quantum dot nanostructure. *The European Physical Journal B*, 84(3):431–438, 2011.

[175] Mark Fox. *Quantum Optics: An Introduction*. Oxford Master Series in Physics. OUP Oxford, 2006.

[176] A. Faraon, I. Fushman, D. Englund, N. Stoltz, P. Petroff, and J. Vučković. Dipole induced transparency in waveguide coupled photonic crystal cavities. *Opt. Express*, 16(16):12154–12162, Aug 2008.

[177] B. Stern, X. Zhu, C. P. Chen, L. D. Tzuang, J. Cardenas, K. Bergman, and M. Lipson. On-chip mode-division multiplexing switch. *Optica*, 2(6):530–535, Jun 2015.

[178] C Schuck, X Guo, L Fan, X Ma, M Poot, and H X Tang. Quantum interference in heterogeneous superconducting-photonic circuits on a silicon chip. *Nature Communications*, 7:10352–, Dec 2015.

[179] S. G. Carter, T. M. Sweeney, M. Kim, C. S. Kim, D. Solenov, S. E. Economou, T. L. Reinecke, L. Yang, A. S. Bracker, and D. Gammon. Quantum control of a spin qubit coupled to a photonic crystal cavity. *Nat Photon*, 7(4):329–334, Apr 2013.

[180] S. Sun, H. Kim, G. S. Solomon, and E. Waks. A quantum phase switch between a single solid-state spin and a photon. *Nat Nano*, 11(6):539–544, Jun 2016.

[181] M.O. Scully and S. Zubairy. *Quantum Optics*. Cambridge University Press, 1997.

[182] C. Gardiner and P. Zoller. *Quantum Noise: A Handbook of Markovian and Non-Markovian Quantum Stochastic Methods with Applications to Quantum Optics*. Springer Series in Synergetics. Springer, 2004.

[183] H.P. Breuer and F. Petruccione. *The Theory of Open Quantum Systems*. OUP Oxford, 2007.

[184] J. Keeling. *Light-Matter Interactions and Quantum Optics*. CreateSpace Independent Publishing Platform, 2014.

[185] A. Ulhaq, S. Weiler, C. Roy, S. M. Ulrich, M. Jetter, S. Hughes, and P. Michler. Detuning-dependent mollow triplet of a coherently-driven single quantum dot. *Opt. Express*, 21(4):4382–4395, Feb 2013.